

FATIGUE ENHANCEMENT OF UNDERSIZED, DRILLED CRACK-STOP HOLES

BY

Joshua Crain

Submitted to the graduate degree program in Civil Engineering
and the Graduate Faculty of the University of Kansas
in partial fulfillment of the requirements for the degree of
Master's of Science.

Chairperson

Committee members

Date defended: _____

The Thesis Committee for Joshua Crain certifies
that this is the approved Version of the following thesis:

FATIGUE ENHANCEMENT OF UNDERSIZED, DRILLED CRACK-STOP HOLES

Committee:

Chairperson

Date approved: _____

ABSTRACT

A common technique used to prevent the propagation of cracks in bridge girders is drilling crack-stop holes at the crack tips. By doing so, stress concentrations at the tip of the cracks are reduced and fatigue life of the bridge is extended. The size of the crack-stop hole is determined by utilizing known material properties and relationships developed through experimentation. However, these equations often result in a crack-stop hole diameter larger than can be practically drilled; therefore, physical limitations force crack-stop holes to be undersized in the field. To raise the effectiveness of the undersized holes to that of full-sized holes, a method is needed to strengthen undersized crack-stop holes.

A similar problem was reported in the aerospace industry with fastener holes, which are potential sites for cracks to initiate and propagate. Static mechanical coldworking generated a great deal of interest in the 1970s and was among several processes that were investigated for improving fatigue life of fastener holes. Extensive literature exists showing that static coldworking of fastener holes can increase fatigue-life-to-failure by a factor from three to ten, depending on stress range.

The purpose of this study is to develop a technique to improve the fatigue lives of undersized, crack-stop holes. The technique under development uses piezoelectric transducers operated at ultrasonic frequencies to improve upon recognized coldworking techniques. The piezoelectric transducers duplicate the residual compressive stresses produced by static cold expansion and hopefully change grain size. These residual compressive stresses act as a barrier to crack initiation by reducing the stress concentration at the hole. In addition, this new technique is expected to change the crystalline structure of the steel in the immediate vicinity surrounding the under-sized hole. It is thought that the excitation from the piezoelectric

transducers will refine the grain size and create a more uniform grain size thereby improving fatigue performance.

A tool is being developed that utilizes the piezoelectric transducers ability to convert electrical signals into mechanical work. Initially, the tool being developed is a small-scale laboratory device; once the technique is proven, it will be scaled up for use on full-scale bridge members under laboratory conditions. Lastly, a tool using the same technology will be developed for field application.

The research includes a set of finite element models created to aid in tool design and to quantify and characterize the residual stresses surrounding the cold expanded crack-stop holes. Results were compared and agreed quite favorably to analyses found in past literature.

ACKNOWLEDGMENTS

The successful completion of this project would not have been possible without the support, assistance and expertise of Drs. Caroline Bennett, Stanley Rolfe, Adolfo Matamoros and Ron Barrett. In addition, I would like to thank Jim Weaver for his valuable assistance in the laboratory portion of the project. I would like to thank the Transportation Pooled Fund Study, TP5-5 (189), for providing the funding which made this project possible. Finally, I would like to thank my family, without their support, I would not be where I am today.

TABLE OF CONTENTS

ABSTRACT	iii
ACKNOWLEDGMENTS	v
TABLE OF CONTENTS	vi
LIST OF FIGURES	ix
LIST OF TABLES	xii
LIST OF ACRONYMS	xiii
CHAPTER 1 INTRODUCTION	1
1.1 Problem Statement	1
1.2 Objective	4
CHAPTER 2 BACKGROUND	5
2.1 Theory of Crack Stop Holes.....	5
2.2 Theory of Static Cold Expansion	8
2.2.1 Residual Compressive Stresses.....	9
2.2.2 Current static cold expansion procedures and equipment.....	11
2.3 Previous Cold Expansion Research.....	15
2.3.1 Quantifying Residual Compressive Fields.....	15
2.3.2 Parameters effecting levels of residual stress	18
2.3.3 Effect on Fatigue Life	21
2.4 Theory of UIT	22
2.5 Fatigue Benefits of Grain Size Reduction.....	22
CHAPTER 3 EXPERIMENTAL SET-UP	24
3.1 Fatigue Specimens.....	24
3.1.1 Specimen Design	24
3.1.2 Specimen Fabrication.....	30
3.2 Fatigue Testing Methods.....	30
3.2.1 Test Groups	30

3.2.2	Stress Ranges	30
3.2.3	Loading Methods	32
3.2.4	Testing Equipment	37
3.2.5	Fatigue Test Parameters	38
3.3	Fatigue Test Instrumentation.....	39
3.3.1	Strain Gages	39
3.3.2	Strain Gage Installation.....	40
3.3.3	Data Acquisition	41
3.4	Fatigue Crack Detection.....	46
3.5	Tensile Testing	49
CHAPTER 4 EXPERIMENTAL RESULTS		52
4.1	Fatigue Specimens.....	52
4.1.1	Fatigue Life of Control Fatigue Specimens	52
4.1.2	Fatigue Life of Pick Treated Specimens	55
4.1.3	Bending Stress	57
4.2	Tensile Testing	59
4.2.1	Yield Strength	60
4.2.2	Ultimate Tensile Strength	62
4.2.3	Modulus of Elasticity	64
CHAPTER 5 FINITE ELEMENT ANALYSIS		66
5.1	Model Parameters.....	66
5.1.1	2D and 3D Uniform Expansion Model Parameters	66
5.1.2	Edge Distance Model Parameters	82
5.1.3	Hole Diameter Model Parameters.....	85
5.1.4	Plate Thickness Model Parameters	86
5.2	Model Results.....	88
5.2.1	2D Uniform Expansion Models	89
5.2.2	3D Uniform Expansion Results	92
5.2.3	Edge Distance Model Results	96
5.2.4	Hole Diameter Model Results.....	98
5.2.5	Plate Thickness Model Results	99

CHAPTER 6 CONCLUSIONS AND RECCOMENDATIONS.....	102
6.1 Conclusions	102
6.2 Recommendations	104
6.3 Future Work	104
APPENDIX A_DETAILED FATIGUE TESTING PROCEDURES	106
APPENDIX B_TENSION TEST DATA.....	107
APPENDIX C STRAIN GAGE DATA SHEET.....	138
APPENDIX D CRACKED FATIGUE SPECIMENS.....	139
APPENDIX E SAMPLE CALCULATIONS.....	147
REFERENCES	148

LIST OF FIGURES

Figure 2-1: Schematic representation of elastic-stress field distribution.....	6
Figure 2-2: Fatigue crack with drilled crack stop holes in steel bridge girder	7
Figure 2-3: Stress fields during cold expansion process.....	9
Figure 2-4: Coordinate system of residual stresses induced during cold expansion:	10
Figure 2-5: Stress values around loaded hole	11
Figure 2-6: Split sleeve cold-working process.....	12
Figure 2-7: Through thickness stress distribution of split-mandrel technique	14
Figure 2-8: Tangential residual stress distribution of a cold expanded hole	16
Figure 2-9: Tangential residual stress, uniform expansion under varying edge distance ratios ...	19
Figure 3-1: AASHTO (2007) Stress Category B detail.....	25
Figure 3-2: AASHTO Design stress range fatigue curves.....	25
Figure 3-3: 3.18 mm [0.125 in.] Fatigue specimen detail.....	27
Figure 3-4 : 3.18mm [0.125in.] fatigue specimens	28
Figure 3-5: 6.35 mm [0.250 in.] Fatigue specimen detail.....	29
Figure 3-6: AASHTO Design stress range curves for Categories A to E'	32
Figure 3-7 3.18 mm [0.125 in.] fatigue specimen with strain gages to monitor bending stress...	34
Figure 3-8: Misalignment of fatigue test equipment.....	35
Figure 3-9: Bending stress control apparatus.....	36
Figure 3-10: Installed strain gage	40
Figure 3-11: WaveBook data acquisition system test configuration	41
Figure 3-12: EBRT 2432 data acquisition system test configuration	43
Figure 3-13: NI 9219, 4-Channel, 24-Bit, Universal Analog Input Module	44
Figure 3-14: National Instruments Data Acquisition System Test Configuration.....	45

Figure 3-15: MTS TestStar <i>Station Manager</i> runtime user interface	48
Figure 3-16: MTS TestStar <i>Station Manager</i> limit detector user interface	48
Figure 3-17: 3.18 mm [0.125 in.] Standard tension specimens	49
Figure 3-18: 6.35 mm [0.250 in.] Standard tension specimens	50
Figure 3-19: Tension test configuration 3.18 mm [0.1250 in.] thick specimens	51
Figure 3-20: Tension test configuration 6.35 mm [0.250 in.] thick specimens	51
Figure 4-1: Results of preliminary investigated stress ranges	53
Figure 4-2: Comparison of results from control specimens and PICK treated specimens	55
Figure 4-3: Stress-Strain plot used to determine yield strength.....	61
Figure 4-4: Stress-Strain plot used to determine ultimate tensile strength	63
Figure 4-5: Strain gage readings used to quantify modulus of elasticity.....	65
Figure 5-1: Stress-strain plot for for 2024-T3 Alclad Aluminum.....	68
Figure 5-2: Stress-strain plot for Gr. A36 Steel.....	69
Figure 5-3: Parametric study determining mesh size in 2D aluminum UE FEM.....	72
Figure 5-4: Partitioned 2D aluminum UE model.....	74
Figure 5-5 Final mesh configuration of aluminum and steel 2D UE models	75
Figure 5-6: Parametric study determining mesh size in 3D mild steel UE FEM	77
Figure 5-7: Partitioned 3D mild steel UE model with rectangular partition.....	78
Figure 5-8 Final meshed 3D mild steel UE model,	79
Figure 5-9: Partitioned 3D mild steel UE model with circular partition	80
Figure 5-10 Final meshed 3D UE model with circular partition surround UE hole.....	81
Figure 5-11 Comparison of 3D UE models with circular and rectangular partitioning schemes.	82
Figure 5-12 Geometric details and edge distance dimensions for edge distance ratio FEMs	84

Figure 5-13: Final mesh configuration for typical edge distance ratio FEM.....	84
Figure 5-14: Final mesh configuration for typical hole diameter model	86
Figure 5-15: Geometric details and edge distance dimensions for plate thickness FEMs.....	87
Figure 5-16: Final mesh configuration for typical plate thickness FEM	88
Figure 5-17: Tangential stress for 2D UE aluminum models at various levels of expansion	89
Figure 5-18: Tangential stress field for 2D UE Gr. A36 Steel	90
Figure 5-19: Tangential stress field for 2D UE 2024-T3 Alclad Aluminum vs. Gr. A36 Steel ...	92
Figure 5-20: Tangential stress field for 2D UE models versus 3D UE models @ mid-thickness	93
Figure 5-21: Through thickness tangential stress field for 3D UE models.....	95
Figure 5-22: Tangential stress field for Edge Distance Model at 3 Percent Expansion	96
Figure 5-23: Tangential stress field for Edge Distance Model at 4 Percent Expansion	97
Figure 5-24: Tangential stress field for Edge Distance Model at 5 Percent Expansion	97
Figure 5-25: Tangential stress field for Edge Distance Model at 6 Percent Expansion	98
Figure 5-26: Tangential stress field for hole diameter models at 4 Percent Expansion	99
Figure 5-27: Tangential stress field for varying plate thickness models	100
Figure 5-28: Tangential stress field for varying expansion models, plate thicknesses varies	101

LIST OF TABLES

Table 4-1: Preliminary investigation for test stress ranges of fatigue specimens.....	54
Table 4-2: Results and dimensions of control and PICK treated specimens	56
Table 4-3: Bending stress summary for 3.18 mm [0.125 in.] thick fatigue specimens	58
Table 4-4: Summary of results for 3.18 mm [0.125 in.] tension specimens.....	59
Table 4-5: Summary of results for 6.35 mm [0.250 in.] tension specimens.....	59
Table 5-1: Basic material properties used in FEM	68

LIST OF ACRONYMS

Acronym	Description
2D	Two-Dimensional
3D	Three-Dimensional
AASHTO	American Association of State Highway and Traffic Officials
ASTM	American Society for Testing and Material
DCE	Dynamic Cold Expansion
FEA	Finite Element Analysis
FEM	Finite Element Model
FLI	Fatigue Life Improvement
MnDOT	Minnesota Department of Transportation
PICK	Piezoelectric Impact Compressive Kinetics
SPD	Severe Plastic Deformation
UE	Uniform Expansion
UIT	Ultrasonic Impact Treatment

CHAPTER 1 INTRODUCTION

1.1 PROBLEM STATEMENT

Currently, bridges all throughout the country contain connection details that are susceptible to the formation of fatigue cracks. At the time these bridges were designed and constructed, engineers lacked some of the fundamental knowledge of the causes of fatigue crack formation. Fatigue prone connection details are in such abundance that the Minnesota Department of Transportation (MnDot) funded a research study, incorporating numerous other DOT's to determine existing details most susceptible to fatigue crack formation [1]. A summary of these fatigue prone details can be found in the report written by Lindberg and Schultz [1].

While the number of bridges with fatigue prone details is alarming, fortunately most fatigue failures have a relatively long propagation period between original crack detection to eventual failure. As a result of the relatively long propagation life, measures can be taken to retrofit and preserve existing cracked bridge members if fatigue cracks are detected in early stages of propagation. There are several existing methods available that can retard the propagation of fatigue cracks. These methods include: (1) grinding away shallow cracks; (2) adhesive patching with composite materials; (3) welding the cracks; (4) implementing metal reinforcements; (5) drilling holes at the tips of cracks and (6) modifying connection details [2]. These methods are attractive considering the alternatives are either the complete replacement of the cracked structural member or reducing external loads coupled with careful monitoring. One extremely common retrofit technique is to drill a hole at the tip of a fatigue crack to halt or slow its propagation [3,4]. The challenges associated with correctly applying this technique are that the theoretical size of a properly sized crack-stop hole is often too large for practical

implementation in the field or the location is blocked by other members. To overcome this issue, crack-stop holes are often drilled undersized and left unreinforced.

A similar problem is faced in the aerospace industry where large stresses are commonly seen at the edges of fastener holes, often sites for crack initiation. In order to strengthen these fastener holes, the holes are often statically cold expanded. Static cold expansion is typically accomplished by forcing an oversized, tapered mandrel through the hole, often resulting in fatigue life improvement between 3 – 10 times that of an untreated hole, depending on stress range [5-8]. This quantified level of improvement in fatigue life is often reported for newly drilled, uncracked statically-expanded fastener holes. However, the resulting fatigue life benefits are similar for holes cold expanded in crack-stop hole situations [4, 9, 26].

The cold expansion process results in an increased fatigue life by inducing high residual compressive stresses around the edges of the holes caused by permanent deformation. The hole is forced to expand through a mechanical process. Yielding will first occur along the edges of the hole where stresses are highest. As further expansion is mechanically induced, the zone of plasticity spreads further outward from the hole. Material that lies beyond this plastically-deformed region will deform elastically under the applied displacement. After the mechanically-applied displacement is removed from the system, residual compressive stresses around the hole are created from the elastic rebounding, or “springback” of the unyielded material surrounding the permanently-deformed plastic zone [10].

While several static cold expansion techniques are currently available having the ability to induce beneficial compressive residual stresses, a new technique is being developed that will not only induce these beneficial residual stresses but is thought will refine the grain size in the inside surfaces of the crack-stop holes. The specific technique being developed uses

piezoelectric transducers to dynamically work and cold-expand the volume of steel plate surrounding a crack-stop hole's inner surface. Dynamically working steel through impact at high frequencies is a proven method for refining coarse grained steel into finer grained material [11], which can translate into improved fatigue performance. The technique investigated in this report has been termed Piezoelectric Impact Compressive Kinetics (PICK).

1.2 OBJECTIVE

This research is focused on improving the fatigue lives of steel bridge structures. While cold expansion techniques exist, these have been applied to aerospace structures. The value these methods of cold expansion have shown on fatigue performance of aerospace structures suggests it is sensible to extend the technique's applicability to steel bridges. Therefore, the objective of this research is twofold:

1. Investigate the appropriateness of generic cold expansion techniques for steel bridge fatigue life improvement through comparison against existing results reported in aerospace engineering literature, and,
2. Develop a new technique suitable for improving the fatigue lives of steel bridges (PICK).

To permit the application of current static cold expansion techniques, commonly used on aerospace materials (primarily aluminum), to be extended to materials frequently used in bridge construction (in this case steel), a series of finite element models (FEMs) were prepared. A discussion of these FEMs can be found in Chapter 5 of this report. In addition, a series of laboratory fatigue tests were performed to determine the fatigue life improvement possible through treatment with the newly developed PICK technique. The preliminary results from this laboratory investigation can be found in Chapters 3 and 4 of this report.

CHAPTER 2 BACKGROUND

2.1 THEORY OF CRACK STOP HOLES

Current methods used to determine sizes of crack-stop holes are based on linear-elastic fracture-mechanic theory [12]. Analytical methods involving linear-elastic fracture mechanics are based on the procedure that relates magnitude of the stress-field near the tip of a crack to nominal applied stress, as described by Eq. (2-1):

$$\sigma_{\max} = k_t \sigma_{\text{nom}} \quad (2-1)$$

Factors that affect the magnitude of the stress amplification term, k_t , are: size, shape, and orientation of the crack or crack-like imperfections. The elastic-stress field at the edge of an imperfection, as described in Eq. (2-2), is derived under the assumption that the shape of the imperfection is either elliptical or hyperbolic (see Figure 2-1) and the nominal applied stress is normal to the plane of the imperfection.

$$\Delta\sigma_{\max} = \frac{2\Delta K_I}{\sqrt{\pi\rho}} \quad (2-2)$$

In Eq. (2-2), the stress intensity factor, ΔK_I , is determined assuming a zero radius crack tip and an initial crack length, $a = a_o + \rho$, where ρ is the radius of the hole.

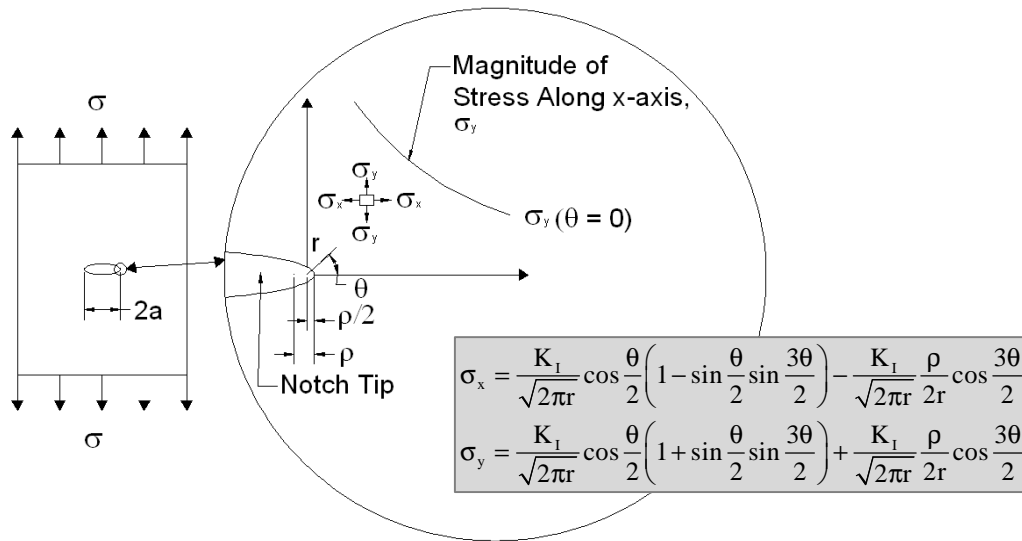


Figure 2-1: Schematic representation of elastic-stress field distribution near the tip of an elliptical crack

From Eq. (2-2), it is observed that ΔK_I and the square root of the radius of the notch tip, $\sqrt{\rho}$, each alter the magnitude of maximum stress seen at the edge of the notch. Eq. (2-2), which is valid for relatively sharp notches, is only exact when the notch tip radius is equal to zero. However, finite element analyses have shown that Eq. (2-2) provides a fairly accurate relationship for imperfections with notch tip radii small compared with the crack length, $2a$ [13]. The theoretical relationship between terms $(\Delta K_I/\sqrt{\rho})$ and maximum stress, $\Delta\sigma_{max}$, led to further laboratory investigation to study its significance to fatigue crack initiation life. Thus, through basic fracture mechanic theory and extensive laboratory testing, Eq. (2-3) was derived in [12], and can be used for determining the proper size of crack-stop hole radii in steel bridges:

$$\rho = \left(\frac{\Delta K_{total}}{10\sqrt{\sigma_{ys}}} \right)^2 \quad (2-3)$$

As an illustrative example as to how Eq. (2-3) may be applied in a practical application, consider the following typical case in which crack-stop holes may be necessary: A fatigue crack is found during an inspection in the web of a bridge girder, near the top flange. The crack runs

longitudinal to the girder, as shown in Figure 2-2, and is 216 mm [8.5 in.] long, offset 12.7 mm [0.5 in.] from the top flange. Therefore, there is dimensional room for a crack-stop hole with an approximate diameter of 25.4 mm [1.0 in].

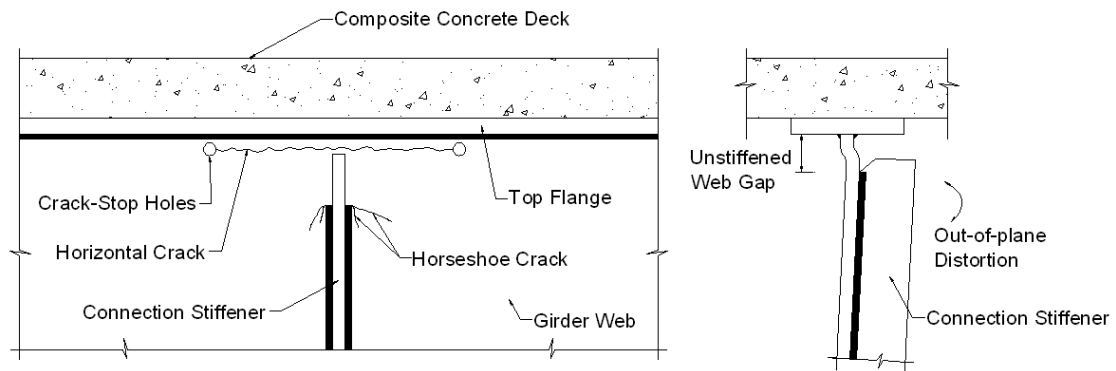


Figure 2-2: Fatigue crack with drilled crack stop holes in steel bridge girder

For the fatigue crack scenario presented, consider the steel in the girder's web to be Gr. A36 with static yield strength, $\sigma_{ys} = 248 \text{ MPa}$ [36 ksi]. For the 216 mm [8.50 in.] length crack, the stress intensity factor, ΔK_{total} , can be determined as follows (note that the following calculations are provided in US standard units as Eq. (2-3) is unit-sensitive):

$$\Delta K_{total} = \Delta\sigma\sqrt{\pi a} \quad (2-4)$$

$$\Delta K_{total} = (26^{\text{ksi}}) \sqrt{\left(\pi\right) \left(\frac{8.5 \text{ in.}}{2}\right)} = 95.0 \text{ ksi}\sqrt{\text{in.}}$$

The value of 179 MPa [26 ksi] assumed for the nominally applied stress was taken from previous finite element studies [14,15] which quantified nominal stress seen at web gaps of details similar to that shown in Figure 2-2. The required radius to halt crack propagation can then be directly solved for from Eqn. 3:

$$\rho = \left(\frac{95.0 \text{ ksi}\sqrt{\text{in.}}}{10\sqrt{36 \text{ ksi}}}\right)^2 = 2.51 \text{ in.}$$

Therefore, the required crack-stop hole diameter for the 216 mm [8.50 in.] long crack is approximately 127 mm [5.0 in.]. For this crack length, there is not enough space to install a properly-sized crack-stop hole; therefore, the hole would need to be undersized due to the dimensional constraints. The 25.4 mm [1.0 in.] diameter holes could serve as a temporary aid to retard the crack from propagating. However, eventually the fatigue crack would reinitiate and propagate away from the undersized holes edge until eventual failure of the structural member or additional repair. This situation is often typical for crack-stop hole design scenarios, where the hole diameter needed to completely halt crack propagation is simply too large to be practically implemented.

2.2 THEORY OF STATIC COLD EXPANSION

Utilizing static cold expansion to improve fatigue life of holes in metal plates began generating interest in the 1970s, primarily in the aerospace industry. Early interest in static cold expansion was generated due to the need to reinforce and improve fatigue performance of fastener holes, often locations prone to crack formation. Through laboratory investigations, static cold expansion was shown to reduce the probability of crack initiation and continued growth of fatigue cracks from fastener holes in various grades of aluminum, titanium and high strength steels [7].

2.2.1 Residual Compressive Stresses

Static cold-expansion improves fatigue performance of holes in metal plates due to the high residual compressive stresses it induces around the edges of the holes. These residual stresses are formed by permanently deforming the material surrounding the inside of the hole.

Permanent deformation is often achieved though pulling an oversized mandrel through the hole, causing yielding along the edges of the hole. The tangential stress is positive at the expansion stage, and after reaching a maximum, will decay away from the edge of the hole, Figure 2-3a.

Material that lies beyond this plastically-deformed region will deform elastically under the applied displacement. Once the mandrel has completely passed through the hole the unloading process generates a zone of residual compressive stress created from the elastic rebounding, or “springback,” of the unyielded material surrounding the permanently-deformed plastic zone [10].

The zone of residual compressive stresses resulting from elastic rebounding can be seen in Figure 2-3b.

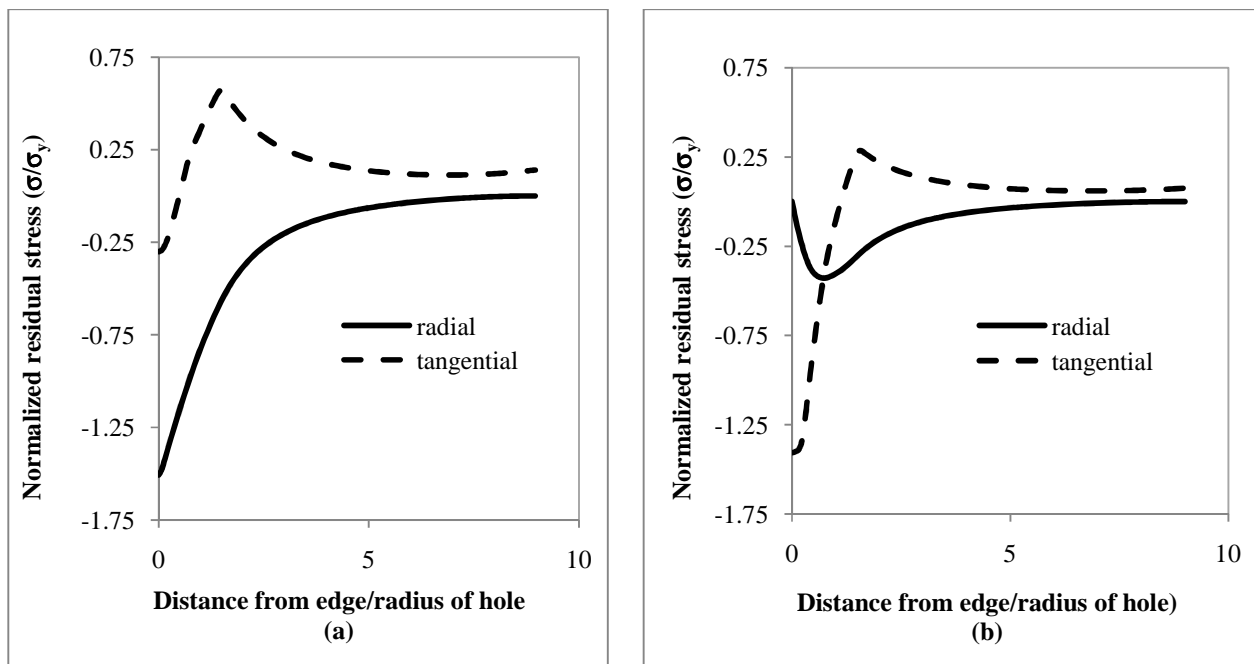


Figure 2-3: Stress fields (a) during cold expansion process (b) upon completion of cold expansion process

Among the three principal residual stresses (see Figure 2-4) generated from SCE (tangential, radial, and transverse), the tangential (i.e. hoop stress) at the edge of the hole is most responsible for the considerable gain in fatigue life [8].

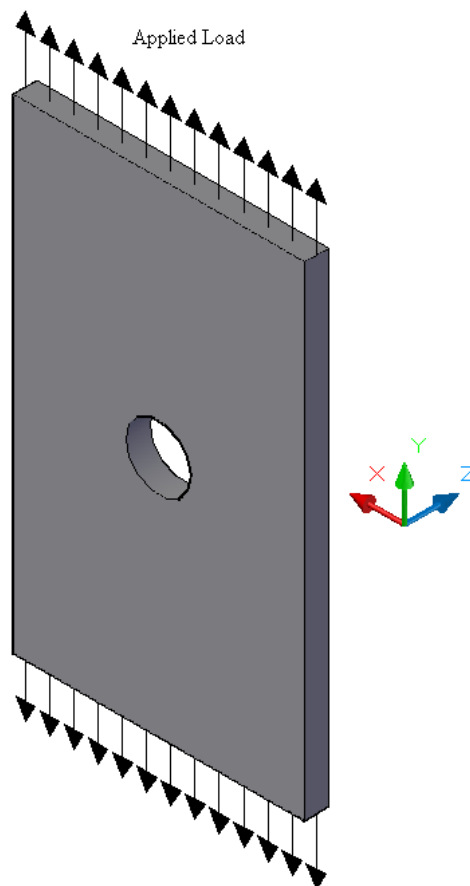


Figure 2-4: Coordinate system of residual stresses induced during cold expansion: (x-axis = radial; y-axis = tangential, circumferential, hoop; z-axis = transverse)

The tangential residual stress field, Figure 2-3b, is the main contributor to improved fatigue performance because the direction of tangential residual stress coincides with that of the large stress concentration caused by geometric discontinuity effects created by a hole (see Figure 2-5).

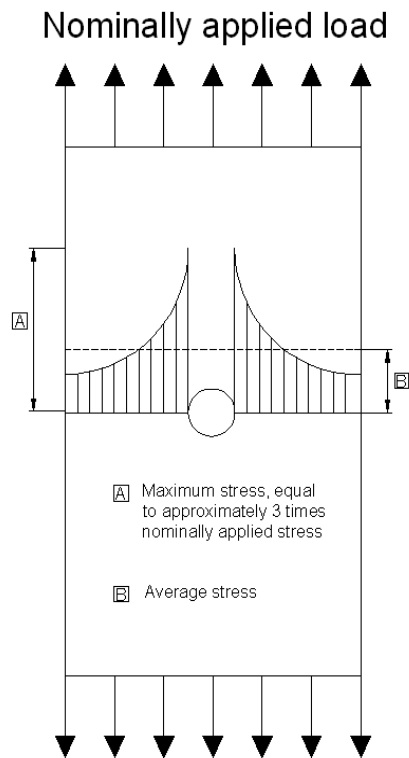


Figure 2-5: Stress values around loaded hole

2.2.2 Current static cold expansion procedures and equipment

Several static cold expansion methods are currently available for the treatment of fastener holes; however, the most effective and widely accepted technique intended for aerospace applications is the split sleeve mandrel process developed by Fatigue Technology Incorporated (FTI) of Seattle, WA. This particular technique was introduced in the 1970's by Boeing Commercial Airplane Company and is now commonly performed in aircraft maintenance and manufacturing [6].

The split sleeve mandrel process, as seen schematically in Figure 2-6, utilizes a solid, tapered mandrel and an internally lubricated steel split sleeve. The split sleeve process begins by positioning the sleeve over the mandrel and inserting the mandrel into the hole. The externally applied force on the mandrel easily deforms the material around the inside edge of the hole. An optimum level of expansion for the split sleeve technique is typically between 3-5% of the

original hole diameter, although this may vary depending on the particular application and the local geometry of the component and material [6,8,17-18,20-21,26]. The deformed material is displaced beyond the yield point extending the plastic zone a large distance away from the edges of the hole. Upon removal of the mandrel, constraint created by the surrounding elastic region causes extensive reverse yielding of the material at the edge of the hole and causes a relaxation of the highly overstrained region. The expanded sleeve remains in the hole and can be left in the hole or discarded. It should be noted that it is common practice remove existing damage by reaming or drilling and reaming the inside of the fastener hole [16].

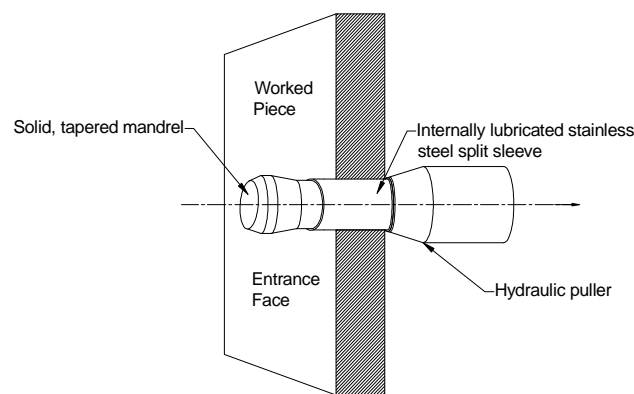


Figure 2-6: Split sleeve cold-working process.

Benefits the split sleeve technique offers over other available static cold expansion methods are its ability to effectively treat the complete through thickness of a plate and its ease of use. Other static cold expansion methods have shown a similar ability to generate beneficial residual stresses at a plate's mid-thickness; however, most static cold expansion methods lack the ability to resist transverse plastic deformation around plates outside edges. This extensive plastic flow of material in the transverse direction will result in a reduction in the amount of plastic deformation possible in the radial and tangential directions. The result of a reduced level of

plastic deformation causes both the size of the plastic zone and the magnitude of the material constraint to be decreased resulting in residual stresses that are less compressive [8].

The split sleeve process is the most effective technique in generating uniform levels of stress through the thickness of plates. However, a number of FEM and laboratory studies have shown the split sleeve technique to produce slightly lower levels of residual stress at a plate's entrance and exit faces as compared to at mid-thickness. [5-8, 16-18] In a study performed by Fourges et. al., a series of finite element models (FEMs) of the split sleeve process were created showing that the lowest level of residual stresses occurred at the entrance face of the treated hole (Figure 2-7). The reason for higher levels at the mid-thickness is simple; with more material available to constrain the plastic zone, a higher level of residual stress will result. At the exit face, the level of residual stress is greater as a result of the modified geometrical conditions at the exit face caused by the accumulation of material volume as the mandrel moves through the hole [18].

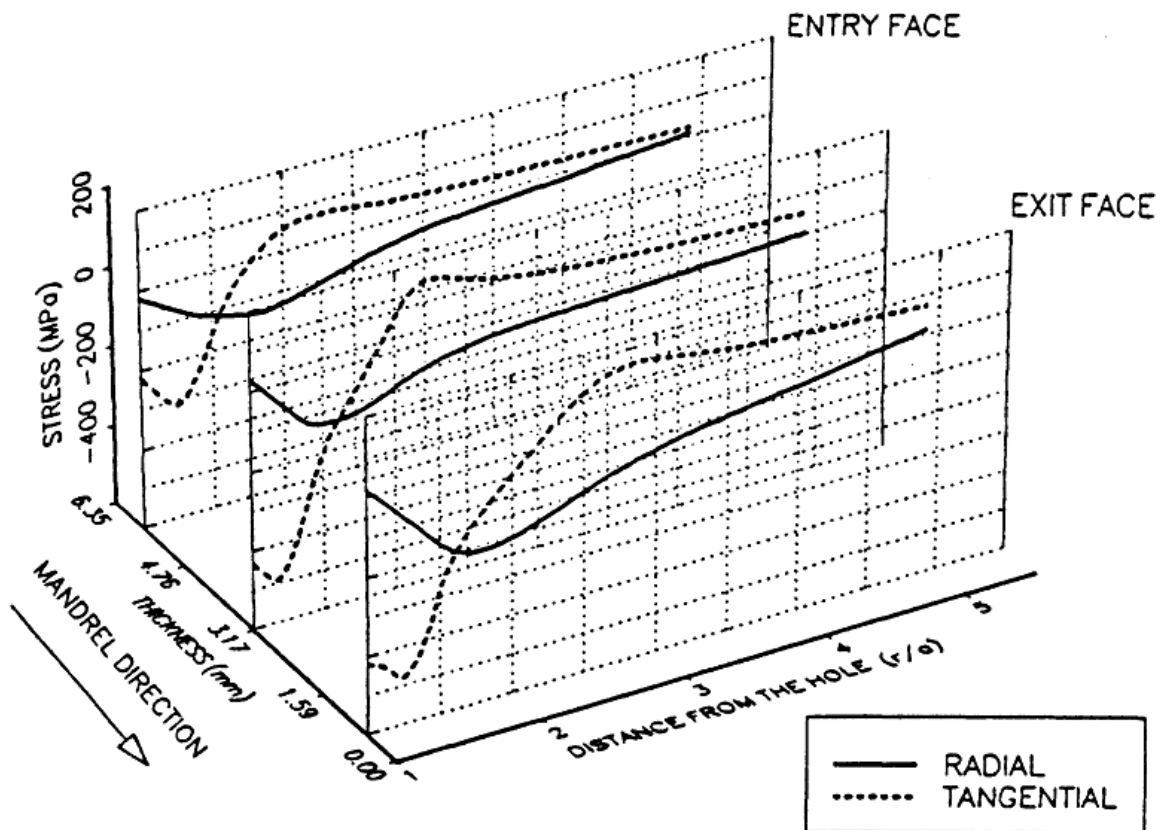


Figure 2-7: Through thickness stress distribution of split-mandrel technique, figure taken from work by Forgues et. al. [18] (r = distance from hole's edge, a = radius of hole)

An extensive amount of research has been performed on the optimization of the split-sleeve mandrel cold-working process [19]. The focus of these prior studies was broken up into two phases. The first phase focused on basic aspects of the split sleeve mandrel process, such as mandrel taper angle, level of interference, puller force requirements, and post reaming requirements. These and other parameters were investigated until optimized values were achieved that maximized beneficial effects such as a minimized puller force and increased fatigue life [19]. For the second phase, effects of additional process parameters were investigated. This included the presence of cracks prior to the cold-working procedure. It was concluded that there was a critical existing crack size above which no residual compressive

stresses could be generated. However, for specimens with cracks smaller than critical crack sizes, results showed that if the ratio of the distance between a hole centerline to the edge of the specimen and a hole's diameter were of reasonably large values, cold-working of previously cracked specimens could be successfully accomplished [4]. Similar investigation will be required in order to optimize the parameters of the PICK tool technique.

2.3 PREVIOUS COLD EXPANSION RESEARCH

2.3.1 Quantifying Residual Compressive Fields

To reasonably predict the levels of improved fatigue performance resulting from cold expanding crack-stop holes, residual stresses must be accurately quantified. A number of analytical investigations and techniques have been proposed and compared with the laboratory investigation, performed as part of this thesis. These previous studies are discussed in the following sections.

2.3.1.1 Analytical Methods

Previous analytical investigations of static cold expansion [7,17,10,20-21] have been based largely on two-dimensional approximations. These closed-form solutions have been applied to both the plain-strain condition of the thick-walled cylinder and the plain-stress condition of holes in infinitely wide plates. These analytical simplifications used both Tresca and von Mises yield criterion with assumptions of either elastic-perfectly-plastic or strain-hardening material properties. An extensive review of these closed-form solution techniques has been performed by Poolsuk [10].

Each method reported by Poolsuk [10] attempted to quantify and characterize the level of residual stress that could be achieved through static cold expansion. The methods of analysis were consistent in showing that a level of residual compressive stress approximately equal to the yield strength of the material could be achieved in the tangential direction near the edge of a hole (Figure 2-8). These methods have also shown that residual compressive stresses decay rapidly in the radial direction and at a distance equal to approximately the diameter of the hole away from the holes edge, residual stress will reach its maximum tensile stress. This distance is referred to as the elastic-plastic boundary, r_p (Figure 2-8). Previous analytical investigations have consistently shown r_p to be a function of varying levels of expansion and plate thickness. The benefit to a larger value of r_p is that it tends to increase the zone of residual compression.

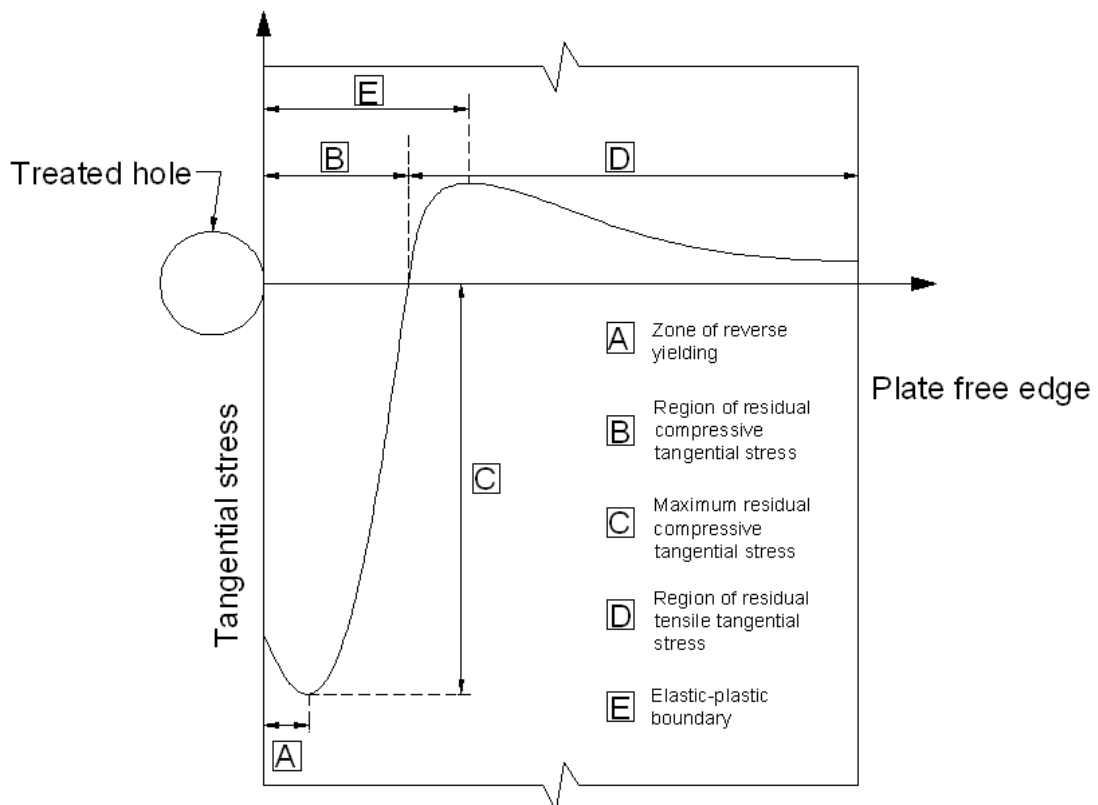


Figure 2-8: Tangential residual stress distribution of a cold expanded hole

More recent investigations have examined various parameters that affect the level of residual compressive stress that can be achieved. These parameters were investigated through FEMs of varying levels of complexity. The purpose of these investigations was to understand in more real-world settings the level of residual stress achievable through static cold expansion of holes in metal plates. The majority of previous FEMs studied various grades of aluminum, however, due to the similar nature between the results from aluminum and mild steel, FEMs created in Chapter 5 of this report, it is reasonable to assume that previously investigated parameters will have similar effects on holes coldworked in mild-steel bridge elements, as they were found to have in aluminum. The parameters, discussed in section 2.3.2 of this report, are: edge distance effects; size of the hole; thickness of the plate; and effects of preexisting cracks surrounding the hole.

2.3.1.2 Experimental Methods

A variety of techniques exist that have shown to be reliable for measuring levels of residual stress surrounding a static cold expansion hole. In general, there are two experimental approaches that can be used to measure residual stresses. First, non-destructive methods such as neutron and X-ray diffraction, which involve the direct measurement of dimensional changes in lattices as microstrains using diffraction techniques, can be used. Second, destructive techniques, which involve measuring changes in macrostrains in a section by successive removal of layers of the material, can alternatively be used to measure residual stresses [6]. Examples of the implementation of these and additional methods can be found in works referenced in this report [6,22-24].

2.3.2 Parameters effecting levels of residual stress

Section 2.3.1 of this report was intended to provide a general overview of the levels of residual stresses that can be induced around a static cold expansion hole in a metal plate. The purpose of the following section is to discuss the effects of changing several systems parameters on residual stress profile.

2.3.2.1 Edge Distance Effects

Since the early stages of static cold expansion development, there has been concern regarding the residual stress distribution in holes located near a plate's edge. The concern was that without sufficient material between the static cold expansion hole and the free surface there would be an insufficient amount of elastic material surrounding the hole to constrain the plastic region not allowing for proper "springback" of the elastically deformed region to occur.

Ayatollahi and Nik [25] performed a study investigating this concern at the Iran University of Science and Technology. In the study, 2D FEMs of Al 2024 plates were created under varying levels of uniform expansion. It was concluded that edge distance did have a significant impact on the residual stress profile resulting from static cold expansion. As a general rule, so long as the edge distance ratio, e/D , e being the distance between the center of the hole and the free edge, and D the diameter of the hole, is kept above $e/D = 3$, there is sufficient material to control the plastic zone and compressive residual stress is not affected. However, for edge ratios lower than $e/D = 3$, the aimed benefits of cold expansion were not nearly as dependent on degree of cold expansion and therefore similar, while lower levels of compressive stress can be accomplished through very minimal levels of expansion (see Figure 2-9).

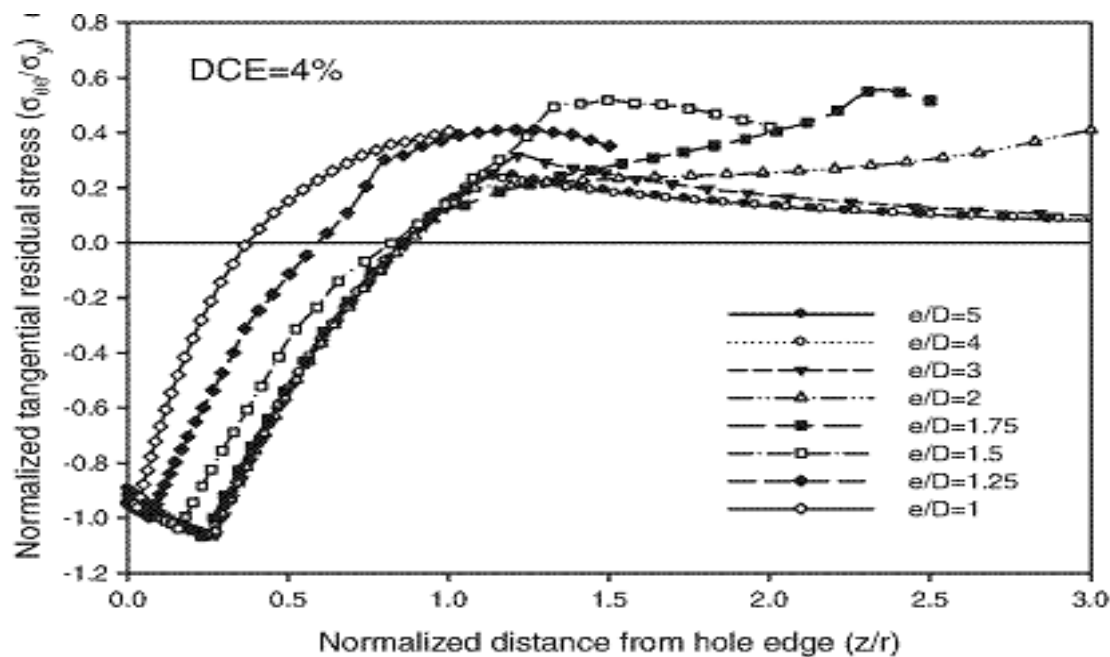


Figure 2-9: Tangential residual stress distribution resulting from a 4% uniform expansion under varying edge distance ratios, figure taken from Ayatollahi and Nik [25]., (z = distance from holes edge, r = radius of treated hole)

In a separate study performed by Ball and Lowry [19] the edge distance parameter was similarly investigated; however, rather than comparing residual stress profiles, level of fatigue life improvement (FLI) was investigated for specimens with varying levels of edge distance ratios. Results of specimen's static cold expansion with e/D ratios of 1 and 4 were compared. Fatigue tests showed that specimens with e/D ratios equal to one produced fatigue life improvement over non treated specimens anywhere from 3.1-4.2 times, while specimens with e/D ratios equal to four produced FLIs greater than 10 times.

2.3.2.2 Hole Diameter Effects

Changes in hole diameter have shown little or no effect on the residual stress profile of static cold expansion specimens of finite width. A study by Amrouche et. al. [4] showed that changing hole diameter had no effect on the zone of compressive residual stress, maximum

achievable residual stress or the size of the plastic deformation of finite width specimens treated with static cold expansion.

2.3.2.3 Plate Thickness Effects

Previous works by Herman and Ozdemir [8] investigated the effects that plate thickness would have on the residual stress distribution surrounding a static cold expansion hole. Plate thickness effects were investigated for two static cold expansion techniques: split sleeve mandrel and roller burnishing. It was concluded that for both techniques the maximum level of residual stress increased and beneficial compressive stresses were maintained for a farther distance away from the holes edge as plate thickness increased. This occurred because as thickness increased the resulting material constraint, or region of resistance behind the plastic zone, increased as well. Consequently, residual stresses produced after static cold expansion became more compressive. Thickness also affected the location of the elastic-plastic boundary; as the thickness of the plate was increased so too was the elastic-plastic boundary.

It is important to note that while residual compressive stresses were increased for both static cold expansion techniques, the level of increase with varying thickness differed for both techniques. Additionally, the optimum level of expansion varied depending on technique and thickness. This fact is vital to any investigation of a new cold expansion technique because optimum level of expansion is likely to vary from previously established techniques.

2.3.2.4 Holes Treated with Existing Cracks

For aerospace applications, static cold expansion of fastener holes can be performed for two scenarios. The first is for precautionary purposes during the manufacturing stage to prevent the formation of fatigue cracks. The second scenario, which would be for maintenance purposes, is

when fastener holes are treated with preexisting cracks emanating from the sides of the hole. Concerns regarding the treatment of fastener holes with pre-existing cracks were raised because it was not clear if similar levels of residual stress to that of uncracked holes could be generated. This topic of concern has been investigated in past studies [19, 24].

One particular investigation, performed by Stefanescu et. al.[24], concluded that beneficial residual stresses, slightly lower than that of an uncracked holes, can be achieved in specimens with existing cracks. However, these slightly lower levels of residual stress can only be achieved up to a certain initial crack length. It was determined that there exists a critical crack size above which no beneficial residual compressive stresses can be generated. The critical crack size, however, is a complex computation depending on the material's fracture resistance, geometry and the applied level of expansion [24].

In a separate study, performed by Ball and Lowry [19], the levels of residual stress that could be achieved in cracked specimens were also investigated. Similar to the study performed by Stefanescu et. al. [24], it was concluded that there existed a critical initial crack size above which no residual compressive stresses could be achieved. However, in their report they noted that critical crack size was dependent on e/D ratios. For specimens with small e/D ratios, the cracks were shown to extend during the cold working process, and as a result, little or no compressive residual stress was developed. For specimens with larger e/D ratios, holes were successfully coldworked with pre-cracks up to the critical crack size.

2.3.3 Effect on Fatigue Life

The ultimate objective of the static cold expansion technique is the fatigue life improvement it creates for holes in metal plates. Quantifying the level of FLI has been the focus of many past studies which have been performed for two static cold expansion scenarios. The first scenario

considers the potential FLI of a specimen with a drilled, reamed and initially uncracked hole.

For this situation, FLI for static cold expansion holes has been consistently shown to be greater than 3 times that of an untreated hole and often can even be greater than 10 [5-8, 27].

The second method of fatigue testing, which is more relevant to the situation of crack-stop hole enhancement in bridges, are tests conducted attempting to quantify the fatigue life improvement of holes drilled at the tips of cracks. Results from past studies [4,9,26] consistently displayed FLI above 3 times that of an untreated hole.

2.4 THEORY OF UIT

Ultrasonic impact treatment (UIT) is considered one of the most effective methods for improving the reliability and fatigue strengths of welded joints [28]. The technique was developed in the late 1960's and early 1970's with the purpose of increasing fatigue life of welds by improving geometric characteristics and stress states of welds. UIT improves fatigue life of welded joints through a variety of mechanisms. One of the most significant mechanisms is the relaxation of residual stresses through application of ultrasonic stress waves at the weld surface [29].

Additional mechanisms include severe plastic deformation generated at the weld surface, reduction in micro discontinuities, and grain refinement of weld material. A detailed overview of the mechanisms and procedures associated with the UIT process can be found in Vilhauer et. al.[29].

2.5 FATIGUE BENEFITS OF GRAIN SIZE REDUCTION

“The resistance of metals and alloys to fatigue crack initiation and propagation is known to be significantly influenced by grain size” [30]. With all other structural variables remaining constant, the fatigue life of an initially smooth surface specimen will increase with decreasing

grain size. One effective method for refining grain size in metals is referred to as severe plastic deformation (SPD). In recent decades, a number of SPD based processes for surface nanocrystallization, Esonix UIT, ultrasonic shot peening, and surface mechanical attrition treatment, have been commercially introduced and have received considerable attention due to their simplicity and low cost [30]. The key feature for these processes is the impact of the worked piece surfaces at ultrasonic frequencies creating material with a surface nanocrystalline layer and a coarse grain interior [31]. The results of these SPD processes have been shown to improve a material's tensile strength, microhardness, wear resistance, and fatigue strength [30]. The PICK tool, developed at the University of Kansas and introduced in this thesis, will attempt to generate SPD at ultrasonic frequencies to refine grain size of the material near the inside surface of the crack-stop holes. The resulting nanocrystalline surface, along with the beneficial residual stresses induced by cold expansion, will result in a FLI potentially greater than any current static cold expansion technique.

CHAPTER 3 EXPERIMENTAL SET-UP

3.1 FATIGUE SPECIMENS

To investigate the effectiveness of the PICK tool to enhance fatigue life of undersized drilled crack-stop holes, an experimental program was created. The preliminary goal of this research program was to investigate potential fatigue life improvement of uncracked holes treated with the newly developed PICK tool. If the PICK tool is found to successfully enhance fatigue life of initially uncracked holes, the next stage in the experimental program will be to generate a new series of specimens, designed to more realistically simulate crack-stop hole scenarios.

This program was funded by the Transportation Pooled Fund Study, TP5-5 (189), Kansas DOT, and the KU Transportation Research Institute. All experimental testing was performed at University of Kansas School of Engineering-this includes Civil Engineering and adaptive Aerostructures labs.

3.1.1 Specimen Design

The first phase of fatigue specimens were designed to simulate an American Association of State Highway and Traffic Officials (AASHTO) Stress Category B detail. The Category B detail considered was “base metal at gross section of high-strength bolted slip resistant connection...” Fisher [32]. The AASHTO (2007) connection detail is shown in Figure 3-1: . A bolted slip critical connection prevents any sliding to occur between connected plates. The prevention of sliding allows for the entire load to be transferred through the drilled holes. Therefore, it was reasonable to classify the fatigue specimens, a single plate with a drilled hole at the center, as Category B detail.

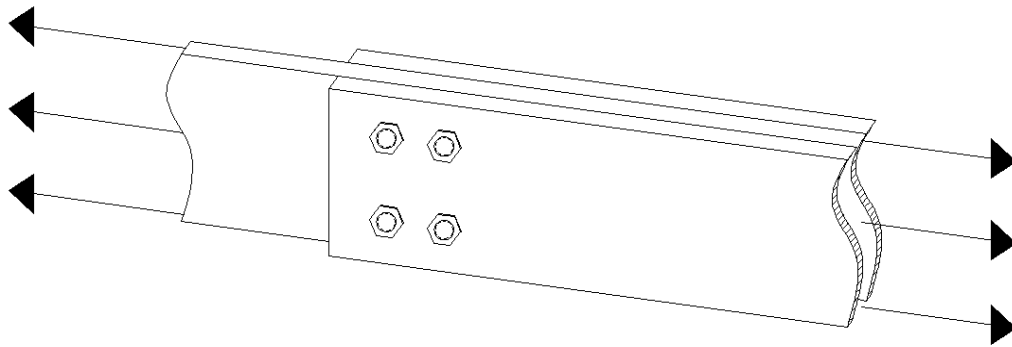


Figure 3-1: AASHTO (2007) Stress Category B detail

Fatigue specimens were classified as AASHTO Category B details so that approximate fatigue life, at know stress ranges, could be predicted. Estimates of fatigue life, taken from the AASHTO design curves (Figure 3-2), were useful in determining preliminary experimental stress ranges.

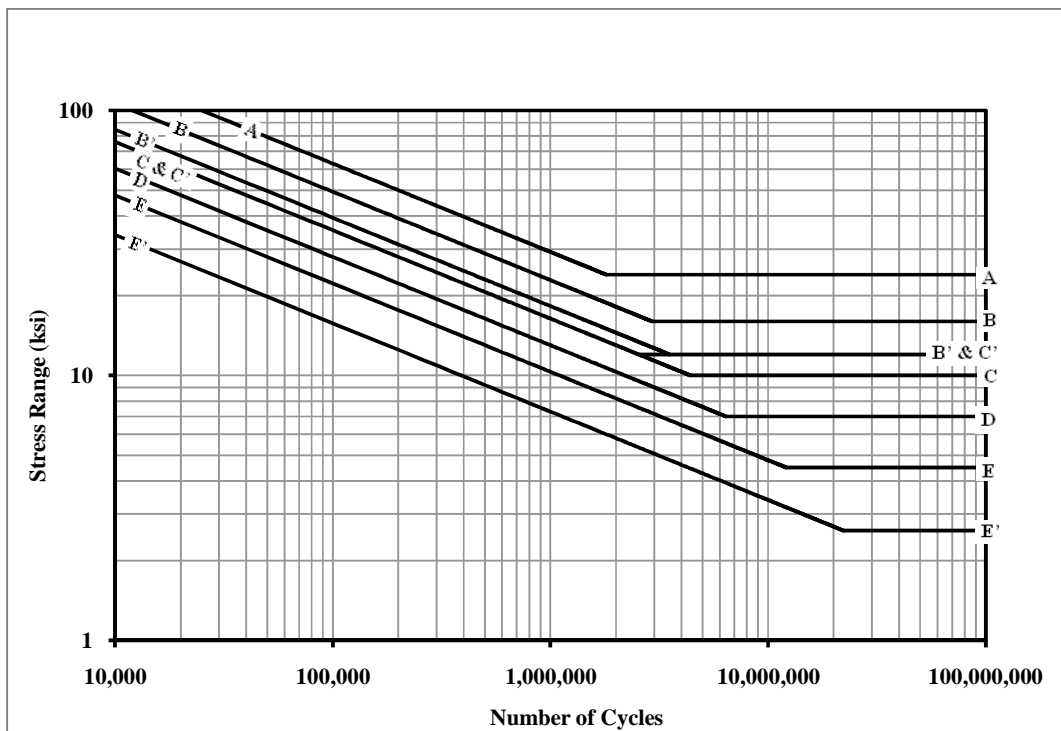


Figure 3-2: AASHTO Design stress range fatigue curves [34]

Fatigue life determined in the lab was not expected to match exactly with AASHTO design classifications. AASHTO design curves were developed for applications on full scale bridge members. Initial stress ranges investigated for this experimental program were selected based on theoretical fatigue life of an AASHTO Category B detail.

Fatigue specimens were designed to meet requirements outlined in American Society for Testing and Material (ASTM) test designation E 466-07 [33]. According to ASTM E 466-07 [33], due to the specialized nature of programs involving notched specimens, there are no limitations on the design of notched specimens. However, the notch, or hole geometry, must be reported and information associated with the stress concentrations occurring at the hole must be reported.

While ASTM E466-07 [33] has no limitations on the design of notched fatigue specimens, previous research has shown edge distance ratio to a significant effect on the levels of residual stress that can be induced through cold expansion as well as potential gains in fatigue life [19,26]. Past studies have shown that specimens with e/D ratios (e is the distance from the center of the hole to the edge of the plate and D is hole diameter) below 3 can result in insufficient surrounding material to control the plastic zone created through cold expansion, and compressive residual stresses fields are reduced. All fatigue specimens, tested as part of this research program, were designed with e/D ratios greater than 3.

3.1.1.1 3.18mm [0.125 in.] Fatigue Specimens

The first batch of fatigue specimens were designed using 50.80 mm x 3.18 mm [2.00 in. x 0.125 in.] Gr. A36 steel plate with a 3.18mm [0.125 in.] drilled and reamed hole located at the center of the specimens. The 3.18mm [0.125 in.] fatigue specimens, Figure 3-3 & Figure 3-4, were

designed to simulate an AASHTO Category B connection detail in accordance with the specimen design section outlined ASTM E 466-07.

The width of the plate at the location of the hole, equal to 31.8 mm [1.25 in.], corresponds to an e/D ratio of 5. This value of e/D exceeds the minimum e/D ratio shown to potentially affect residual stress fields in previous studies [19,26]. 3.18mm [0.125 in.] plate was chosen as this test programs preliminary plate thickness because with the small corresponding volume of steel, a low amount of power output would be required of the PICK tool. Given that the PICK tool was still at a developmental stage, a lower power demand was considered an appropriate starting place (corresponding to a reduced scale).

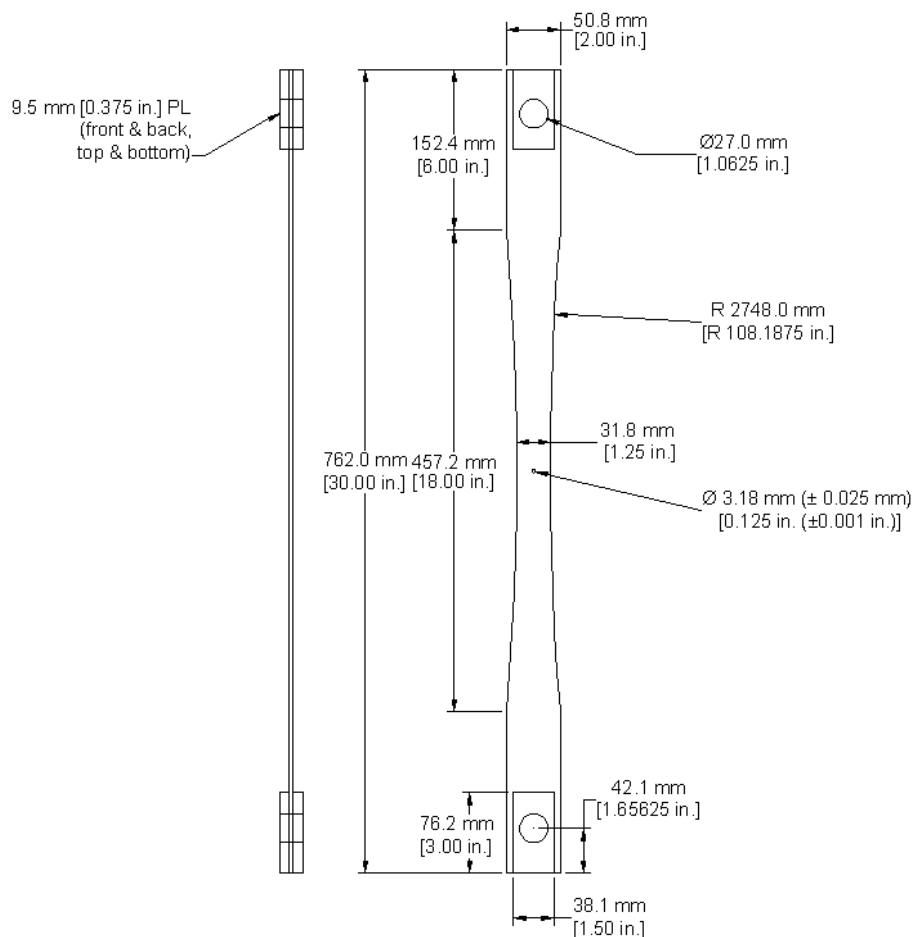


Figure 3-3: 3.18 mm [0.125 in.] Fatigue specimen detail



Figure 3-4 : 3.18mm [0.125in.] fatigue specimens, fabricated by Rice Precision Manufacturing, located in Baldwin, KS

The loading device used grips with 25.4 mm [1.00 in.] diameter pins to secure the specimens. Specimens were designed with 27.0 mm [1.0625 in.] holes drilled out of each end. In addition, two 76.2 mm x 38.1 mm x 9.5 mm [3.00 in. x 1.50 in. x 0.375in.] Gr. A36 steel plates were welded onto the surface of the 3.18mm [0.125 in.] Gr. A36 steel plate at the location of the 27.0 mm [1.0625 in.] holes (Figure 3-3). Additional plate thickness was provided to ensure the loading device would not cause specimens to tear out of the grips.

3.1.1.2 6.35 mm [0.250 in.] Fatigue Specimens

The 6.35 mm [0.250 in.] fatigue specimens were designed to more closely simulate the thickness of a web in an actual bridge girder. In addition, verification that the PICK tool concept could work on specimens with increased thickness provided assurance that the concept could be extended to future 3D test configurations. The 6.35 mm [0.250 in.] specimens were made from 50.8 mm x 6.35 mm [2.00 in. x 0.250 in.] Gr. A36 steel plate. A 6.35 mm [0.250 in.] hole was

drilled and reamed at mid-height (Figure 3-5). Due to the increase in hole diameter over the 3.18mm [0.125 in.] specimens, the width of the plate was increased to 44.5 mm [1.75 in.] at the location of the hole to ensure an adequate e/D ratio. A width of 44.5 mm [1.75 in.] corresponds to an e/D ratio of 3.5; greater than the value found to effect levels of residual stress fields and fatigue life [19,26].

Similar to the 3.18mm [0.125 in.] fatigue specimens, the 6.35 mm [0.250 in.] fatigue specimens were detailed to properly fit in the grips of the loading device. This was accomplished by drilling 27.0 mm [1.0625 in.] holes from each end of the specimens (Figure 3-5) and welding two 76.2 mm x 50.8 mm x 6.35 mm [3.00 in. x 2.00 in. x 0.250 in.] Gr. A36 steel plates at the locations of the 27.0 mm [1.0625 in.] holes.

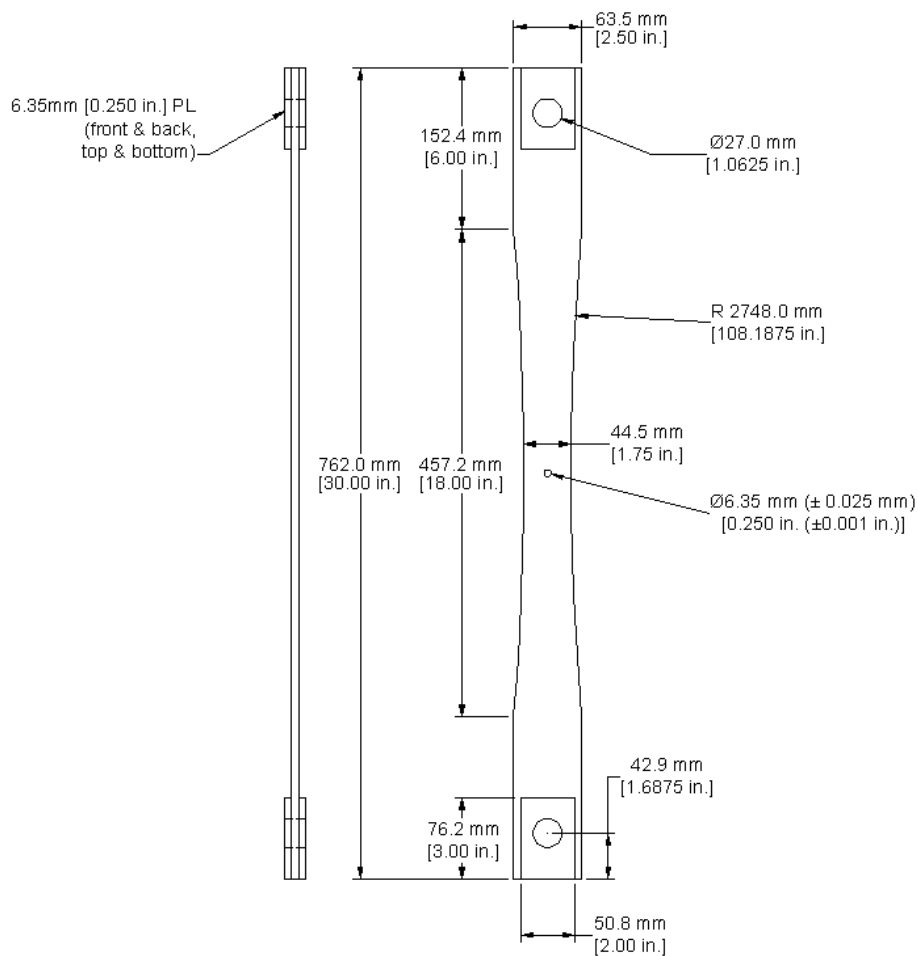


Figure 3-5: 6.35 mm [0.250 in.] Fatigue specimen detail

3.1.2 Specimen Fabrication

All specimens were fabricated at Rice Precision Manufacturing in Baldwin City, Kansas. To ensure smooth surfaces on the inside face of the centered holes, holes were drilled and reamed to size. Any additional burs were removed from the holes edges using a chamfering tool.

Once the proper hole diameters were met, dimensions were verified with bore micrometers.

Specimens were received from Rice Precision Manufacturing with mill scale remaining on the surface. The specimens were sand blasted with Balotini Impact Beads, Size AD, 70-140 US Sieve sand. Sand blasting was followed by coating with a layer of a workable fixative paint to help prevent corrosion.

3.2 FATIGUE TESTING METHODS

3.2.1 Test Groups

Specimens of both thicknesses were divided into two groups, treated and control. Both groups were tested at equivalent stress ranges. Fatigue lives of both groups were evaluated and a preliminary fatigue life improvement factor was established for the PICK tool.

3.2.2 Stress Ranges

Stress ranges used for this test program were established both by referencing the AASHTO fatigue design curves and through experiential verification [34]. The AASHTO LRFD Bridge Design Specification (2007) groups details at risk to load-induced fatigue cracking into eight categories: Category A; Category B; Category B'; Category C; Category C'; Category D; Category E; and Category E' (categories listed from longest to shortest fatigue life). Specific components and details are assigned to one of the eight categories, typically through a member

or components detailed geometry. Further information on how to utilize AASHTO design curves can be found in works by Barsom and Rolfe [12] and Fischer [32].

The AASHTO (2007) fatigue design curve (Figure 3-6) was used to select stress ranges corresponding to reasonable design fatigue lives for a Category B detail. The five preliminary stress ranges investigated were: 138 MPa [20.0 ksi]; 164 MPa [24.0 ksi]; 193 MPa [28.0 ksi]; 207 MPa [30.0 ksi] and 221 MPa [32.0 ksi] at R values of 0.091, 0.077, 0.067, 0.063 and 0.059, respectively. Laboratory investigation showed that stress ranges from 193-221 MPa [28.0-32.0 ksi] resulted in reasonable fatigue life of control specimens. A stress range of 221 MPa [32.0 ksi] was used for the majority of testing to date for the test program.

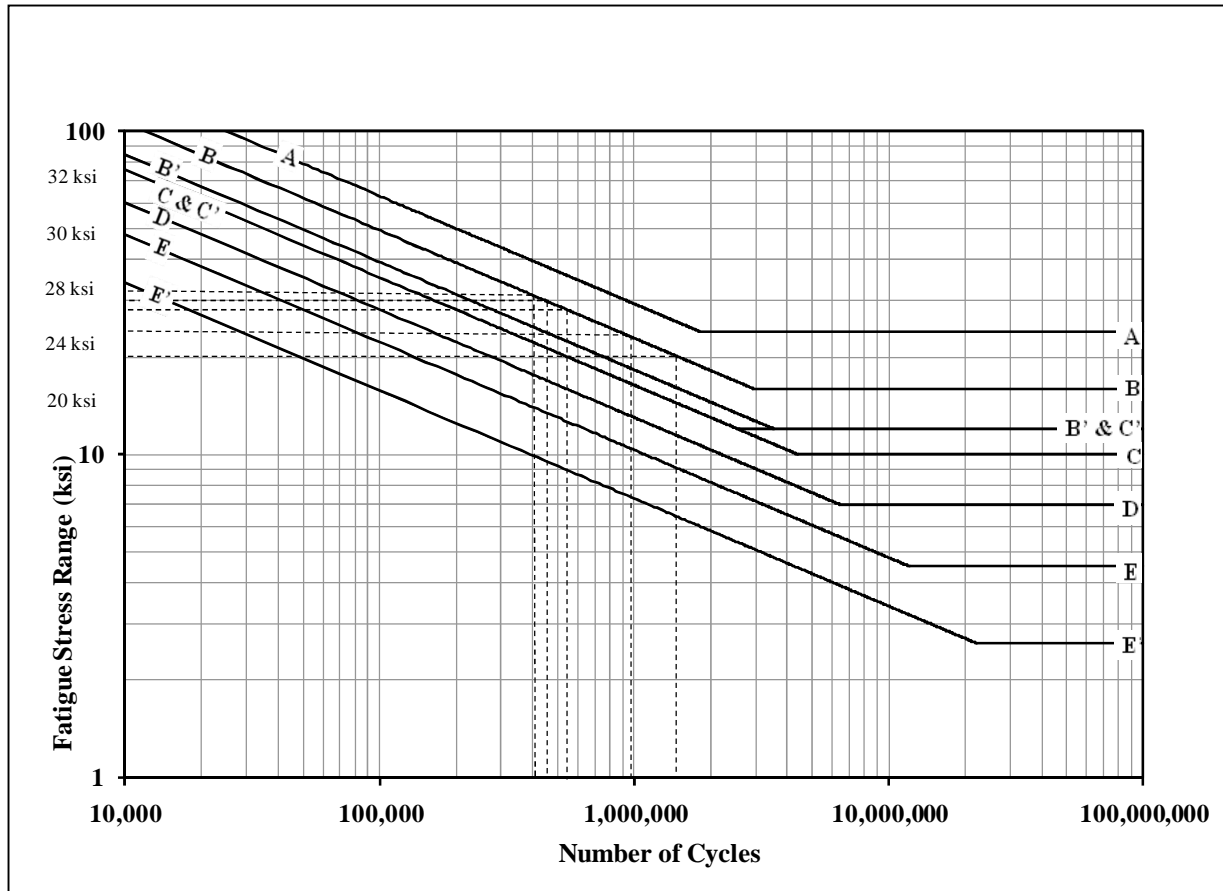


Figure 3-6: AASHTO Design stress range curves for Categories A to E' [34]

3.2.3 Loading Methods

Load ranges were determined first by measuring exact dimensions of each specimen at the location of the hole. Width, thickness and hole diameter were measured using digital calipers, dimensions were rounded off in accordance with ASTM E466-07 [33]. According to ASTM E466-07 [33], dimensions equal to or greater than 5.08 mm [0.200 in.] values should be rounded to the nearest 0.030 mm [0.001 in.] and dimensions less than 5.08 mm [0.200 in.] rounded to the nearest 0.0130 mm [0.0005 in.]. Net area could then be calculated at the location of the hole. The calculated net area was used to solve for an appropriate load range to match the target stress range.

Controlling bending stress, particularly in the 3.18 mm [0.125 in.] thick specimens, proved to be a challenge. ASTM E 466-07 details a procedure to verify acceptable alignment of the test equipment to control levels of bending. The verification technique involves installing fatigue grade strain gages on all four sides of a “control specimen” with a rectangular cross section. According to ASTM E 466-07, “The bending stress (strains) so determined on...the rectangular cross section specimen should be limited to less than 5% of the greater of the range, maximum or minimum stresses (strains), imposed during any test program.”[33]

For this test program, instead of measuring stresses (strains) on a “control specimen” with a rectangular cross section, bending stress was monitored for each individual specimen by placing strain gages on both sides of the specimens at the location of minimum width (mid-height (Figure 3-7)). Bending stress was monitored throughout the life of each test and kept as close to or below five percent of the maximum stress. Bending stress was monitored for each specimen to ensure consistent stress ranges were applied to each specimen. Bending stress was calculated using Eq. (3-1):

$$\sigma_{bending} = \frac{\varepsilon_1 - \varepsilon_2}{2} \times E \quad (3-1)$$

where ε_1 and ε_2 represent the maximum and minimum strain measurements obtained from the strain gages placed on both sides of each specimen (Figure 3-7), and E is the modulus of elasticity measured in tension tests, Section 3.5.

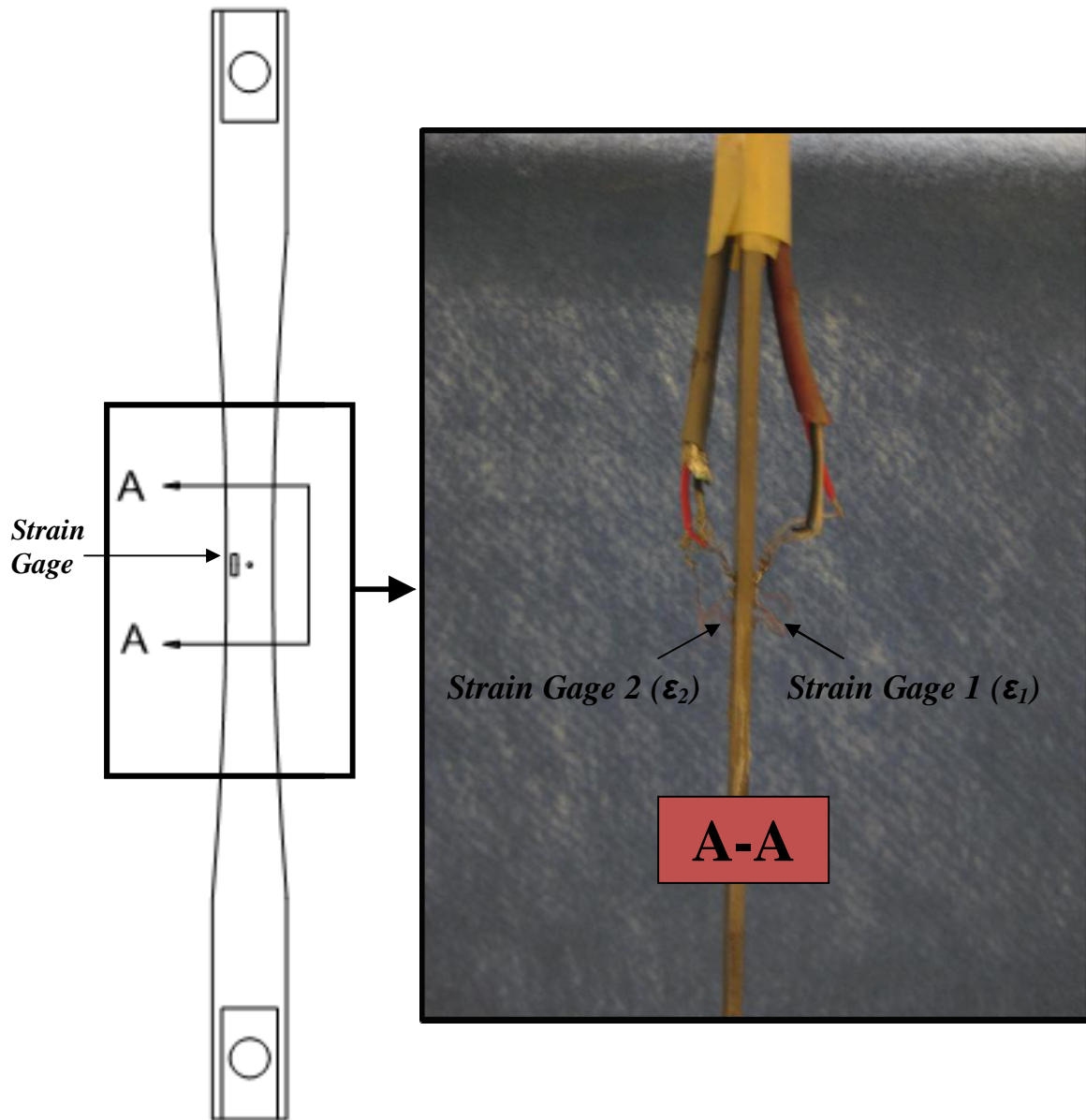


Figure 3-7 3.18 mm [0.125 in.] fatigue specimen with strain gages to monitor bending stress

Initial results for bending stress levels were as high as 137.9 MPa [20.0 ksi]. Several test parameters were investigated to determine the cause of these high bending stresses. It was concluded that two factors were causing much of these unusually high bending stresses. The first was the alignment of the testing equipment grips. As seen in Figure 3-8, the grips were misaligned by approximately 4.76 mm [0.1875 in.]. The load frame was adjusted to eliminate

the misalignment of the grips. Properly aligning the grips of the load frame significantly reduced bending stress; however, bending stresses remained slightly higher than the five percent suggested limit.

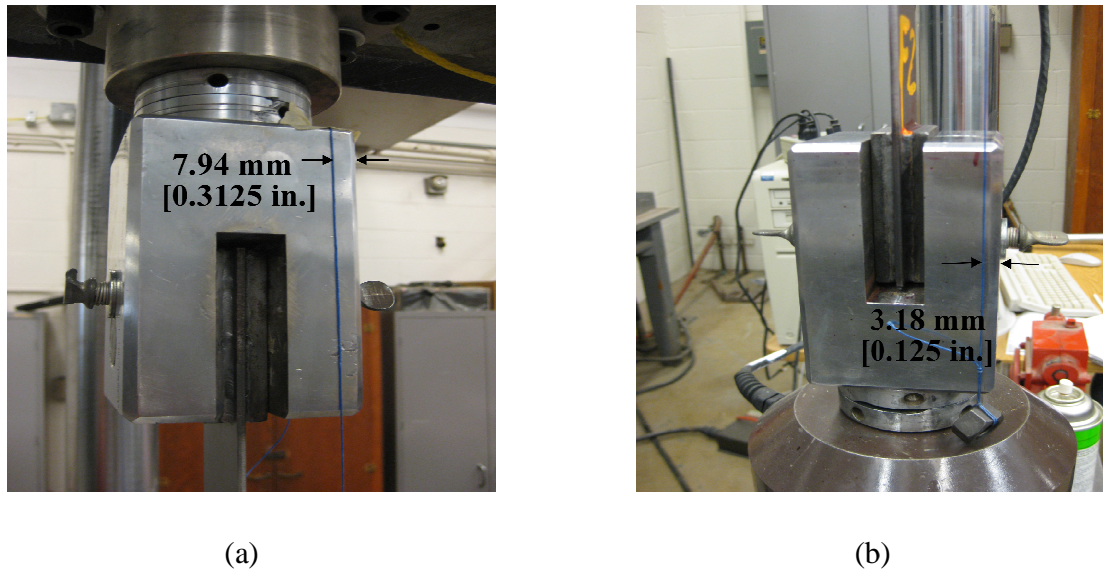


Figure 3-8: Misalignment of fatigue test equipment (a) upper grip, (b) lower grip

It was concluded that the slenderness of the 3.18 mm [0.125 in.] thick specimens was the additional parameter causing high levels of bending stress. Even though the fatigue specimens were loaded in tension, a thickness of 3.18 mm [0.125 in.] proved insufficient in preventing out of plane bending for a 762 mm [30.00 in.] unbraced length. The 6.35 mm [0.250 in.] thick fatigue specimens, having the same unbraced length as the 3.18 mm [0.125 in.] thick specimens, did not experience large levels of bending stress under the same test conditions. It proved necessary to develop a bending control system for the 3.18 mm [0.125 in.] thick specimens.

To reduce bending stresses in the 3.18 mm [0.125 in.] thick specimens, an external apparatus was devised. ASTM E 466-07 allows for externally applied mechanism to be used to

control bending levels so long as the apparatus does not affect fatigue life results. The bending control device developed in this test program consisted of a series of cables, ferrules and turnbuckles (Figure 3-9). The device could be used as the test was in progress. If high levels of bending stress were detected at any point during a test, the turnbuckles were adjusted to equalize the stresses seen on both sides of the specimen. The bending stress control apparatus proved successful in limiting bending levels to approximately five percent of the maximum applied stress.

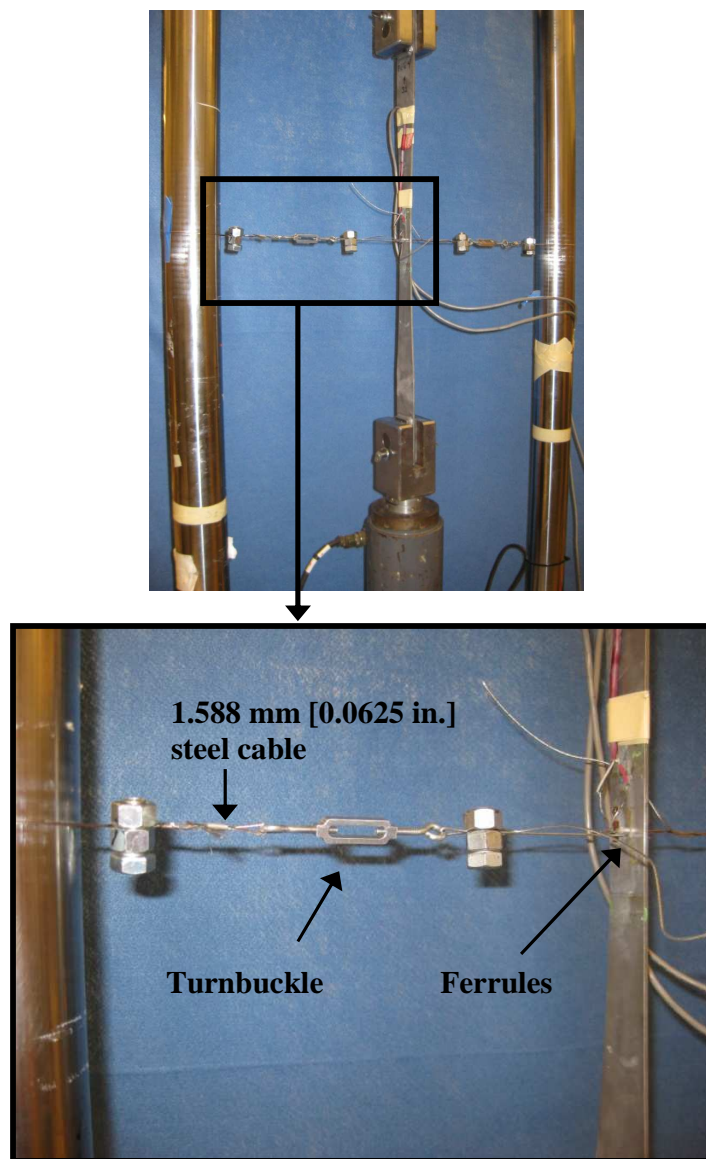


Figure 3-9: Bending stress control apparatus

3.2.4 Testing Equipment

3.2.4.1 MTS Load Frame

The testing machine used for the bulk of the fatigue and tension testing was a MTS Model No. 204.26 Servo Ram. The servo-controlled actuator had a 127 mm [5.00 in.] stroke length with a 160 kN [35,000 lb] force rating, and was supported by a two column MTS Model No. 312.31 load frame with 222 kN [50 kip] capacity.

The MTS user interface, TestStar, was used to write the fatigue testing procedures. A detailed procedure can be found in Appendix A of this report. Two different load cells were used in this experimental program. The load cell used for the 3.18 mm [0.125 in.] specimens was a MTS Model No. 661.20E-02 single bridge force transducer; it had a capacity of ± 50 kN [$\pm 11,000$ lb]. The 6.35 mm [0.250 in.] specimens required the application of loads larger 50 kN [11,000 lb]. A MTS Model No. 661.22 single bridge force transducer with a capacity equal to ± 222 kN [$\pm 50,000$ lb] was used for the 6.35 mm [0.250 in.] specimens.

3.2.4.2 Instron Load Frame

An Instron model 1334 closed-loop servo-hydraulic testing system was used for a small number of preliminary fatigue tests. Details regarding the user interface and operation of the Instron Load Frame can be found in Vilhauer et.al. [29].

3.2.4.3 Baldwin Load Frame

The 3.18 mm [0.125 in.] thick tension specimens were tested using a Baldwin 120 test frame. The test frame used an Intron Model 5500 R 120 BTE actuator with a capacity of ± 534 kN [± 120 kip]. The user interface software, Partner, was used to create the tension test program for the

3.18 mm [0.125 in.] specimens. The tension testing procedure used can be found in Appendix B of this report.

3.2.5 Fatigue Test Parameters

The fatigue test parameters followed those outlined in ASTM E 466-07. A summary of the test parameters and properties of each fatigue specimen can be found in Chapter 4 of this report.

Sinusoidal waveforms were used to load the fatigue specimens using both the Intron and MTS test machines. Procedures written for each testing machine began by defining maximum load, minimum load, average load and test frequency. Stress amplitudes were monitored at all times during testing and were kept within the required $\pm 2\%$ of the desired test force amplitude.

Preliminary control fatigue specimens were tested at stress ranges of 138 MPa [20.0 ksi], 164 MPa [24.0 ksi], 193 MPa [28.0 ksi], 207 MPa [30.0 ksi] and 221 MPa [32.0 ksi]. The majority of the specimens were tested at 193 MPa [28.0 ksi] and 221 MPa [32.0 ksi]. While target stress range was held constant for individual specimens, load inputs varied between specimens due to minor differences in net section at the location of the holes.

As a measure of simplification, the same minimum stress was used for all specimens, 13.8 MPa [2.00 ksi]. The stress ratio, R , representing the relative magnitude of the minimum and maximum stress in each cycle, varied for the assorted load ranges as a result of the unchanged minimum stress of 13.8 MPa [2.00 ksi] [12]. The AASHTO LRFD Bridge Design Specification (2007) considers stress range, not maximum or minimum stress, as the controlling factor for fatigue life.

Testing frequency had a noticeable influence on bending stress experienced by the 3.18 mm [0.125 in.] fatigue specimens. A significant increase was seen in bending stress levels as test frequency was increased. ASTM E 466 -07 states that fatigue strength is unaffected when

loaded at frequencies ranging from 10^{-2} Hz to 10^{+2} Hz. Therefore, a test frequency needed to be selected that would minimize bending stress and fall in the range outlined by ASTM E 466-07. Initial fatigue testing was performed at a test frequency of 2 Hz. At this frequency bending stress was low and easy to maintain (with the use of the apparatus discussed in Section 3.2.3). While uncontrolled bending was not an issue at this test frequency, long time periods were required to complete fatigue tests. Higher frequencies were investigated starting with a test frequency of 10 Hz. The time of the test was significantly reduced; however, bending stresses experienced at this test frequency were significantly higher and more difficult to control. It was determined, through experimental investigation, that a test frequency of 3 Hz, given the experimental setup, was the highest frequency that could be used to maintain low bending stresses.

At the onset of each new fatigue test, bending stress was measured and, if necessary, lowered to approximately five percent of the maximum applied stress. Once acceptable initial levels of bending stress were achieved, bending stress was closely monitored and recorded twice a day to ensure a consistent stress range applied to the fatigue specimens throughout the test.

3.3 FATIGUE TEST INSTRUMENTATION

3.3.1 Strain Gages

Precision strain gages were used to measure bending stress present in the fatigue specimens. The strain gages were manufactured by Vishay Micro-Measurements having designation WK-06-250BG-350. The strain gage was comprised of fully encapsulated K-alloy gages with high-endurance lead wires. WK- series strain gages were selected because of their high fatigue life, compact size and wide range of operating temperatures. The gages had a grid resistance of $350 \pm 0.3\%$ ohms and a gage factor equal to $2.03 \pm 1.0\%$. The gage length and geometry were of

designation 250BG. A detailed data sheet of the 250BG strain gage can be found in Appendix C of this report.

3.3.2 Strain Gage Installation

All strain gage installation procedures, including surface preparation, strain gage application, wire preparation, and wire soldering were performed using Vishay Micro-Measurement Technical notes [35-37]. An installed strain gage is shown in Figure 3-10.

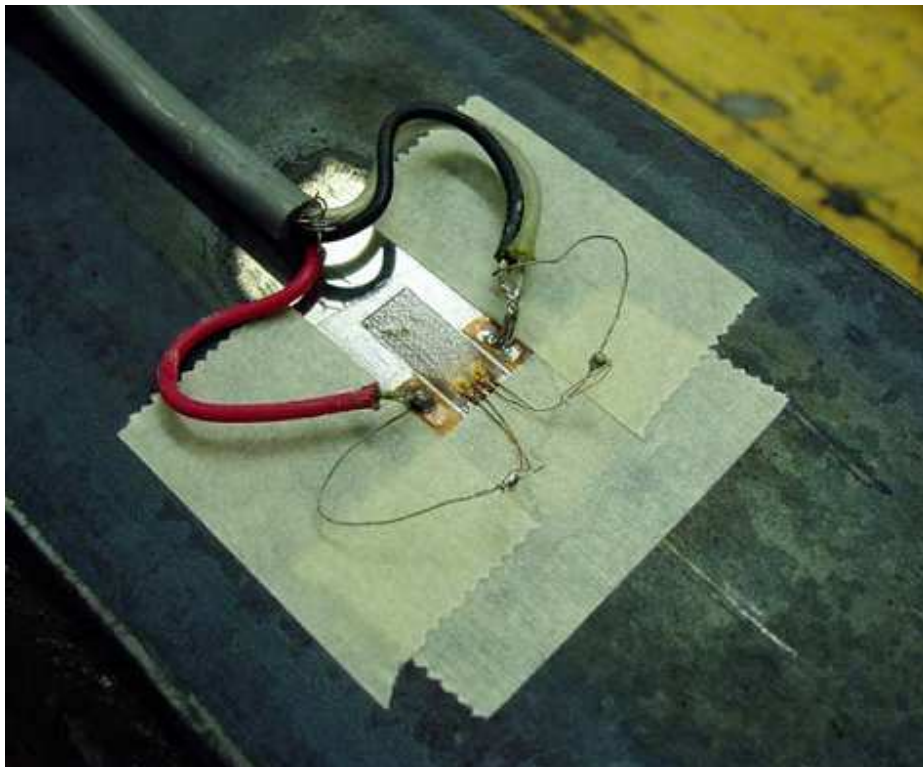


Figure 3-10: Installed strain gage

3.3.3 Data Acquisition

3.3.3.1 WaveBook Data Acquisition System

Three data acquisition systems were used in this experimental program. The first was an Iotech WaveBook/516 16 bit, 1 MHz, data acquisition system, Figure 3-11. The Wavebook/516 was a user friendly acquisition system due to its mobility and easy to use PC based software, WaveView. The acquisition system had the ability to simultaneously record up to 24 channels of strain input. A piece of plywood supported 13 sets of quick-connect terminals to allow for simple and quick connection between the strain gages and the data acquisition system.

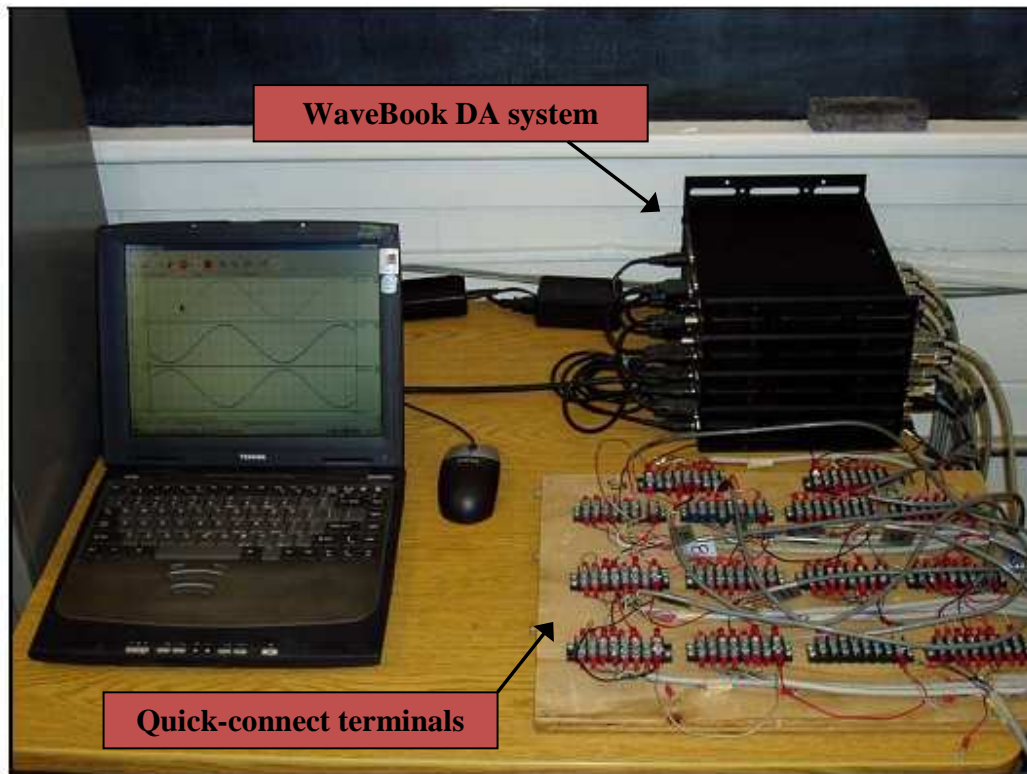


Figure 3-11: WaveBook data acquisition system test configuration

The scope window of WaveView was utilized to observe strain, load, and displacement readings immediately after the data collection had completed. It was convenient to use this feature to monitor bending stress. If bending stress became large, data would be immediately

available after the predefined reading time had been completed and the bending control apparatus could be adjusted accordingly.

The WaveBook had the ability to work with full, one-half and one-quarter wheatstone bridges. For the fatigue testing portion of this program, one-quarter wheatstone bridges were utilized. The quarter bridges had three 350Ω interior resistors and excitation voltages of 10 V. Before recording data with WaveBook, shunt calibrations were performed to calibrate the gages. Calibration was performed using internal shunt resistances of $34.65\text{ k}\Omega$ supplied by the WaveBook. The calibration used a gage correction factor of 2.03. This value for gage correction was supplied by Vishay Micro-Measurements [38].

3.3.3.2 *EBRT Data Acquisition*

The second data acquisition system used for this test program was the EBRT 2432 (Figure 3-12). The EBRT acquisition system is a small lightweight system with the capability of simultaneously sampling at 100,000 Hz per channel with 32 channels of input. The EBRT 2432 connected to the computer using a standard TCP/IP protocol for wired Ethernet communications.

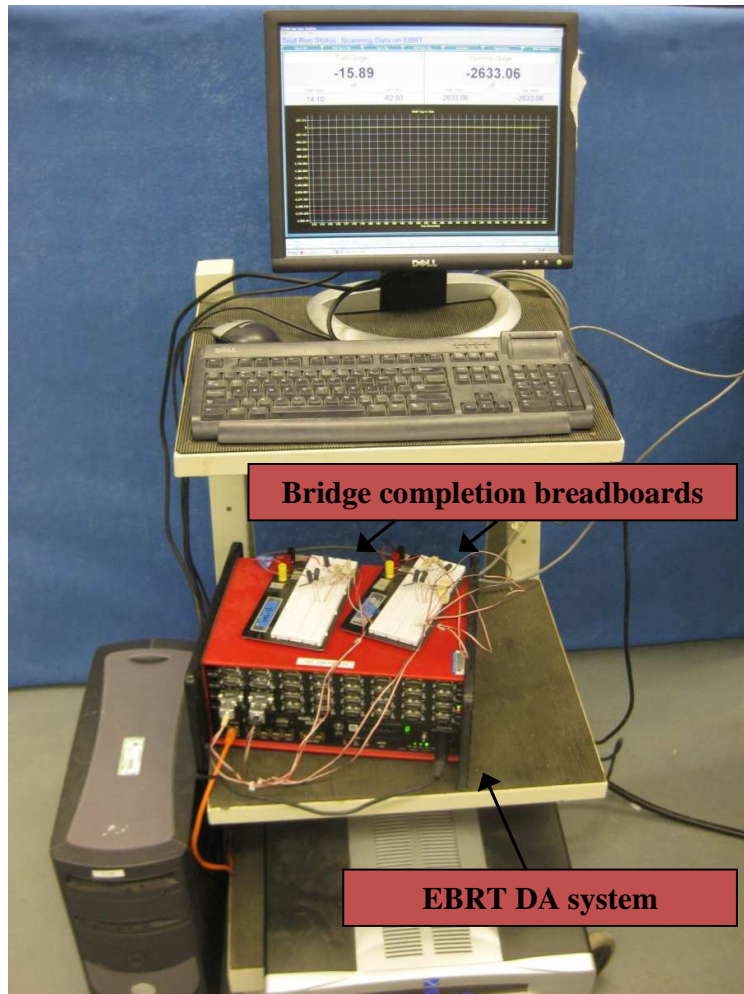


Figure 3-12: EBRT 2432 data acquisition system test configuration

The EBRT 2432 provided a number of verification methods to confirm the accuracy of laboratory measurements. One example is the equipment verification (VCAL) in which a voltage signal is sent to the front of the input channels to verify accurate gains. In addition to verifying the accuracy of recorded data, the EBRT system allowed for real time data to be viewed in multiple graph formats. This feature made the EBRT extremely efficient in monitoring bending levels in the axial fatigue specimens.

The EBRT system was capable of being connected to a number of different sources, however, the only sources necessary for testing in this report were a 9-Pin D-Sub Connector to

BNC, used with voltage sources, and a 9-Pin D-Sub Connector to quarter bridge sensors. For each device, a specialty connection was built to convert the signal so that the EBRT system was able to properly recognize the component. Details concerning how to properly construct the converters can be found in the Technical Manual for the EBRT 2432. The EBRT system was not used for a large number of fatigue tests. The reason for its limited use was the ability of the EBRT to sample data at such high frequencies, up to 100,000 Hz. The use of the EBRT was better served for test configurations requiring higher sampling frequencies than required for the fatigue tests.

3.3.3.3 *National Instruments Data Acquisition*

The third data acquisition system used for this test program was a National Instruments model NI 9219, 4-Channel, 24-Bit, Universal Analog Input Module (Figure 3-13). The NI 9219 had four 6-terminal spring-terminal connectors.

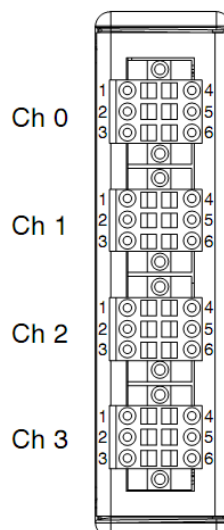


Figure 3-13: NI 9219, 4-Channel, 24-Bit, Universal Analog Input Module [39]

The use of more than four channels was often required during testing. As a result, many test configurations involved docking multiple NI 9219 modules into a model NI cDAQ-9172 chassis (Figure 3-14). The NI cDAQ-9172 chassis provided eight slots for any C Series I/O modules. The chassis was capable of reading a broad range of digital and analog inputs using a high-speed USB 2.0 interface.

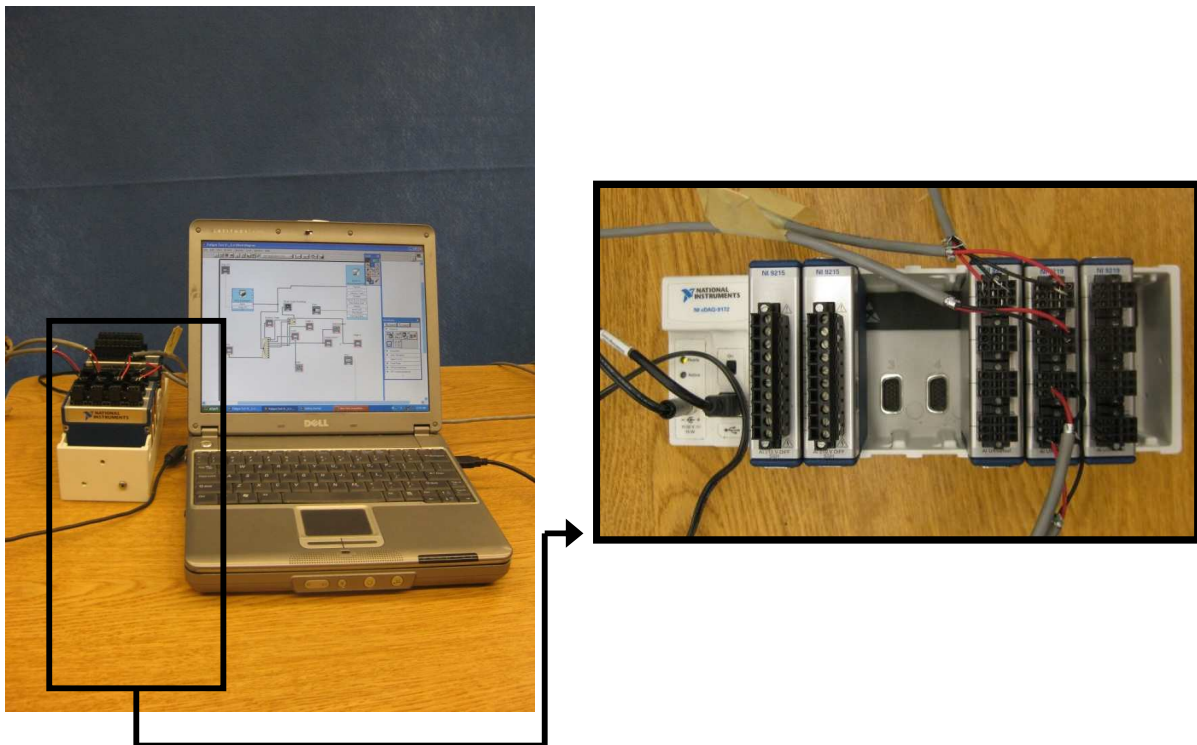


Figure 3-14: National Instruments Data Acquisition System Test Configuration

The test program for the NI 9219 data acquisition system was written in National Instruments LabVIEW 8.6. LabVIEW, short for Laboratory Virtual Instrument Engineering Workbench, is an interactive program development and execution system. It is user friendly software allowing the user to create programs capable of working with a variety of instrument functions. A number of sample LabVIEW programs are provided with the LabVIEW software, providing a convenient starting point for first-time LabVIEW users. Once a test program was

written in LabVIEW it could be saved and used on any computer with a compatible version of LabVIEW. The data acquisition setup, shown in Figure 3-14, was convenient for lab testing due to the portable nature of the hardware.

3.3.3.4 *Recorded Data*

Two sets of data were recorded throughout the life of the fatigue specimens. The first set of data, collected through the three various data acquisition systems, monitored and recorded levels of bending stress (strain). Bending stress levels were calculated using Eq. (3-1). In addition to recording bending stress (strain) from the active gages, readings were taken from a “dummy gage” that was mounted to a stationary specimen to ensure electronic noise was not affecting results.

The second set of data, recorded throughout the duration of the test, was axial displacement and axial force collected with the MTS controller’s data acquisition system. The load data was carefully analyzed for each tested specimens to verify that the load output stayed within $\pm 2\%$ of the load range command.

3.4 FATIGUE CRACK DETECTION

Test termination, as defined by ASTM E466-07 [33], states that a fatigue test shall be continued “...until the specimen failure criteria is attained or a predetermined number of cycles has been applied to the specimen. Failure may be defined as complete separation, as a visible crack at a specified magnification, as a crack of certain dimensions, or by some other criterion...” For this test program, a specimen was considered “failed” when a crack of any size was detected using a dye penetrant crack detection system. A similar dye penetrant crack detection scheme was used by Villhauer et. al. [29].

The dye penetrant crack detection system was used in this test program in place of continuous monitoring for crack initiation. The dye penetrant crack detection system involved the use of the limit detector function in the MTS Station Manager software. As shown in Figure 3-15, the runtime user interface of the Station Manager program allowed for maximum and minimum axial forces and axial displacements to be monitored and continuously updated throughout the life of the test. As the test was in progress, upper and lower bounds of axial displacement and axial force remained fairly constant. It was therefore possible to set limit detectors (Figure 3-16) to values just above the maximum axial displacement so that the test program would interlock (terminate), once a predefined maximum displacement was exceeded. The limit detectors allowed for any sudden increase in displacement between the cross heads to result in immediate pausing of the test. Typically the maximum axial displacement detector was set to approximately 0.127 mm [0.005 in.] above the maximum axial displacement reading in the runtime user interface. If at any point during the test the upper limit detector was triggered the specimen was removed and checked for cracks using dye penetrant. This method proved effective in detecting cracks in early stages of initiation. Cracks were typically detected before they became longer than 2.54 mm [0.10 in.].

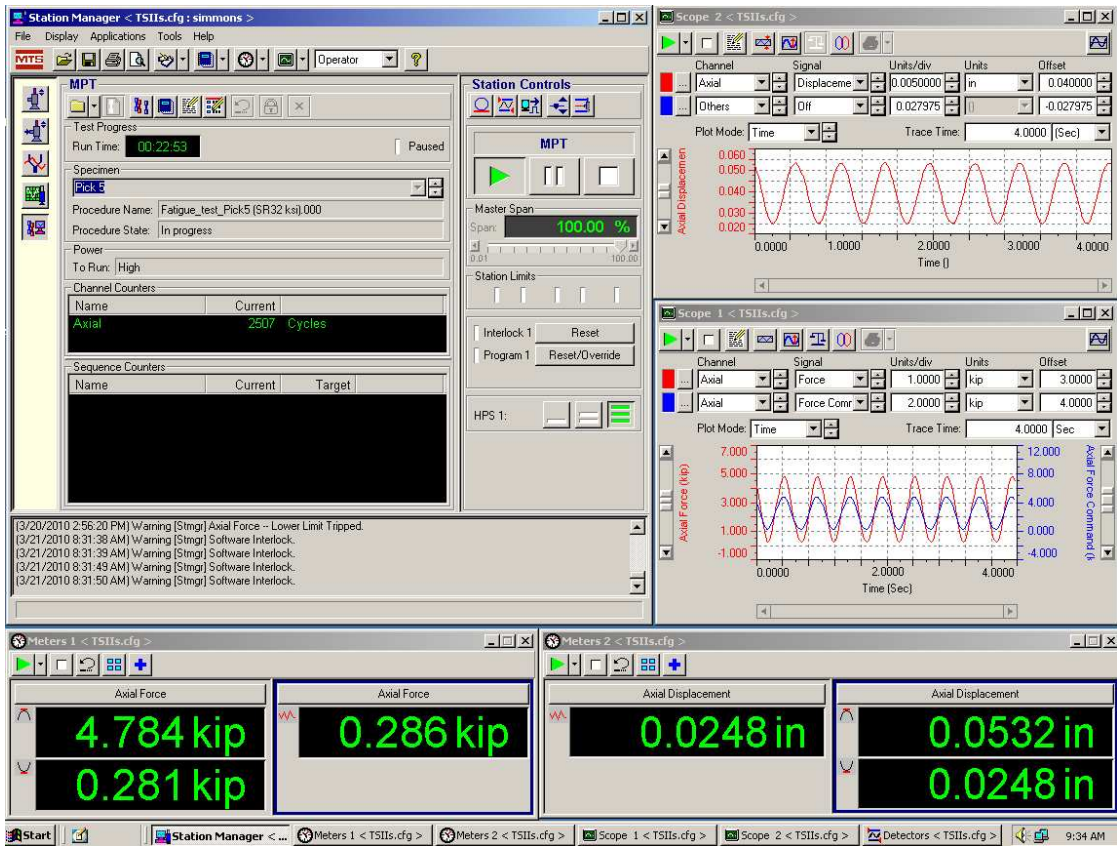


Figure 3-15: MTS TestStar Station Manager runtime user interface

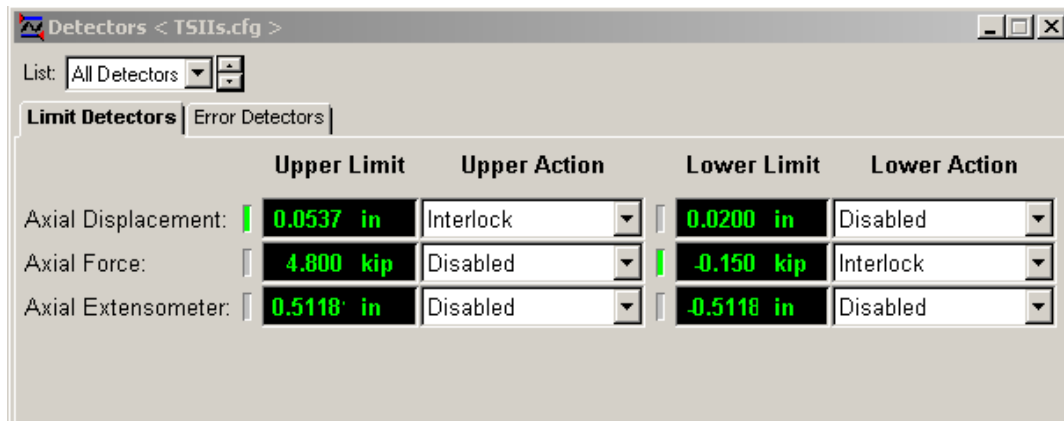


Figure 3-16: MTS TestStar Station Manager limit detector user interface

3.5 TENSILE TESTING

Establishing material properties of the plate used to construct the fatigue specimens, Section 3.1, was necessary for two reasons: (1) FEM material definition and (2) bending stress calculations. Tensile testing was performed on two plate thicknesses, 3.18 mm [0.125 in.] and 6.35 mm [0.250 in.]. All tension testing was performed in accordance with ASTM E8-04 Standard Methods for Tension Testing of Metallic Materials [40]. This included specimen design, illustrated in Figure 3-17 and Figure 3-18, which followed ASTM E8-04 criteria for standard rectangular specimens.

Loading rates outlined in ASTM E8-04[40] were closely followed for all specimens. A detailed summary of testing procedures used for specimens of both thicknesses can be found in Appendix B of this report.

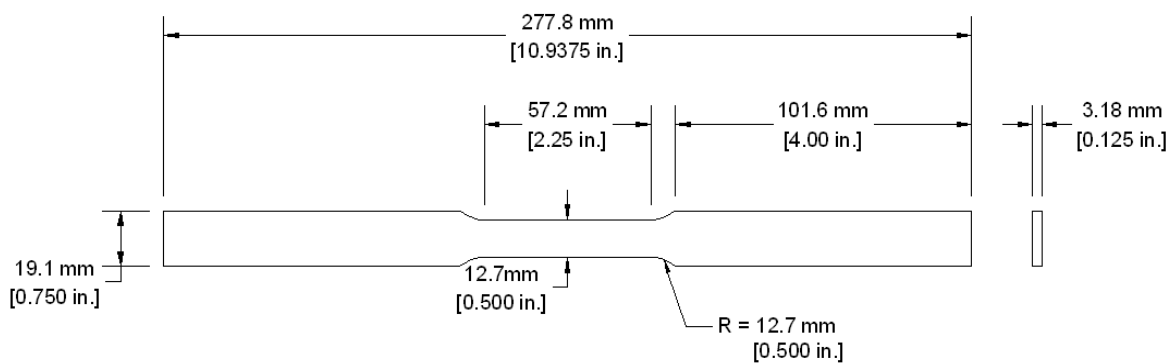


Figure 3-17: 3.18 mm [0.125 in.] Standard tension specimens

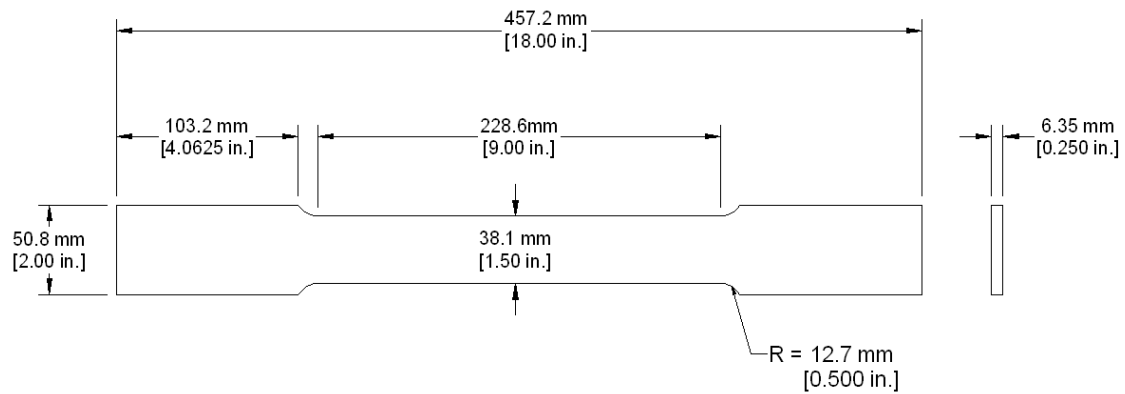


Figure 3-18: 6.35 mm [0.250 in.] Standard tension specimens

Data for applied force was collected through voltage outputs from the load cell. Strain data was measured using two devices: an Epsilon model 3542-0200-050-ST axial extensometer and strain gages (Section 3.3.1) applied to both sides of the tension specimens. The axial extensometer had a gage length of 50 mm [2.00 in.] and the capability of recording strain anywhere from -10% to +50%. The extensometer met all ASTM requirements for accuracy making it satisfactory for use in standard metallic tension testing as outlined by ASTM E8-04. Strain gages were used to confirm the readings of the extensometer up to the point of yielding. Upon onset of yielding, the strain gages would crack and lose their resistance. Final test configurations are shown in Figure 3-19 and Figure 3-20. Tabular results of the tension tests can be found in Chapter 4 and detailed stress strain diagrams for each test can be found in APPENDIX B.

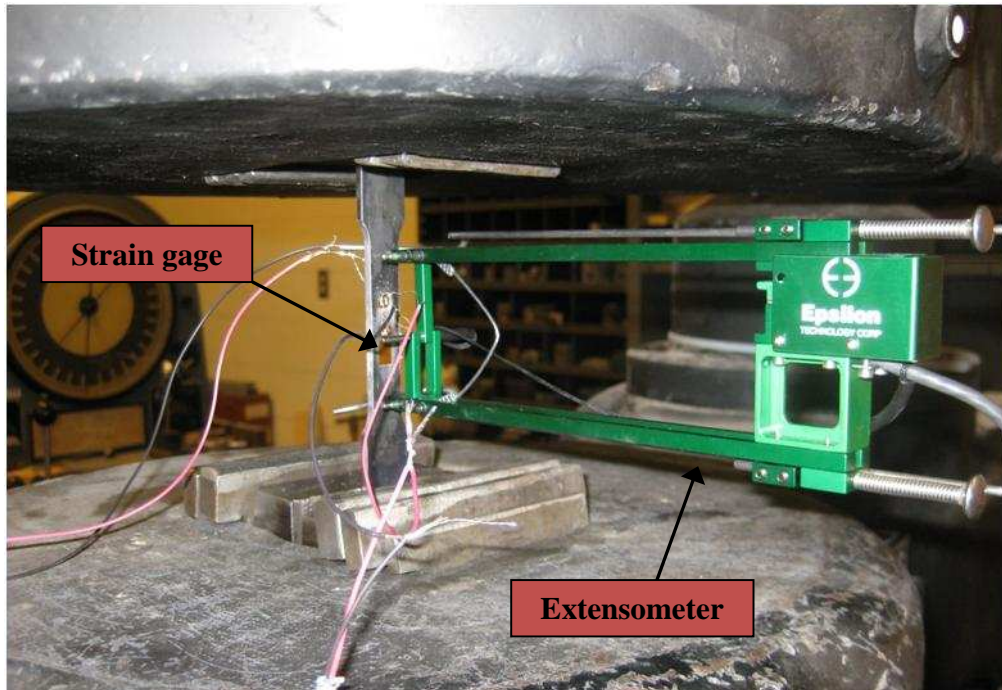


Figure 3-19: Tension test configuration 3.18 mm [0.1250 in.] thick specimens

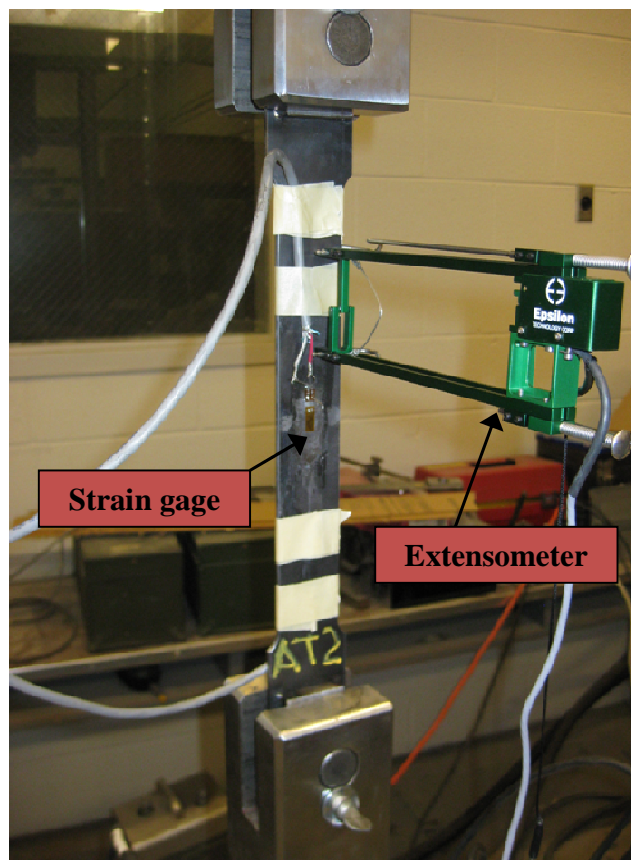


Figure 3-20: Tension test configuration 6.35 mm [0.250 in.] thick specimens

CHAPTER 4 EXPERIMENTAL RESULTS

4.1 FATIGUE SPECIMENS

The following section summarizes the results of the fatigue tests performed on 3.18 mm [0.125 in.] thick axially loaded specimens both with and without PICK tool treatment. As mentioned in Section 3.4, failure was defined as the visual detection of a flaw of any size, typically detected using the limit detector function on the MTS user interface, TestStar, then verified with dye penetrant.

4.1.1 Fatigue Life of Control Fatigue Specimens

As discussed in Section 3.2.2, several initial stress ranges were investigated to determine an appropriate test stress range. The target stress ranges investigated were: 138 MPa [20.0 ksi]; 164 MPa [24.0 ksi]; 193 MPa [28.0 ksi]; and 221 MPa [32.0 ksi]. Results from the preliminary stress range tests are shown in Figure 4-1 and Table 4-1. A final stress range of 221 MPa [32.0 ksi] was selected and used for comparison against the PICK treated specimens due to the level consistency achieved (a standard deviation of 25,340 cycles) and relatively short fatigue lives (average life 194,000 cycles) of the control specimens tested at 221 MPa [32.0 ksi]. Photographs and initial flaw sizes of the failed fatigue specimens can be found in APPENDIX D of this report.

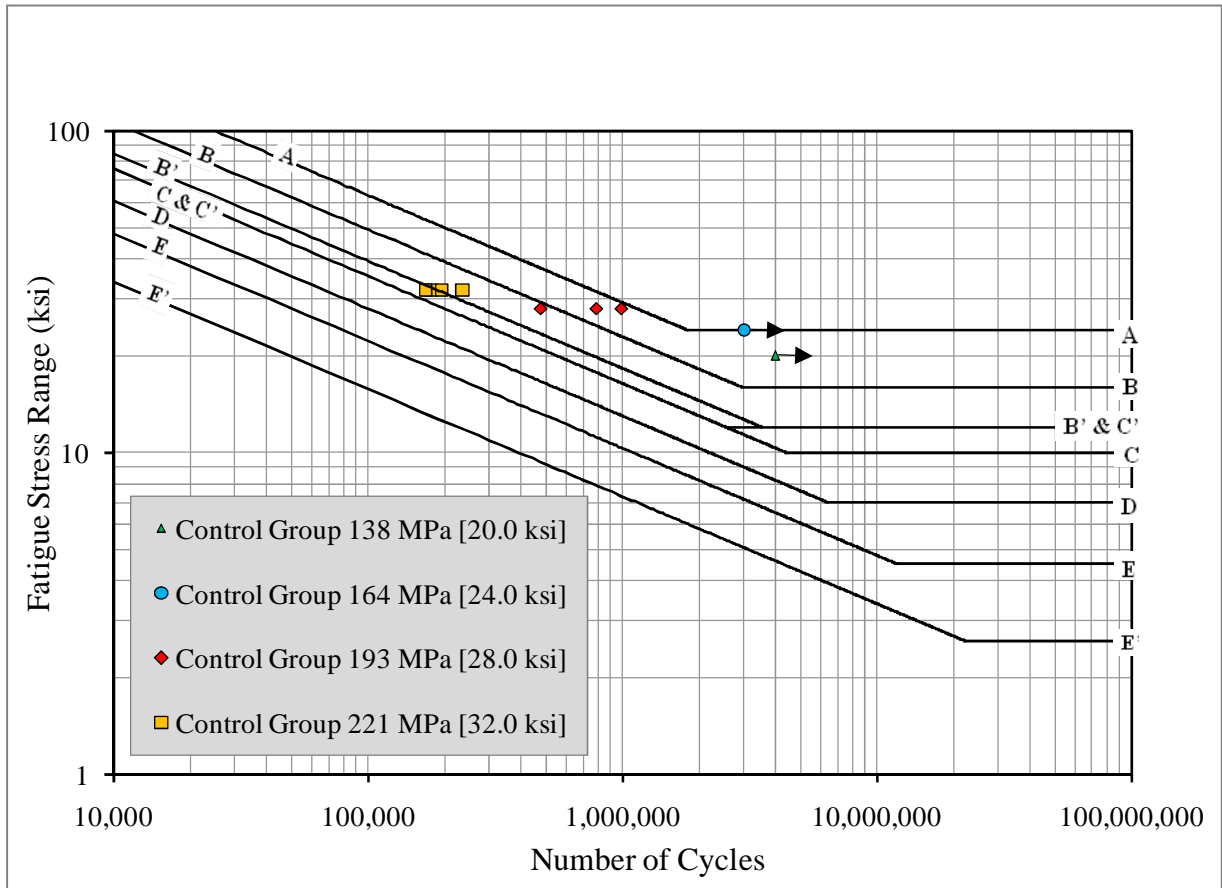


Figure 4-1: Results of preliminary investigated stress ranges for 3.18 mm [0.125 in.] thick fatigue specimens plotted on AASHTO Design stress range curves for Categories A to E' (All details Category B)

Test ID	Target Stress [Mpa (ksi)]			Applied Load [kN (kip)]			Specimen Dimensions [mm (in.)]						Frequency [Hz]	Cycles to Failure
	Range	Minimum	Maximum	Range	Minimum	Maximum	Width	Thickness	Hole Diameter	Stress Ratio	Stress Ratio			
Controlo_9	220.6 (32.0)	13.8 (2.0)	234.4 (34.0)	20.36 (4.577)	1.272 (0.286)	21.63 (4.863)	32.23 (1.2688)	3.18 (0.1251)	3.18 (0.1250)	0.0588	0.0588	2	234,824	
Controlo_10	220.6 (32.0)	13.8 (2.0)	234.4 (34.0)	20.34 (4.572)	1.271 (0.286)	21.61 (4.858)	32.04 (1.2614)	3.19 (0.1257)	3.18 (0.1250)	0.0588	0.0588	2	177,106	
Controlo_11	220.6 (32.0)	13.8 (2.0)	234.4 (34.0)	20.50 (4.609)	1.281 (0.288)	21.78 (4.897)	32.22 (1.2614)	3.20 (0.1259)	3.15 (0.1239)	0.0588	0.0588	2	169,222	
Controlo_12	220.6 (32.0)	13.8 (2.0)	234.4 (34.0)	19.93 (4.481)	1.246 (0.280)	21.18 (4.761)	31.89 (1.2557)	3.14 (0.1238)	3.16 (0.1246)	0.0588	0.0588	2	195,220	
Controlo_13	220.6 (32.0)	13.8 (2.0)	234.4 (34.0)	19.77 (4.445)	1.236 (0.278)	21.01 (4.723)	31.92 (1.2567)	3.11 (0.1226)	3.14 (0.1236)	0.0588	0.0588	2	194,449	
Controlo_14	193.1 (28.0)	13.8 (2.0)	206.8 (30.0)	17.49 (3.932)	1.249 (0.281)	18.74 (4.213)	32.11 (1.2642)	3.12 (0.1230)	3.11 (0.1225)	0.0667	0.0667	2	479,117	
Controlo_15	137.9 (20.0)	13.8 (2.0)	151.7 (22.0)	12.36 (2.778)	1.236 (0.278)	13.6 (3.056)	31.79 (1.2517)	3.13 (0.1231)	3.12 (0.1227)	0.0909	0.0909	4	Infinite Life (>4,000,000)	
Controlo_16	164.5 (24.0)	13.8 (2.0)	179.3 (26.0)	14.94 (3.359)	1.245 (0.280)	16.18 (3.638)	31.91 (1.2562)	3.14 (0.1236)	3.14 (0.1235)	0.0769	0.0769	4	Infinite Life (>3,000,000)	

Table 4-1: Results and dimensions of preliminary investigation for test stress ranges of 3.18 mm [0.125 in.] thick fatigue specimens

4.1.2 Fatigue Life of Pick Treated Specimens

The goal of this test program was only to determine the fatigue life of the PICK treated specimens. A separate detailed report of the PICK tool procedure and components will be prepared and discussed at a later date. This report will be completed by a member the Fatigue and Fracture research group at the University of Kansas. The fatigue results of the PICK treated specimens, tested at a stress range of 221 MPa [32.0 ksi], compared to the fatigue specimens tested at 221 MPa [32.0 ksi] are shown in Figure 4-2 and Table 4-2.

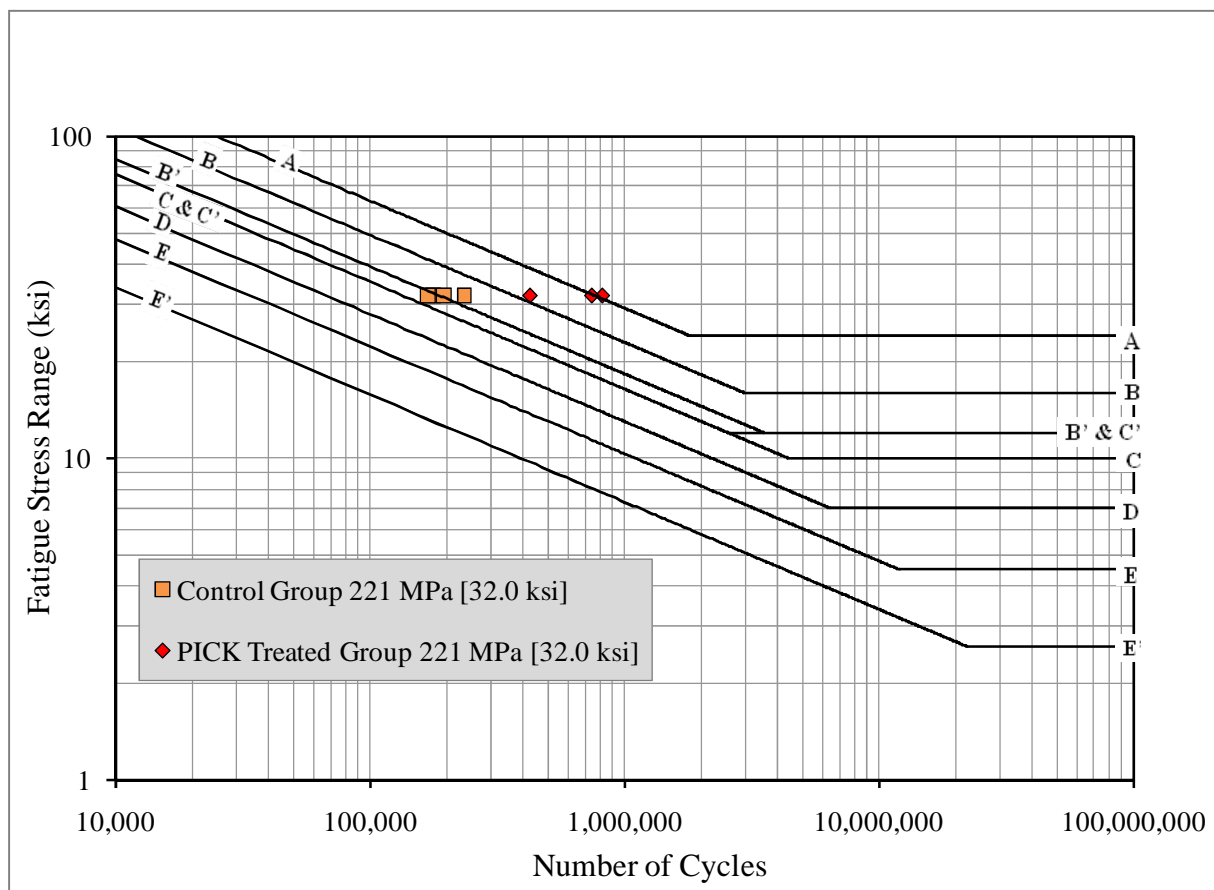


Figure 4-2: Comparison of results from control specimens and PICK treated specimens for 3.18 mm [0.125 in.] thick fatigue specimens plotted on AASHTO Design stress range curves for Categories A to E'

Test ID	Target Stress [MPa (ksi)]			Applied Load [kN (kip)]			Specimen Dimensions [mm (in.)]						Frequency [Hz]	Cycles to Failure
	Range	Minimum	Maximum	Range	Minimum	Maximum	Width	Thickness	Hole Diameter	Stress Ratio	Stress Ratio			
Control_9	220.6 (32.0)	13.8 (2.0)	234.4 (34.0)	20.36 (4.577)	1.272 (0.286)	21.63 (4.863)	32.23 (1.2688)	3.18 (0.1251)	3.18 (0.1250)	0.0588	0.0588	2	234,824	
Control_10	220.6 (32.0)	13.8 (2.0)	234.4 (34.0)	20.34 (4.572)	1.271 (0.286)	21.61 (4.858)	32.04 (1.2614)	3.19 (0.1257)	3.18 (0.1250)	0.0588	0.0588	2	177,106	
Control_11	220.6 (32.0)	13.8 (2.0)	234.4 (34.0)	20.50 (4.609)	1.281 (0.288)	21.78 (4.897)	32.22 (1.2614)	3.20 (0.1259)	3.15 (0.1239)	0.0588	0.0588	2	169,222	
Control_12	220.6 (32.0)	13.8 (2.0)	234.4 (34.0)	19.93 (4.481)	1.246 (0.280)	21.18 (4.761)	31.89 (1.2557)	3.14 (0.1238)	3.16 (0.1246)	0.0588	0.0588	2	195,220	
Control_13	220.6 (32.0)	13.8 (2.0)	234.4 (34.0)	19.77 (4.445)	1.236 (0.278)	21.01 (4.723)	31.92 (1.2567)	3.11 (0.1226)	3.14 (0.1236)	0.0588	0.0588	2	194,449	
PICK 3	220.6 (32.0)	13.8 (2.0)	234.4 (34.0)	20.17 (4.535)	1.259 (0.283)	21.43 (4.818)	32.09 (1.2633)	3.16 (0.1245)	3.12 (0.1250)	0.0588	0.0588	2	818,635	
PICK 4	220.6 (32.0)	13.8 (2.0)	234.4 (34.0)	19.83 (4.459)	1.241 (0.279)	21.07 (4.737)	32.00 (1.2597)	3.12 (0.1228)	3.12 (0.1250)	0.0588	0.0588	2	743,725	
PICK 6	220.6 (32.0)	13.8 (2.0)	234.4 (34.0)	20.08 (4.514)	1.254 (0.282)	21.33 (4.796)	32.11 (1.2641)	3.15 (0.1239)	3.12 (0.1250)	0.0588	0.0588	2	426,302	

Table 4-2: Results and dimensions of control and PICK treated specimens for 3.18 mm [0.125 in.] thick fatigue specimens

The results shown in Figure 4-2 illustrate that treatment with the PICK tool enhanced fatigue life of untreated specimens. Treated specimens, PICK 3 and PICK 4, each had a fatigue life improvement of approximately four times that of the untreated specimens. PICK 6 displayed a slightly smaller fatigue life improvement of only around two times that of untreated specimens. However, during treatment of PICK 6, the piezoelectric crystals on the PICK tool cracked and the ultrasonic impact treatment was stopped. It was hypothesized that the lack of full ultrasonic treatment could have caused the lower levels of fatigue life improvement for specimen PICK 6.

4.1.3 Bending Stress

Bending stress was recorded and monitored twice a day for each of the 3.18 mm [0.125 in.] thick fatigue specimens. Bending stress levels were kept to as close to or below 5 percent of the maximum applied stress. The modulus of elasticity, 207,031 MPa [30,028 ksi], used to calculate levels of bending from Eq. (3-1), was determined from the 3.18 mm [0.125 in.] thick tension specimen results, Section 4.2.3. Table 4-3 contains a complete set of all 3.18 mm [0.125 in.] fatigue specimens and their corresponding bending stress.

Specimen	Test Frequency (Hz)	Stress Range [MPa (ksi)]	Max Stress [MPa (ksi)]	No. Cycles To Initiation	Allowable Bending Stress [MPa (ksi)] (5 Percent of Max Stress)	Average Bending Stress [MPa (ksi)]
Control_9	2	220.6 (32.0)	234.4 (34.0)	234,824	11.7 (1.70)	19.8 (2.88)
Control_10	2	220.6 (32.0)	234.4 (34.0)	177,106	11.7 (1.70)	13.0 (1.88)
Control_11	2	220.6 (32.0)	234.4 (34.0)	169,222	11.7 (1.70)	25.8 (3.74)
Control_12	2	220.6 (32.0)	234.4 (34.0)	195,220	11.7 (1.70)	11.1 (1.61)
Control_13	3	220.6 (32.0)	234.4 (34.0)	194,449	11.7 (1.70)	7.65 (1.11)
Control_14	2	193.1 (28.0)	206.8 (30.0)	479,117	10.3 (1.50)	3.65 (0.53)
Control_15	4	137.9 (20.0)	151.7 (22.0)	Infinite Life (>4,000,000)	7.58 (1.10)	3.45 (0.50)
Control_16	4	164.5 (24.0)	179.3 (26.0)	Infinite Life (>3,000,000)	8.96 (1.30)	4.96 (0.72)
PICK 3	2	220.6 (32.0)	234.4 (34.0)	818,635	11.7 (1.70)	10.3 (1.50)
PICK 4	2	220.6 (32.0)	234.4 (34.0)	743,725	11.7 (1.70)	7.58 (1.10)
PICK 6	2	220.6 (32.0)	234.4 (34.0)	426,302	11.7 (1.70)	10.3 (1.50)

Table 4-3: Bending stress summary for 3.18 mm [0.125 in.] thick fatigue specimens

4.2 TENSILE TESTING

In total, 10 tension specimens were failed for this test program. Five specimens with a 3.18 mm [0.125 in.] thickness and five with a 6.35 mm [0.250 in.] thickness were tested. Detailed dimensions of the tension specimens are discussed in Section 3.5. Of the five 3.18 mm [0.125 in.] thick specimens, one set of data had to be discarded due to excessive slip in the grips of the Baldwin test frame. All of the 6.35 mm [0.250 in.] were successfully tested. A summary of the yield strength, modulus of elasticity and ultimate tensile strength are shown in Table 4-4 and Table 4-5.

Specimen	Modulus of Elasticity		Yield Strength		Tensile Strength	
	ksi	MPa	ksi	MPa	ksi	MPa
0.125_AT1	30,595	210,943	48.9	337.2	55.2	380.6
0.125_AT3	30,314	209,006	44.8	308.9	55.8	384.7
0.125_AT4	30,118	207,655	46.1	317.8	55.0	379.2
0.125_AT5	29,083	200,519	45.3	312.3	55.4	382.0
Average	30,028	207,031	46.3	319.1	55.4	381.6

Table 4-4: Summary of results for 3.18 mm [0.125 in.] tension specimens

Specimen	Modulus of Elasticity		Yield Strength		Tensile Strength	
	ksi	MPa	ksi	MPa	ksi	MPa
0.25_AT1	28,348	195,449	48.0	330.9	71.6	493.7
0.25_AT2	29,285	201,910	48.2	332.3	71.6	493.9
0.25_AT3	29,293	201,965	49.0	337.8	72.2	497.7
0.25_AT4	28,353	195,484	48.9	337.2	71.7	494.0
0.25_AT5	28,571	196,990	48.8	336.5	72.0	496.6
Average	28,770	198,359	48.6	334.9	72.0	495.0

Table 4-5: Summary of results for 6.35 mm [0.250 in.] tension specimens

4.2.1 Yield Strength

In accordance with section 7.7.3 of ASTM specification E8, the autographic diagram method was used to determine values of yield strength. The autographic method defines yield strength as the stress corresponding to the maximum force at the onset of discontinuous yielding. Figure 4-3 shows the process by which the autographic method was used to calculate yield strength for each tension specimen. The autographic method was chosen over the offset method because of the discontinuous yielding displayed in the results of the tension tests. A detailed discussion regarding the differences between the autographic and offset method can be found in Vilhauer, B. [29]. The average yield strengths for the 3.18 mm [0.125 in.] and 6.35 mm [0.250 in] tension specimens were 319.1 MPa [46.3 ksi] and 334.9 MPa [48.6 ksi] respectively. This meant the average yield strength for both plate thicknesses was greater than the minimum yield strength of 248 MPa [36.0 ksi] required for Gr. A36 steel. A complete set of partial stress-strain diagrams, illustrating the autographic diagram method, for each tensile specimen can be found in Appendix B of this report.

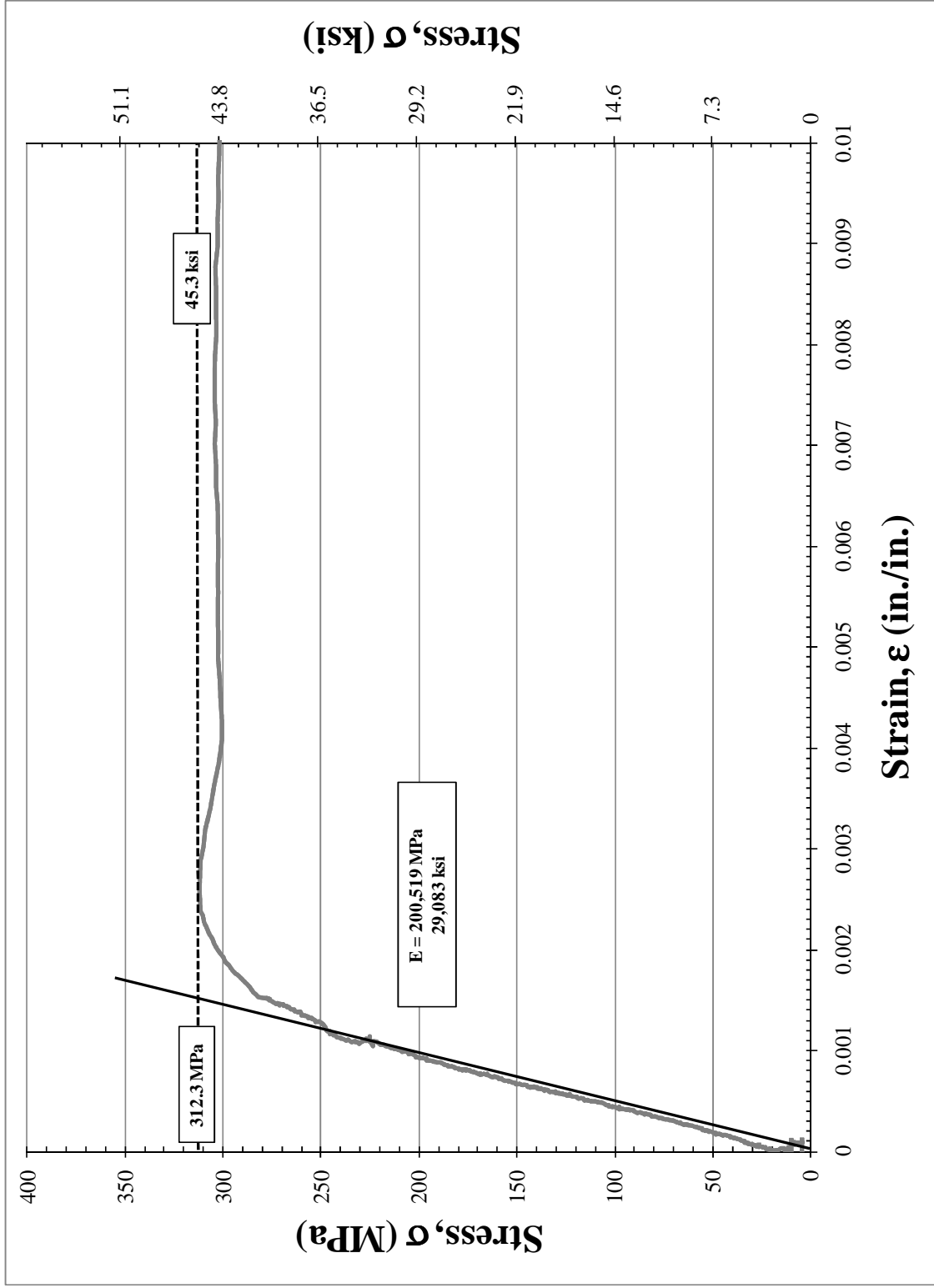


Figure 4-3: Stress-Strain plot used to determine yield strength for specimen 0.125_AT5

4.2.2 Ultimate Tensile Strength

In accordance with section 7.10 of ASTM specification E8, ultimate tensile strength was found by dividing the maximum force measured by the load cell by the initial cross sectional area of the tensile specimen. As shown in Figure 4-4, the ultimate tensile strength could also be found by taking the apex of the complete stress-strain curves. The average tensile strength for the 3.18 mm [0.125 in.] plate was equal to 381.6 MPa [55.4 ksi]. While this value of ultimate tensile strength was lower than the minimum tensile strength 400 MPa [58.0 ksi] required for Gr. A36 steel, for the purposes of this study, the lower value of ultimate tensile strength was not of any concern. The average ultimate tensile strength for the 6.35 mm [0.250 in.] plate was equal to 495 MPa [72.0 ksi]. This value far exceeded the minimum tensile strength required for Gr. A36 steel. Complete stress-strain diagrams for all tension tests, used to determine ultimate tensile strength, can be found in APPENDIX B of this report.

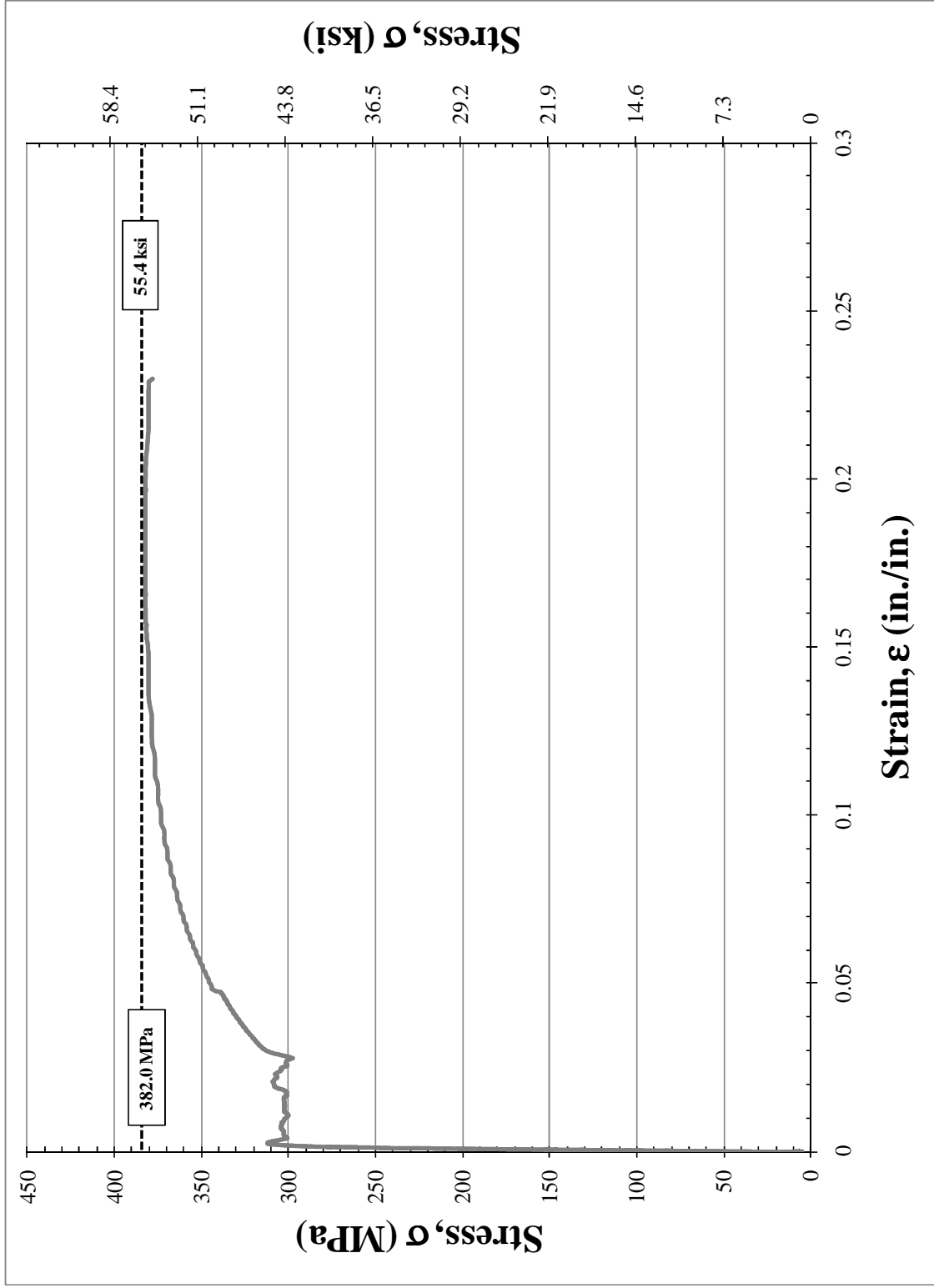


Figure 4-4: Stress-Strain plot used to determine ultimate tensile strength for specimen 0.125_AT5

4.2.3 Modulus of Elasticity

The modulus of elasticity of each specimen was determined from the linear region of the stress-strain diagrams. As mentioned in Section 3.5, readings from strain gages, applied to both sides of the tension specimens, were used to determine modulus of elasticity. Once data from the strain gage readings had been input into Microsoft Excel, the linear regression feature was used to determine the corresponding modulus of elasticity. The average value for slope of the two sets of strain gage data was taken as the modulus of elasticity of the specimen. Figure 4-5 illustrates the process by which modulus of elasticity was determined from readings of the two strain gages. The average moduli for the 3.18 mm [0.125 in.] and 6.35 mm [0.250 in] tension specimens were 207,031 MPa [30,028 ksi] and 198,359 MPa [28,770 ksi] respectively. The average modulus of elasticity for both plate thicknesses were close to the expected Modulus of Elasticity of steel, 200,000 MPa (29,000 ksi). Patial stress-strain plots, similar to Figure 4-5, are shown for all specimens in APPENDIX B.

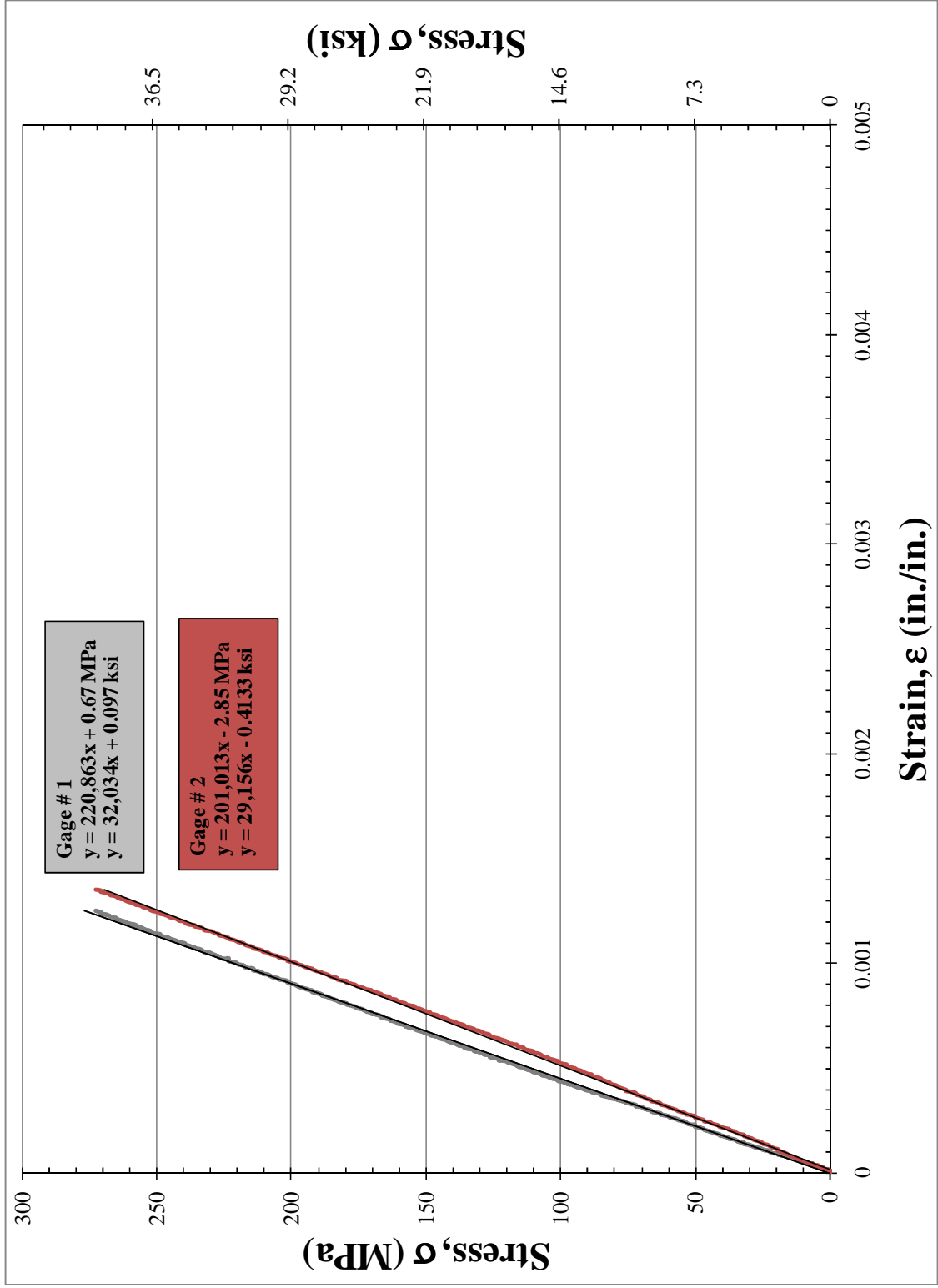


Figure 4-5: Strain gage readings used to quantify modulus of elasticity for specimen 0.125_AT1

CHAPTER 5 FINITE ELEMENT ANALYSIS

The finite element analysis (FEA) portion of this report included five groups of finite element models (FEMs). The purpose of these FEMs was to extend concepts of current static cold expansion techniques, commonly used on aerospace materials (primarily aluminum), to materials frequently used in bridge construction (in this case steel). The goal of the first group of FEMs was to verify that beneficial residual compressive stresses could be induced in mild grade steel. This group of FEMs will be referred to as the “2D uniform expansion (UE) models.” The plate dimensions used for the 2D UE models were the same as the 3.18 mm [0.125 in.] thick fatigue specimens discussed in Section 3.1.1.1. The second set of models expanded upon the 2D UE models by including the fatigue specimens’ thickness. The final three sets of FEMs investigated the affects of varying geometric parameters, shown to influence levels of beneficial residual stress in aerospace materials, on residual stress levels in mild steel. The parameters investigated were edge distance ratio, hole diameter, and plate thickness. These models will be referred to as “edge distance models,” “hole diameter models” and “plate thickness models” respectively.

5.1 MODEL PARAMETERS

All FEMs were created in ABAQUS/CEA software Version 6.8.2.and solved for in ABAQUS/Standard software. The five groups of models were generated to provide numeric solutions to the goals listed above. The following sections provide a detailed overview of the model parameters specific to each group.

5.1.1 2D and 3D Uniform Expansion Model Parameters

A significant body of literature exists in which numerical simulation studies were performed with the intent of comparing uniform levels of expansion with existing cold expansion

techniques [5-10, 18, 20-23]. The majority of these studies compared the results from uniform expansion to a simulated process of split sleeve mandrel cold expansion in aluminum plates. Results of uniform expansion models were compared to the split sleeve mandrel technique because it is the most effective and widely accepted technique intended for aerospace applications [6]. For this project, a similar analytical approach will be taken to compare uniform expansion (UE) of mild steel with expansion generated using the PICK tool technique. The following section is an overview of the UE models, the results of which will later be compared to those of FEMs simulating the PICK tool technique.

The aluminum alloy modeled in this study was 2024-T3 Alclad. The material properties were referenced from a FEA investigation performed by de Matos, P.F.P. et al. [22]. The mild steel alloy used in this study was a Gr. A36 steel. True-stress true-strain material properties for the Gr. A36 steel, used in all FEMs simulations, came from tensile tests performed as part of this study, described in Section 4.2. True-stress true-strain properties have been presented in APPENDIX B of this report.

Basic material properties used for the FEMs are shown in Table 5-1. Hardening behavior, shown in Figure 5-1 and Figure 5-2, was modeled using data from experimental tensile testing (mild steel) and properties found in past literature (aluminum). In addition, hardening behavior for both the aluminum and mild steel materials was defined as isotropic. The assumption of isotropic hardening was consistent with model parameters in the analytical investigation performed by de Matos et. al. [22]. While isotropic hardening behavior was assumed for all FEMs in this investigation, extensive research has shown beneficial residual stresses to be slightly lower when assuming kinematic hardening behavior in place of isotropic [17, 20-21]. Since modeling cold expansion in mild steel was at a preliminary stage, isotropic

hardening was considered an appropriate assumption since modeling with isotropic hardening is simpler and more expedient. The hardening behavior of mild-steel, as shown in Figure 5-2, was used in all subsequent FEMs comprised of this material.

Material	Modulus of Elasticity		Yield Strength		Tensile Strength		Poisson's Ratio
	ksi	MPa	ksi	MPa	ksi	MPa	
2024-T3 Alclad Aluminum	11,200	77,220	45.2	312	63.8	440	0.35
Gr. A36 Steel	30,028	207,301	46.3	319	67.2	463	0.30

Table 5-1: Basic material properties used in FEM

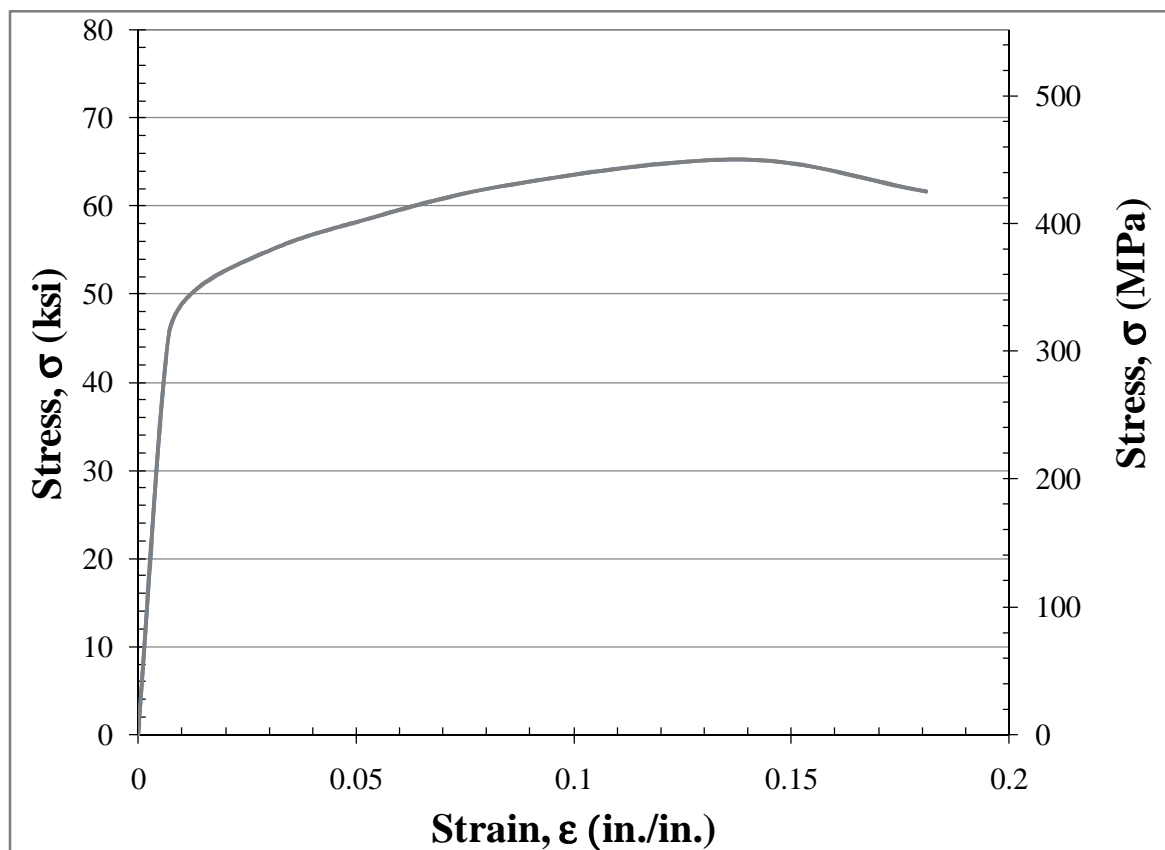


Figure 5-1: Stress-strain plot for for 2024-T3 Alclad Aluminum, de Matos et. al. [22]

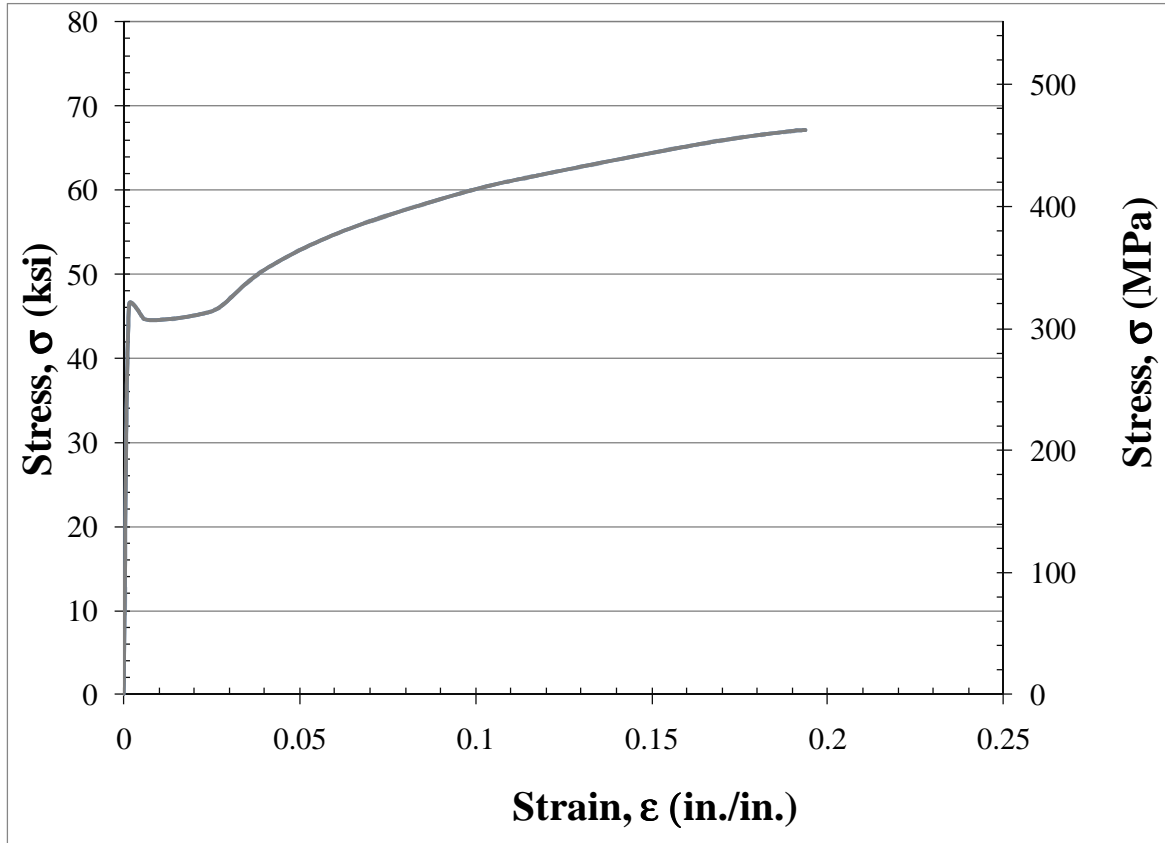


Figure 5-2: Stress-strain plot for Gr. A36 Steel, Section 4.2

The first set of UE models constructed were 2D and included 2024-T3 Alclad Aluminum material properties and hardening behavior. The models were created with the same outside plate dimensions as the 3.18 mm [0.125 in.] fatigue specimens, as presented in Section 3.1.1.1. The 2D UE aluminum models were developed first so that modeling parameters, such as mesh size and type, could be adjusted until results closely matched those of previously accepted FEM investigations [22] that were performed for 2024-T3 Alclad Aluminum. Therefore, the 2D UE Models were primarily intended to validate modeling techniques being employed in this study.

To generate uniform expansion in the 2D aluminum models, a radial displacement was applied to the edge of the hole, expanding the material past the point of yielding. To generate a radial displacement, a cylindrical coordinate system was first created in ABAQUS. An “expansion” step was then created which included a displacement/rotation boundary condition. The boundary condition used the cylindrical coordinate system to generate the appropriate outward displacement in the radial direction. A second step, called the “relaxation” step, was then created to inactivate the boundary condition that generated uniform expansion in the radial direction. Upon the relaxation of this UE, beneficial residual stresses were generated in each of the three principal axes. The UE for all sets of FEMs was defined as:

$$i = \frac{D_o - D}{D} \times 100\% \quad (5-1)$$

where D_o is the initial diameter of the hole and D is the expanded hole diameter. UE levels of $i = 3\%$, 4% , 5% and 6% were investigated for all uniform expansion FEMs. These levels of expansion were chosen to capture the range of “optimum levels” of expansion shown to maximize fatigue life improvement for current cold expansion techniques [8, 22, 27].

Many of the parameters of the 2D aluminum models were consistent with the analytical study performed by de Matos, P.F.P. et. al. [22]. The similarities included the following general assumptions: (1) non-linear geometric effects at the expansion and relaxation steps (2) a direct method of solution defined in the equation solver and (3) as mentioned previously, isotropic hardening behavior of all materials past the point of yielding. The main differences in the analysis performed de Matos, P.F.P. et. al. [22] and this investigation were the outside plate dimensions and the mesh configuration surrounding the UE hole.

Once material properties had been properly defined, the next step in the modeling procedure was to generate an appropriate mesh configuration for the aluminum 2D UE model. The default element shape, hexahedral elements, was used for the aluminum 2D UE models and later used for all FEMs of this analytical study. The hexahedral elements provided efficient and symmetric mesh configurations which allowed for paths to be easily cut through models during data extraction. Fine mesh sizes (small elements) were used at areas of high stress concentrations, in this case, the areas directly around the edges of the hole, and the mesh was gradually made coarser (larger elements) moving farther away from the hole. A parametric study was performed to determine optimum mesh size, or the size in which no further reduction in mesh size would significantly affect levels of residual stress. Three mesh sizes were investigated for the region directly surrounding the hole; these mesh sizes included 0.254 mm [0.010 in.], 0.127 mm [0.005 in.], and 0.0635 mm [0.0025 in.]. Results from this parametric study are shown in Figure 5-3.

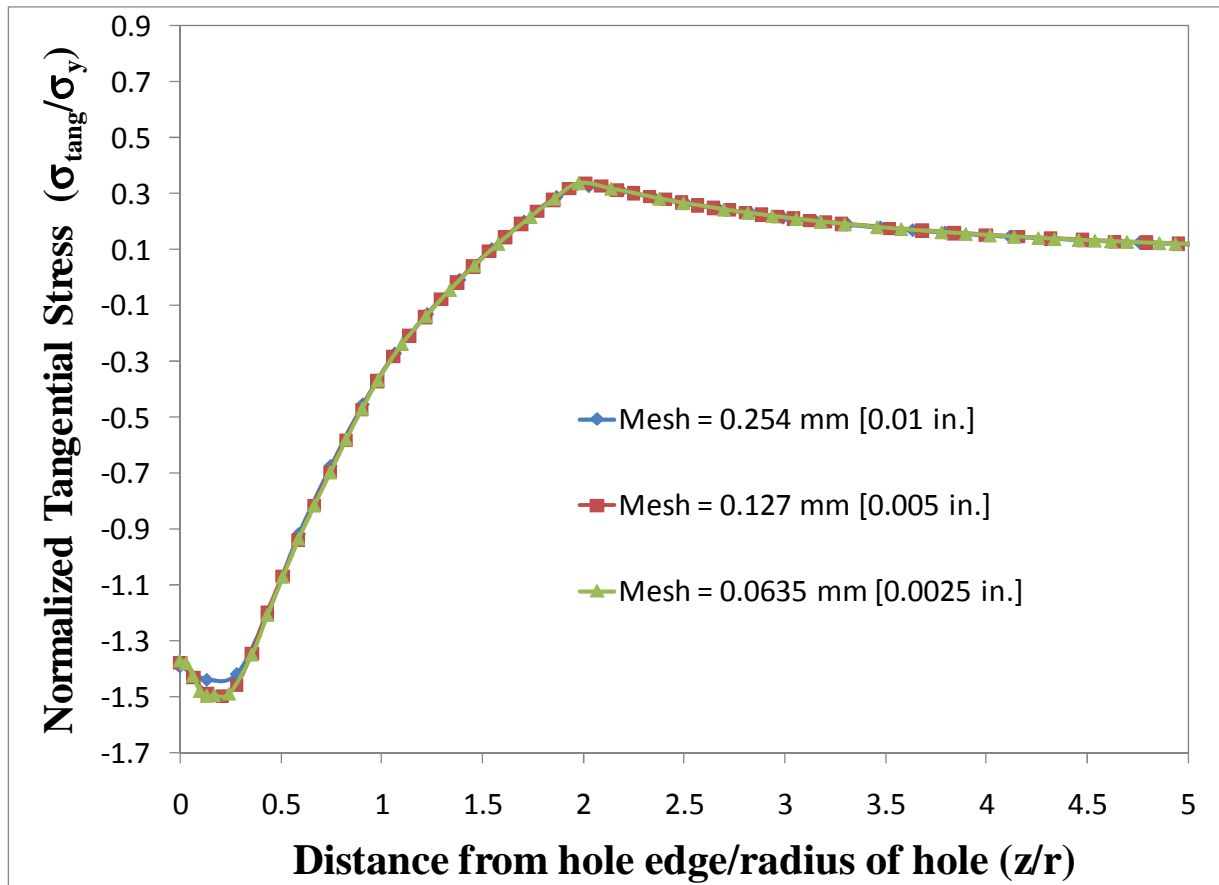


Figure 5-3: Resulting tangential stress (at 8 percent UE) field from parametric study determining optimum mesh size directly surround hole in 2D aluminum uniform expansion FEM

As illustrated in Figure 5-3, all investigated mesh sizes (0.254 mm [0.01 in.], 0.127 mm [0.005 in.] and 0.0635 mm [0.0025 in.]) resulted in similar residual tangential stress fields. The only difference was the 0.254 mm [0.01 in.] mesh size had a slightly lower peak compressive stress. The 0.0635 mm [0.0025 in.] mesh size converged almost exactly with the mesh size of 0.127 mm [0.005 in.]. To decrease model runtime without sacrificing accuracy of results, a mesh size of 0.127 mm [0.005 in.] was used for the area surrounding the hole of all the 2D aluminum UE models. The same mesh size was used for the 2D mild steel UE models.

To develop a coarser mesh moving away from the hole where numerical accuracy was not as critical, the model was partitioned into smaller sections. The 2D aluminum UE model partition configuration, shown in Figure 5-4, was developed so that fine mesh sizes existed around the UE hole. The final mesh configuration, shown in Figure 5-5, used for the 2D aluminum UE models, was also used for the 2D mild steel UE models.

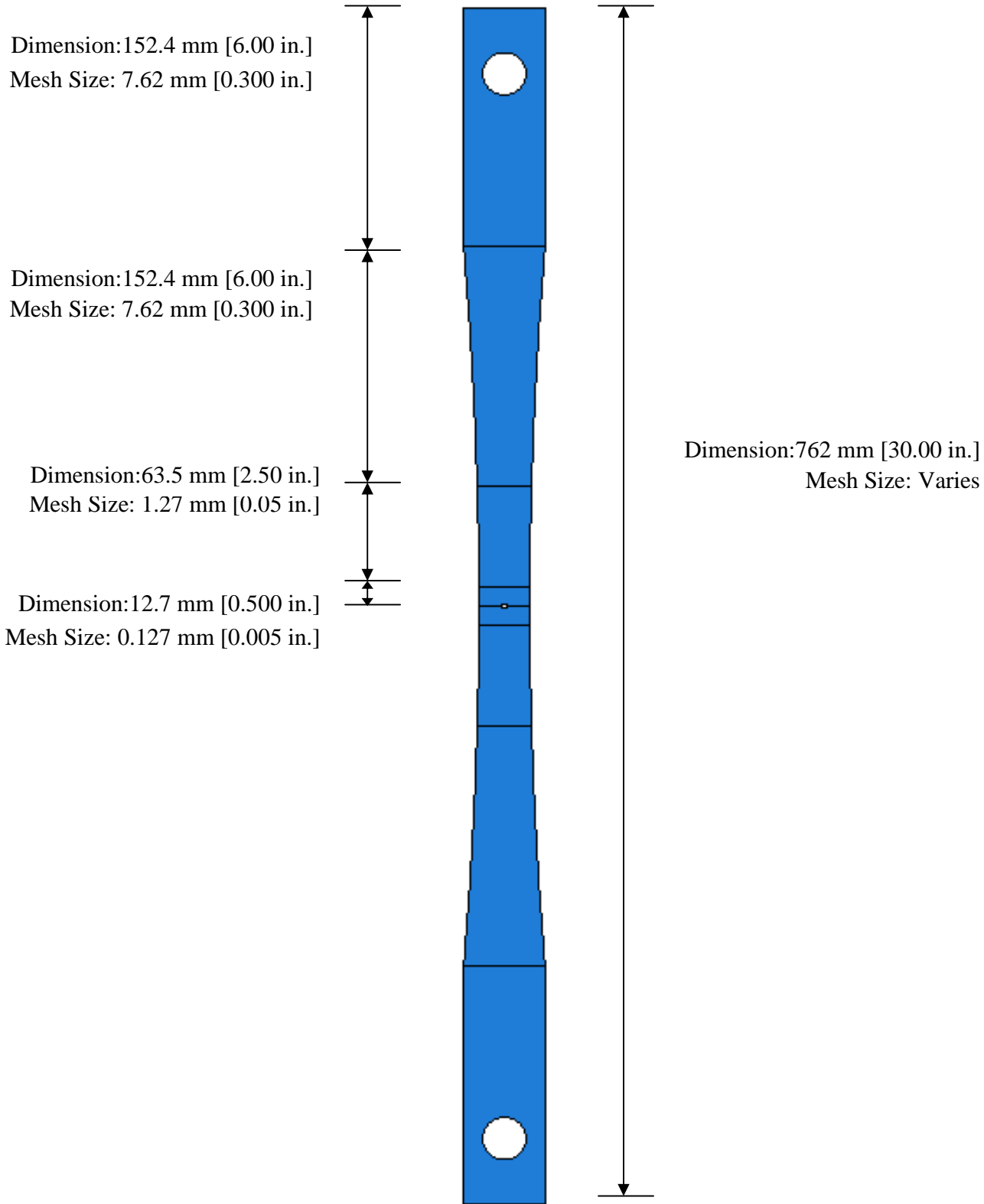


Figure 5-4: Partitioned 2D aluminum UE model, including partition dimensions and mesh size (symmetric)

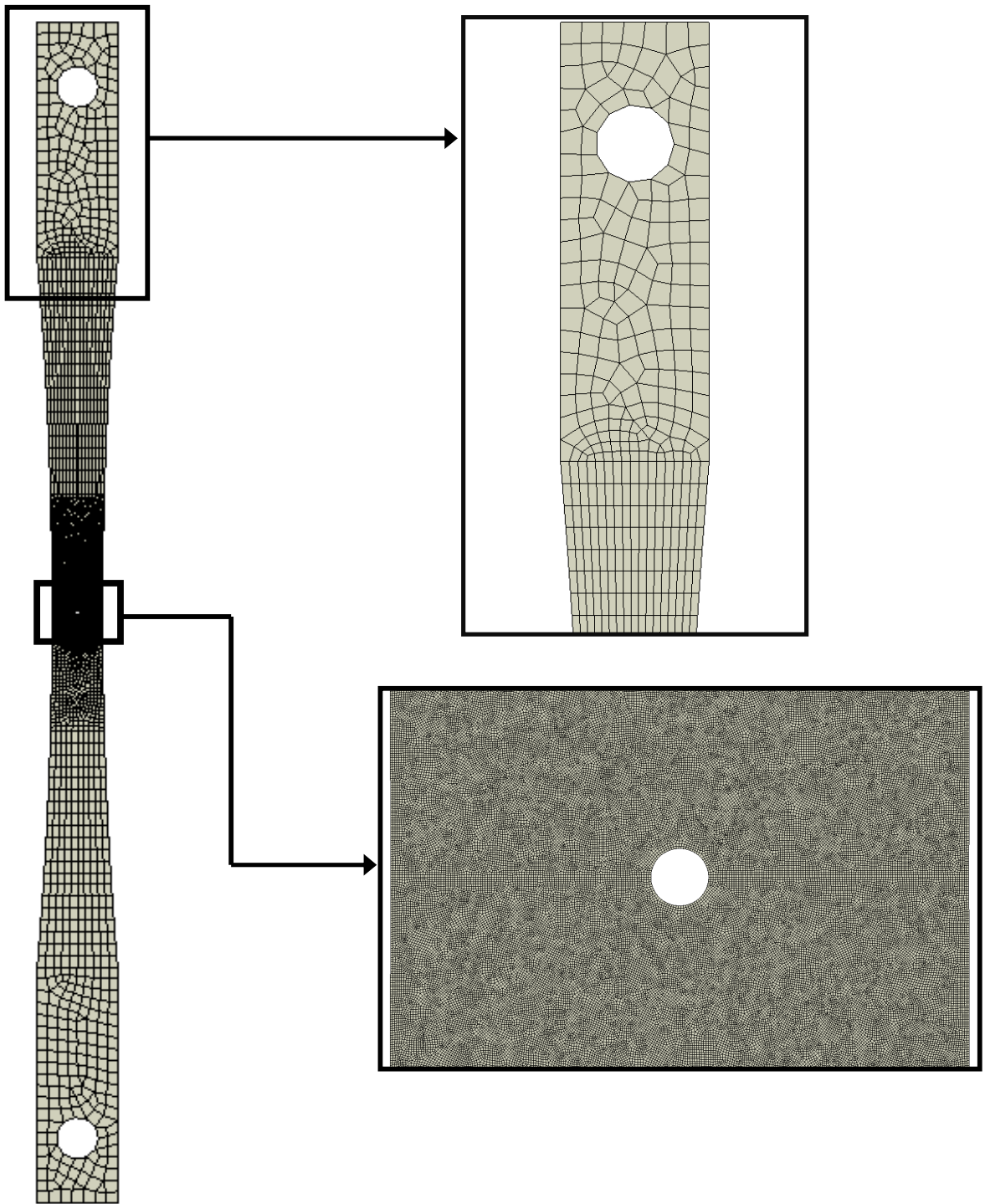


Figure 5-5 Final mesh configuration of aluminum and steel 2D UE models, mesh size 0.127 mm [0.005 in.]

Once the results of the 2D aluminum UE models were validated through comparison with previous investigations and general behavior was confirmed for Gr. A36 steel in the 2D models, the next step was to create a set of 3D models analyzing the change in residual stress through the thickness of the fatigue specimens under UE. The same levels of expansion were used in the 3D models as simulated in the 2D models. The 3D models were constructed with the same outside dimensions and thickness as the 3.18 mm [0.125 in.] thick mild steel fatigue specimens, described in Section 3.1.1.1. The 3D UE models included the 26.99 mm [1.063 in.] diameter steel pins at the ends of the specimens, similar to the loading configuration of the MTS Load Frame Section 3.2.4.1. The pins, which were modeled with typical steel to steel contact surfaces, were included so that future investigations could look at the effects of loading the specimen.

The 3D mild steel UE models were created under many of the same assumptions used in the 2D aluminum and mild steel UE models. In fact, all assumptions for material properties, hardening behavior, mesh type, and solution technique were identical for the 3D mild steel UE models as for the 2D aluminum and mild steel UE models.

The difference in the 3D UE models versus the 2D UE models was in the mesh *size* used for the area surrounding the hole. Similar to the 2D UE models, a parametric study was performed to optimize mesh size of the regions of high stress concentration directly surrounding the UE hole. As shown in Figure 5-6, reduction of mesh size in the regions surrounding the UE hole did not have a significant effect on levels of tangential residual compressive stress. Due to minute effects of changing mesh size, a mesh size of 0.2032 mm [0.008 in.] was used for all 3D uniform expansion models, compared to a 0.127 mm [0.005 in.] mesh used for all 2D UE models.

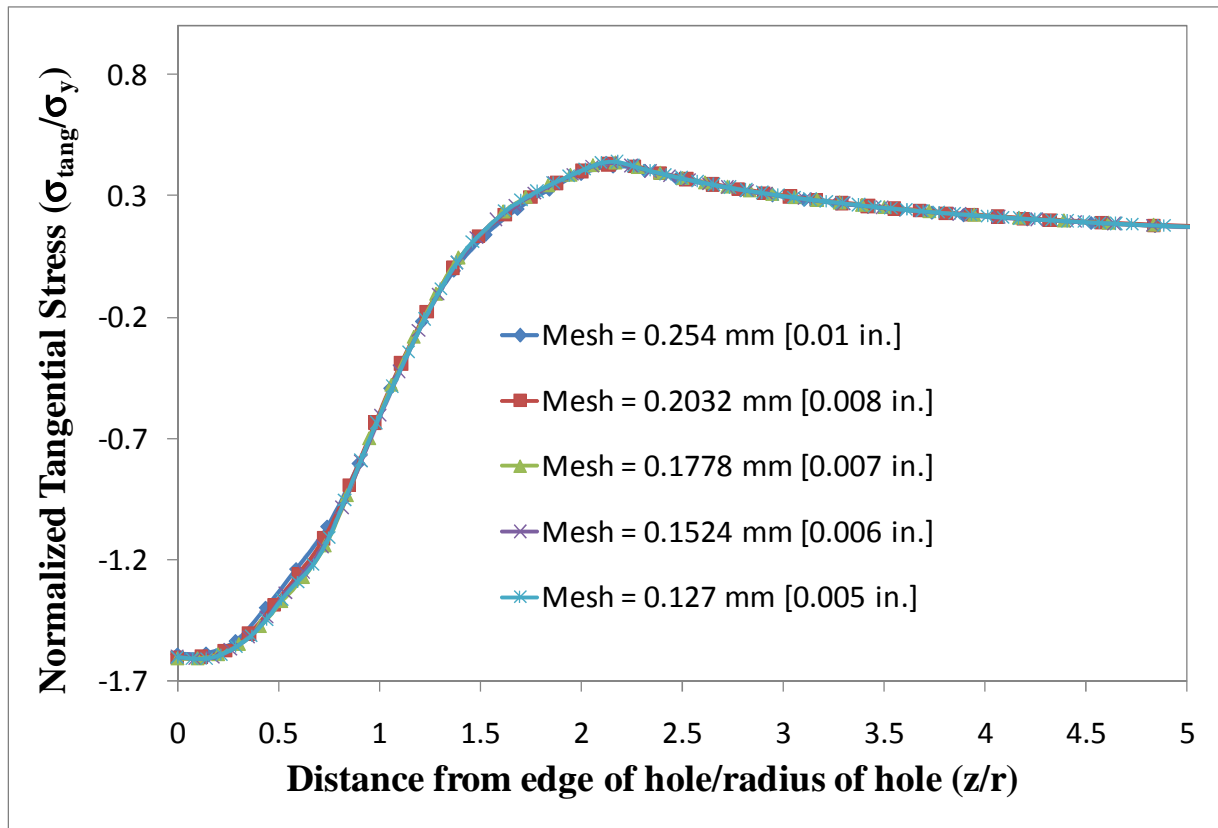


Figure 5-6: Tangential stress field (at mid-thickness and 6 percent UE) from parametric study determining optimum mesh size directly surround hole in 3D mild steel UE FEM

The final parameter investigated in creating the 3D mild steel UE models was whether a circular partition (Figure 5-9 and Figure 5-10) surrounding the hole, as assumed in many past FEAs, rather than the rectangular partition (Figure 5-7 and Figure 5-8) assumed in this investigation, would affect levels of tangential residual stress. To determine whether partition geometry had an effect on levels of residual stress, a separate partitioning scheme, shown in Figure 5-9, was created using a circular partition surrounding the cold expanded hole. Results from the two partitioning schemes are shown in Figure 5-11. As shown in Figure 5-11, partitioning geometry had little to no effect on tangential residual stress, therefore the original partitioning scheme, shown in Figure 5-7, used for the parametric study optimizing mesh size, was selected.

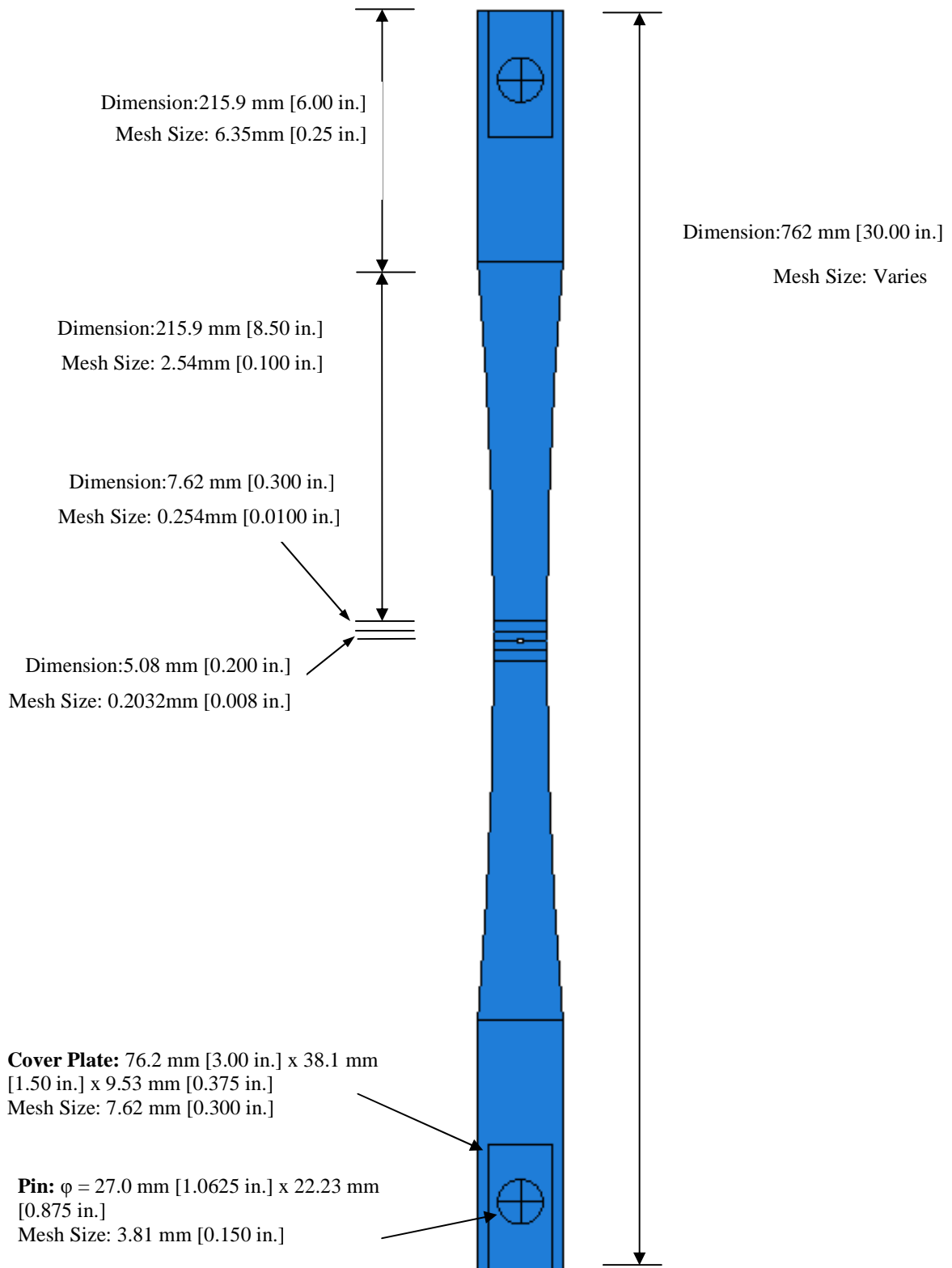


Figure 5-7: Partitioned 3D mild steel UE model with rectangular partition surrounding UE hole, including

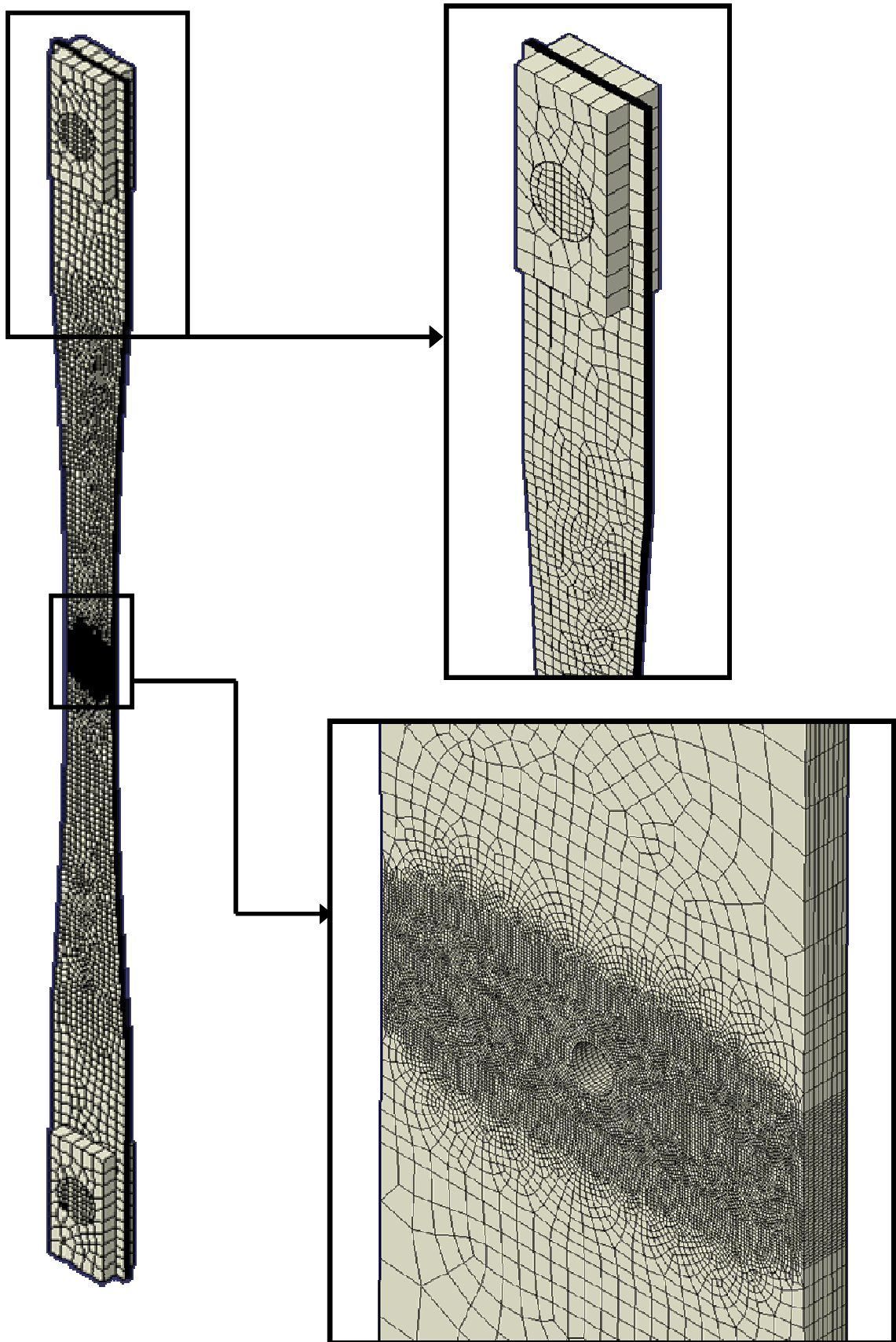


Figure 5-8 Final meshed 3D mild steel UE model, close up at mid-thickness and at cover plate

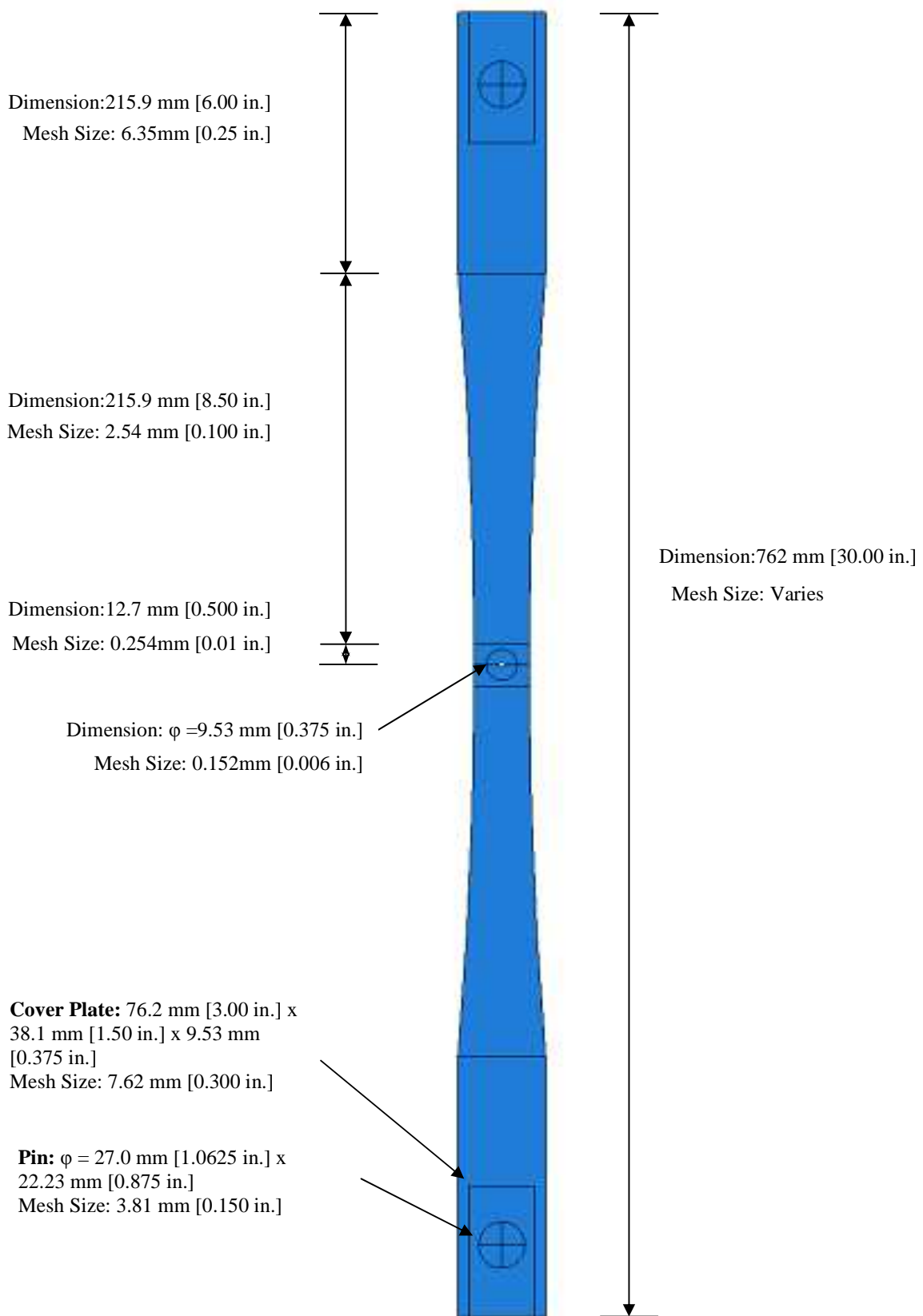


Figure 5-9: Partitioned 3D mild steel UE model with circular partition surrounding UE hole, including

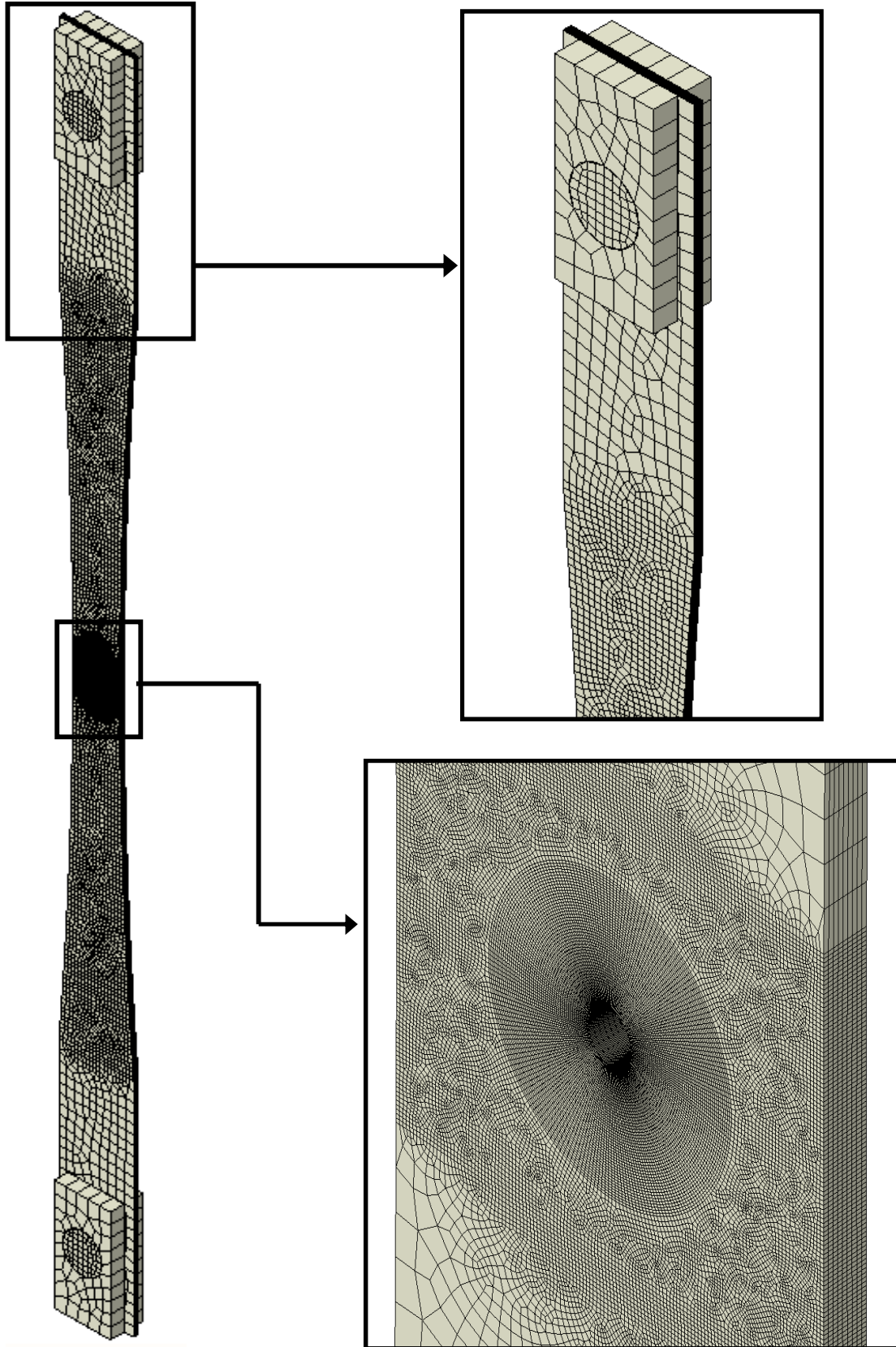


Figure 5-10 Final meshed 3D UE model with circular partition surround UE hole, close up at mid-thickness and at cover plate

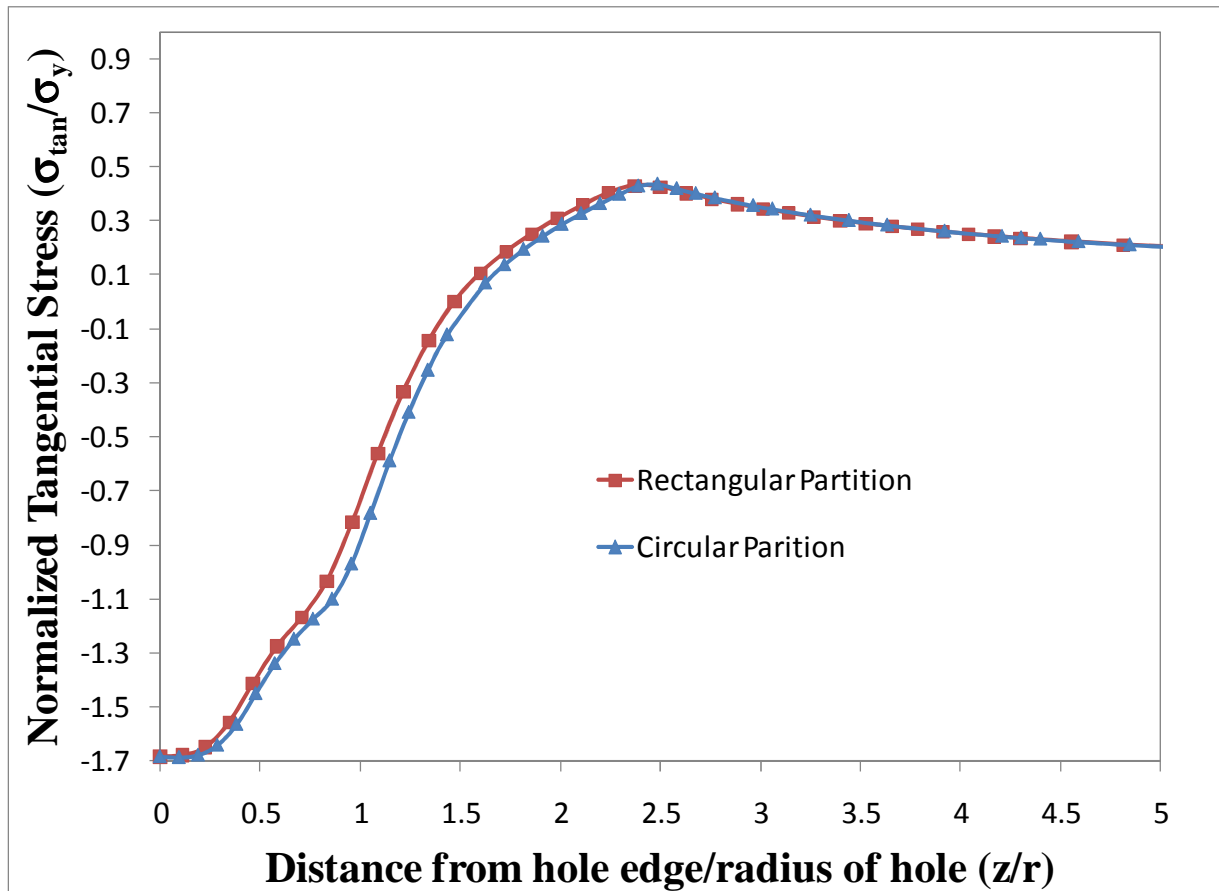


Figure 5-11 Comparison of tangential stress field in 3D uniform expansion models with circular and rectangular partitioning schemes

5.1.2 Edge Distance Model Parameters

Fatigue cracks can initiate at a variety of locations along the depth of a bridge girder. As the location of the fatigue crack changes, so too does the location of the drilled crack-stop hole. As the location of the crack-stop hole moves closer to the edge of a girder, achievable levels of beneficial residual stresses become a concern. In materials commonly used for aircraft structures, as cold expanded holes move closer to a plate's edge, a decrease in residual stress level is observed. This decrease is due to an insufficient amount of material (between the hole and the edge of the plate) to constrain the plastically deformed region surrounding the hole, not

allowing for proper “springback” of the elastically deformed region to occur. For a detailed discussion on this topic, see Section 2.3.2.1.

For this reason, effects of edge distance ratio, defined as e/D , e being the distance between the center of the hole and the free edge, and D as the diameter of the hole, were investigated for Gr. A36 steel. Edge distance ratios, e/D , investigated for this FEA were: 1.00; 1.25; 1.50; 1.75; 2.00; 2.50; 3.00; 5.00; 10.00 and 25.00. Each edge distance ratio was examined at degrees of expansion of $i = 3\%$, 4% , 5% and 6% .

The edge distance ratio models were constructed with the geometry shown in Figure 5-12. The hole diameter, 3.18 mm [0.125 in.]; outside plate dimensions, 457.2 mm [18.00 in.] x 457.2 mm [18.00 in.]; and plate thickness, 3.18 mm [0.125 in.]; remained consistent for each value of edge distance ratio. A plate thickness of 3.18 mm [0.125 in.] was used to reduce the total number of elements and degrees of freedom of the model, producing shorter model run times. The outside plate dimensions were chosen to simulate a semi-infinite edge distance ratio on the edge opposite the side of the plate in which edge distance ratios were being investigated. Edge distance ratios were adjusted by varying the dimension e , shown in Figure 5-12.

A similar mesh configuration, including mesh size and element type, as optimized for the 3D uniform expansion models, Figure 5-7 and Figure 5-8, was used for the region of high stress concentration surrounding the expanded hole. A final mesh configuration for a typical edge distance ratio model is shown in Figure 5-13.

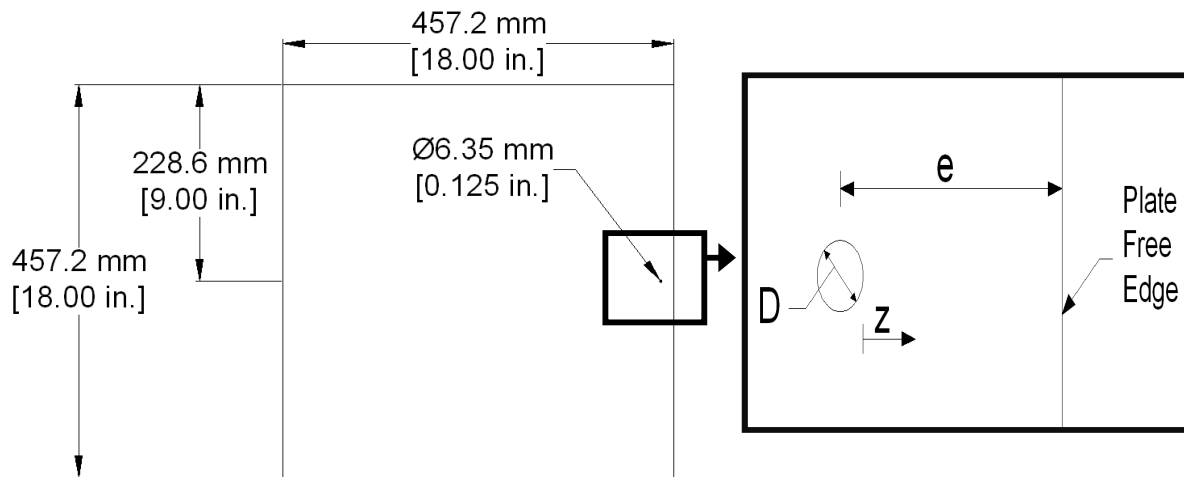


Figure 5-12 Geometric details of holes and edge distance dimensions for edge distance ratio FEMs

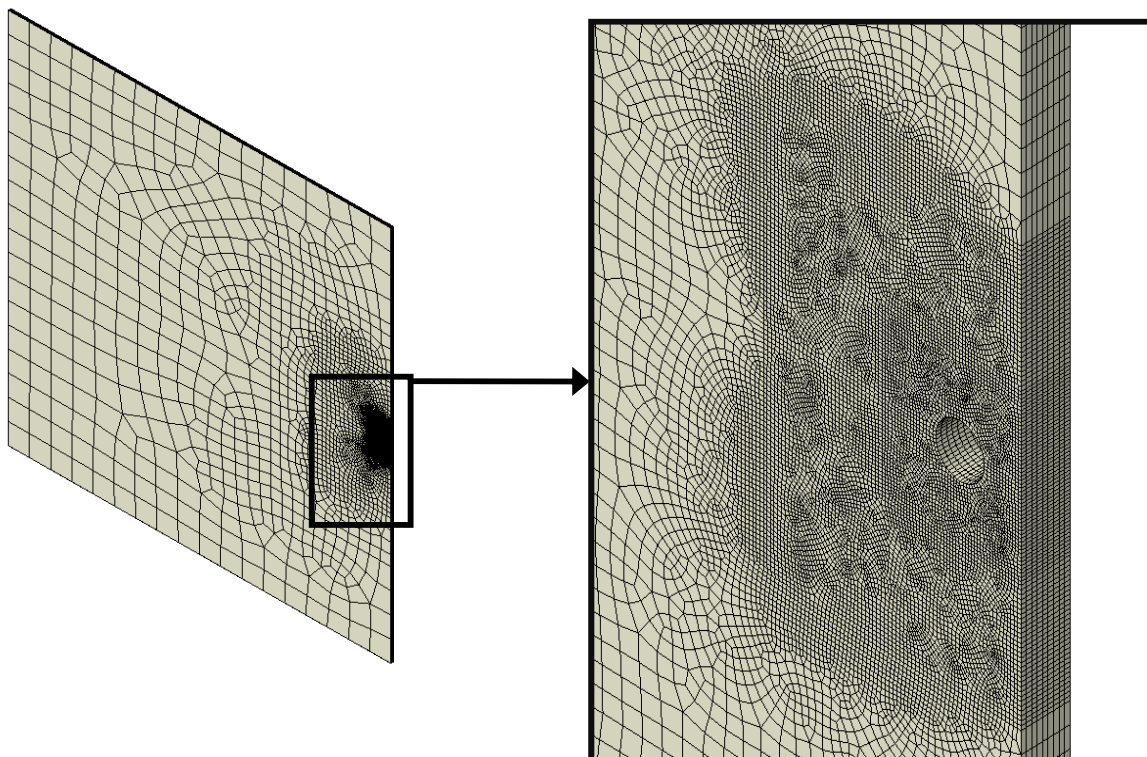


Figure 5-13: Final mesh configuration for typical edge distance ratio FEM (shown, $e/D = 2$)

5.1.3 Hole Diameter Model Parameters

Changes in hole diameter have shown little or no effect on the residual stress profile of static cold expansion specimens of finite width. A FEA study by Amrouche, A. et. al. [26] showed that changing hole diameter had no effect on the zone of compressive residual stress, maximum achievable residual stress, or the size of the plastic deformation in aluminum finite width specimens treated with static cold expansion. In the study by Amrouche, A. et. al. [26] hole diameters equal to 4.00 mm [0.157 in.], 6.00 mm [0.236 in.] and 8.00 mm [0.315 in.] were investigated. The hole diameters investigated in this report are as follows: 3.18 mm [0.125 in.]; 6.35 mm [0.250 in.] and 9.53 mm [0.375 in.].

The outside plate dimensions and plate thickness were kept the same to for all hole diameter models. The plate dimensions, 457.2 mm [18.00 in.] x 457.2 mm [18.00 in.] x 3.18 mm [0.125 in.], were chosen so that edge distance ratio did not effects results for the varying diameter holes. The partition arrangement and mesh configuration used for the hole diameter models was similar to that of the edge distance ratio models. A final mesh configuration for one of the hole diameter models is shown in Figure 5-14.

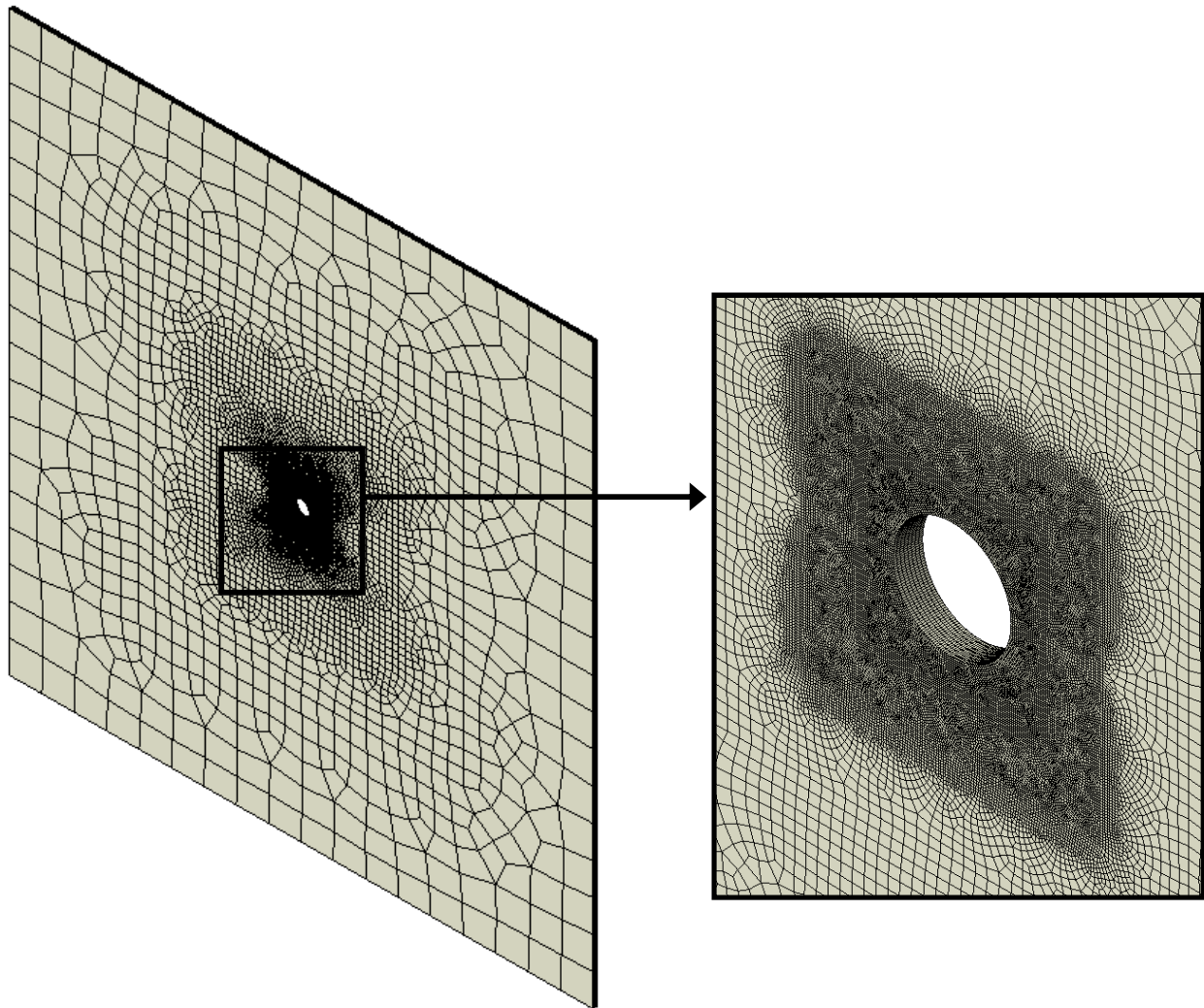


Figure 5-14: Final mesh configuration for typical hole diameter model (shown $\phi = 9.35$ mm [0.375 in.]

5.1.4 Plate Thickness Model Parameters

For aircraft material, plate thickness has been shown to significantly affect tangential residual stress fields surrounding a cold expanded hole, see discussion Section 2.3.2.3; therefore, it is reasonable to expect similar behavior in mild steel. The effects of increasing plate thickness are a larger maximum level of residual compressive stress and elastic-plastic boundary. The purpose of this section of the FEA was twofold. The first was to determine if similar effects on residual

stress fields occur in mild steel with increasing plate thickness. Second, because the field application of the PICK tool technique will be on bridge members with thicknesses far exceeding 5 mm [0.197 in.], much larger plate thicknesses were investigated to determine if at any point plate thickness not longer affects levels of residual stress. The plate thicknesses investigated were: 3.18 mm (0.125 in.); 6.35 mm [0.250 in.]; 9.53 mm [0.375 in.]; and 12.7 mm [0.500 in.].

To eliminate concerns of edge distance ratios effects, the plate thickness models were constructed as semi-infinite square plates with outside dimensions 457.2 mm [18.00 in.] x 457.2 mm [18.00 in.], as shown in Figure 5-15. A 3.18 mm [0.125 in.] hole, located in the center of the square plate, was used for each varying thickness. A mesh configuration scheme and size, as optimized in the 3D uniform expansion models, Figure 5-6 & Figure 5-8, was used for all plate thickness models, see Figure 5-16.

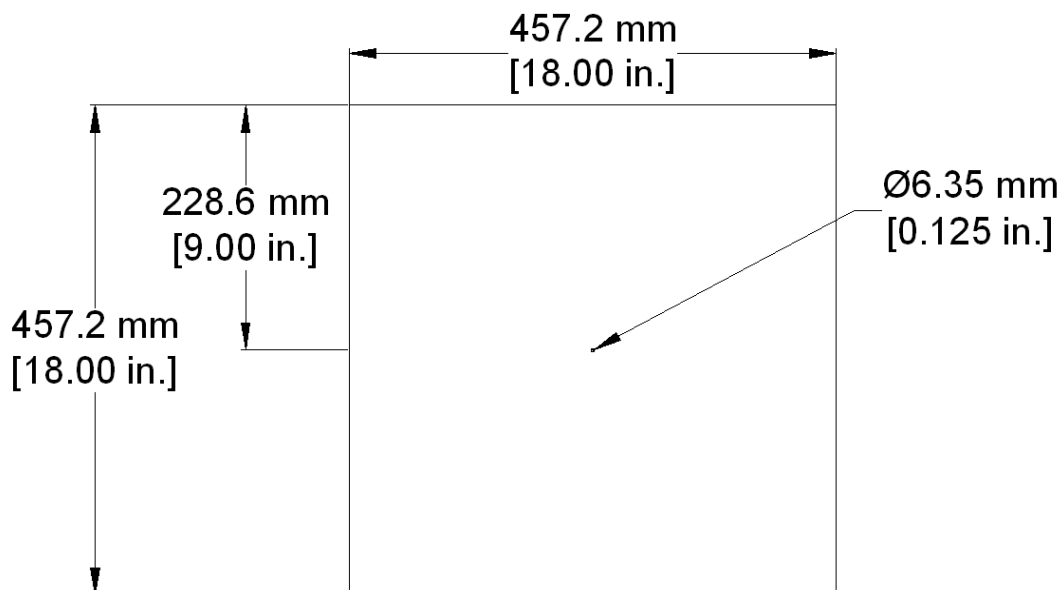


Figure 5-15: Geometric details of holes and edge distance dimensions for plate thickness FEMs

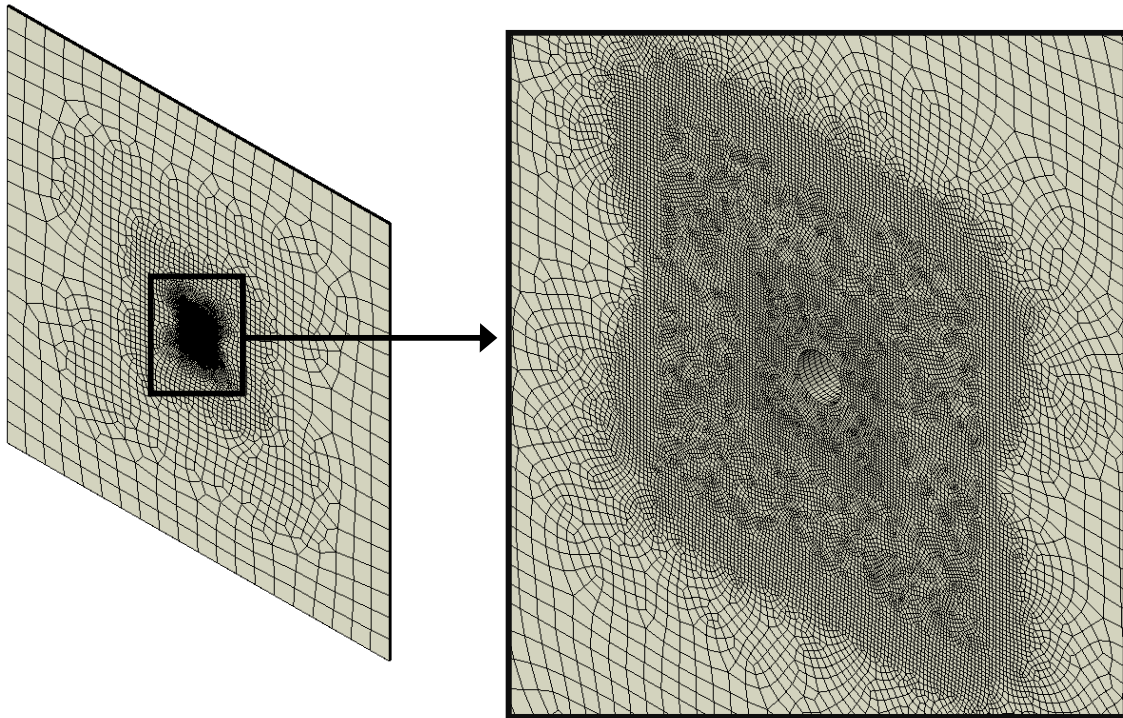


Figure 5-16: Final mesh configuration for typical plate thickness FEM (shown, 3.18 mm [0.125 in.] thick)

5.2 MODEL RESULTS

The results from all five groups of models represent theoretical values of residual stress achievable in mild steel under uniform levels of expansion. While these results should not be expected to correlate exactly with those measured in a laboratory setting, the following results have provided an excellent basis for the factors that can effect levels of residual stress as well as approximate values that can be achieved for materials commonly used in bridge construction.

5.2.1 2D Uniform Expansion Models

The initial goal of the 2D UE models was to verify the accuracy of the modeling technique of this study by comparing results with those of previously established FEA. Results of the 2D UE aluminum models, shown in Figure 5-17, were consistent with the FEA performed by de Matos, P.F.P. et. al. [22].

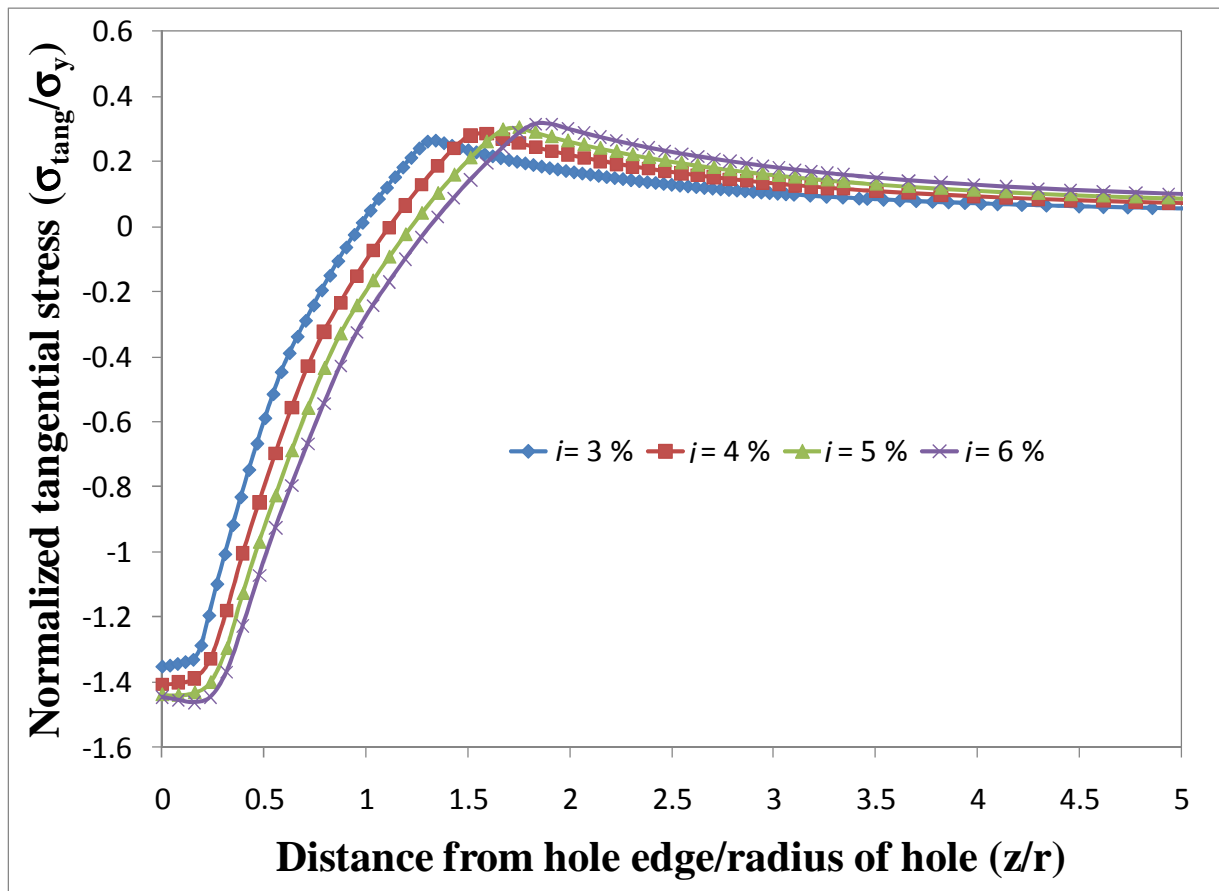


Figure 5-17: Tangential stress field for 2D UE aluminum models at various levels of expansion

As in the FEA performed by de Matos, P.F.P. et. al. [22], the peak tangential compressive stress was equal to a value just above the tensile yield strength of the material and was increased with increasing uniform levels of expansion. The zone of residual compression and the location of the elastic-plastic boundary, shown in Figure 5-17, were also consistent with the FEA performed by

de Matos, P.F.P. et. al. [22]. With increasing levels of uniform expansion, the zone of residual compression became larger and the elastic-plastic boundary moved away from the edge of the hole. The slight differences in results between this study and that performed by de Matos et. al. [22] can be attributed to the varying partition and mesh configuration, outer plate dimension, and slight differences in material properties.

Once the results of the 2D aluminum UE models had been confirmed, 2D UE models simulating mild steel material properties were investigated. The results are shown in Figure 5-19. The tangential stress field, peak compressive stress, and elastic-plastic boundary were very similar to that of the aluminum 2D UE model results, Figure 5-18.

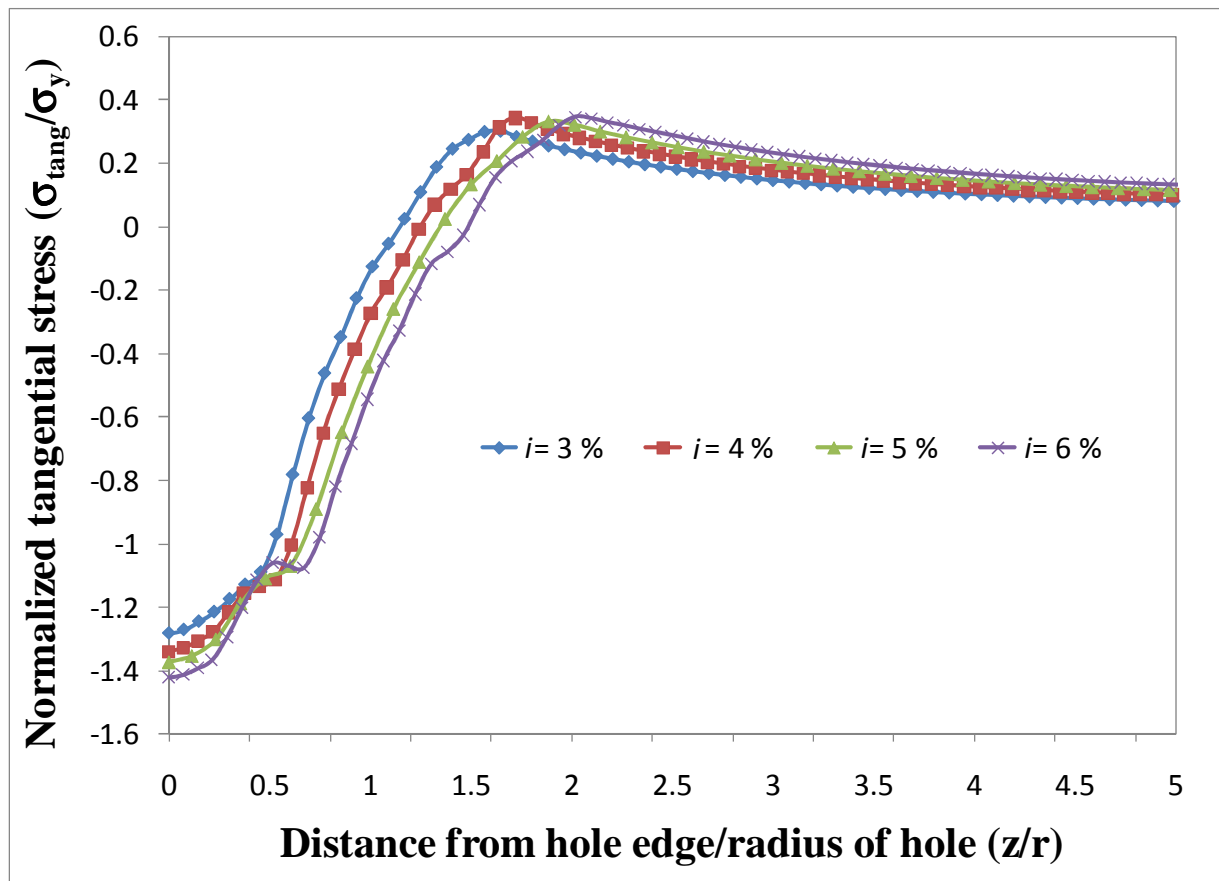


Figure 5-18: Tangential stress field for 2D UE Gr. A36 Steel at (a) 3 % (b) 4 % (c) 5 % and (d) 6 % levels of expansion

The differences between the 2D aluminum and mild steel model can be seen much more clearly in Figure 5-19. In Figure 5-19, the results of the 2D models simulating aluminum and steel material properties are plotted against one another at each varying degree of expansion. It is clear that the residual stress field for the aluminum material was significantly smoother than for the mild steel. At each degree of expansion, at a value approximately equal to the yield strength of the steel, a discontinuity in the tangential stress field appeared. This slight discontinuity in the tangential stress field was the only significant difference between the results of the two materials. These results confirm that beneficial residual stresses are achievable in mild steels similar to levels achievable in aluminum; thus, a similar improvement to fatigue life can be expected.

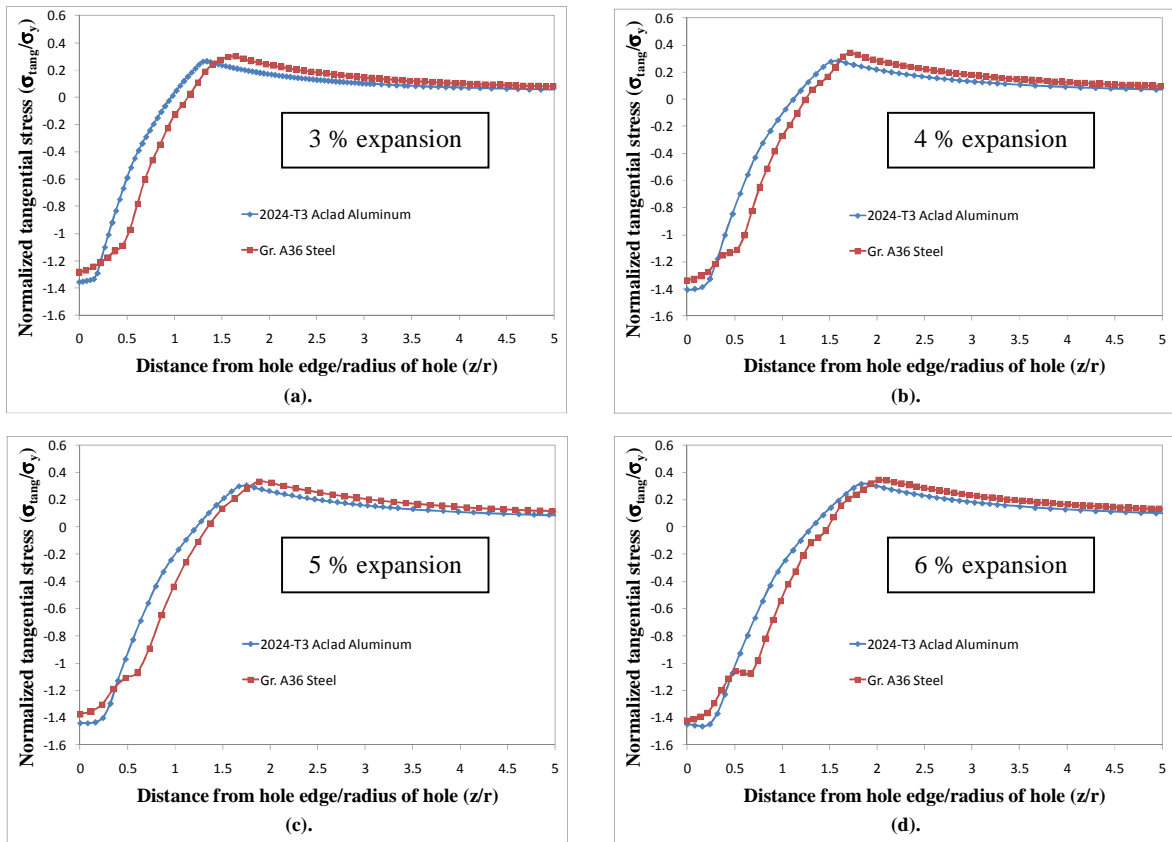


Figure 5-19: Tangential stress field for 2D UE 2024-T3 Alclad Aluminum vs. Gr. A36 Steel at (a) 3 % (b) 4 % (c) 5 % and (d) 6 % levels of expansion

5.2.2 3D Uniform Expansion Results

The 2D UE results confirmed that beneficial residual stresses, similar to those achievable through static cold expansion in aluminum, could be achieved in mild steel. The focus now shifted to comparing results of the 2D mild steel models with those of the 3D UE models. The results of the 3D UE mild steel models, at mid-thickness of the 3.18 mm [0.1215 in.] plate are shown for varying expansions in Figure 5-20.

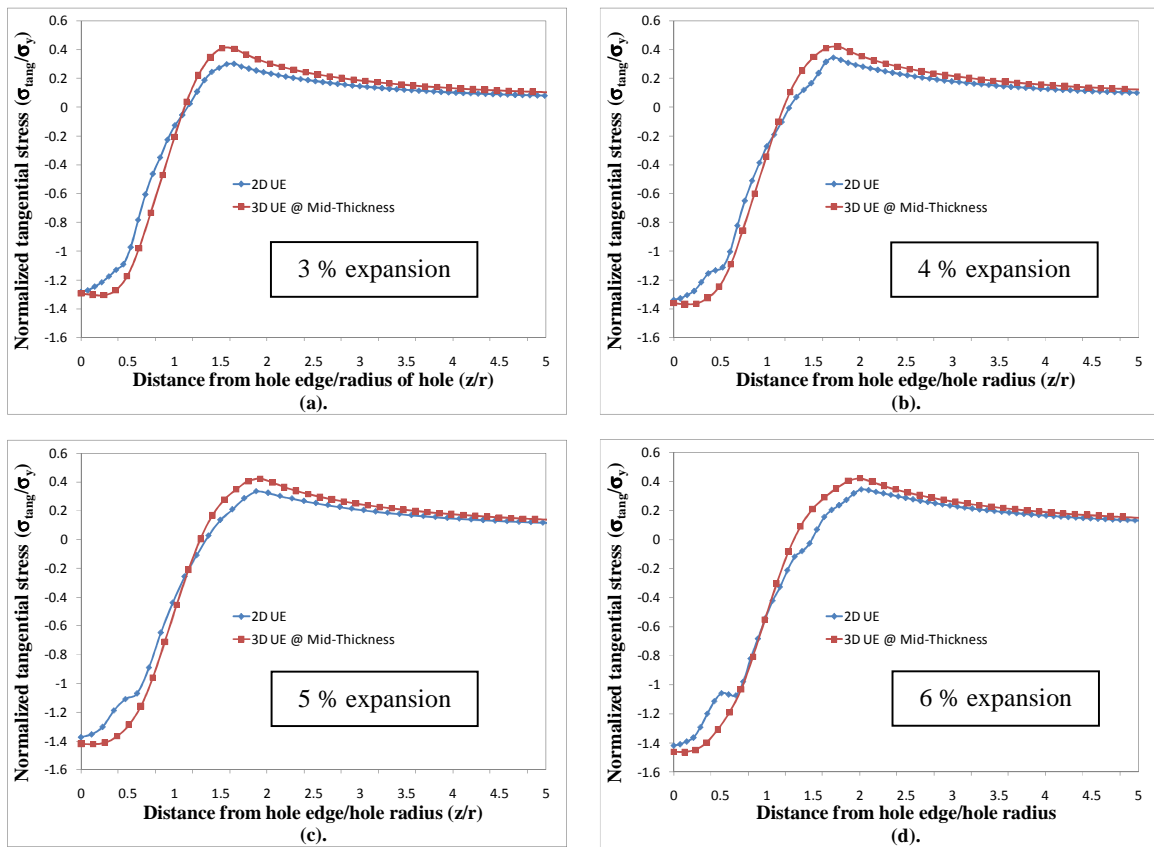
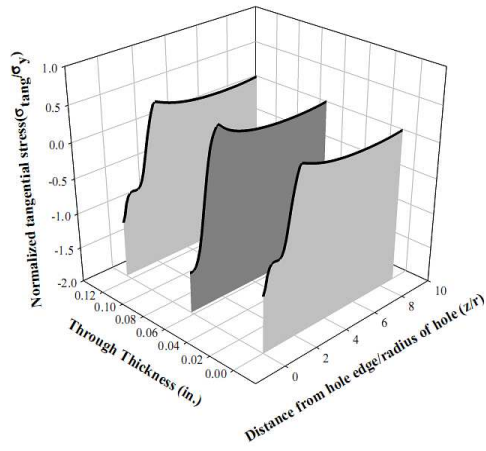


Figure 5-20: Tangential stress field for 2D UE models versus 3D UE models @ mid-thickness for various degrees of expansion (a) 3 %, (b). 4 %, (c). 5 % and (d). 6 %

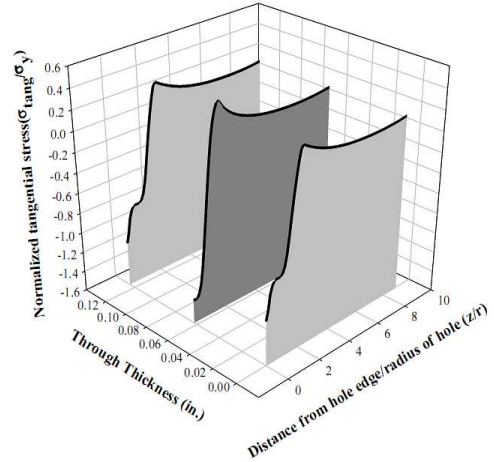
As shown in Figure 5-20, the relative magnitudes of peak residual compressive stress, elastic-plastic boundary, and zone of residual compression are similar at the mid-thickness of the 3D UE mild steel models as the 2D UE mild steel models. The simpler 2D UE mild steel models were fairly consistent with those of the 3D UE mild steel models at mid-thickness. While the compressive stress at the location of the hole was almost identical for both sets of models, the 3D UE mild steel models generated larger peak compressive stresses (no more than a 3.5 % increase) as well as larger zones of residual compression. In addition, the 3D UE mild steel models did not experience the discontinuity in the stress field near the tensile yield strength of the material. These differences are clearly a result of the effects of confinement provided by the

thickness of the plate in the 3D UE mild steel models that the 2D models simulations do not capture.

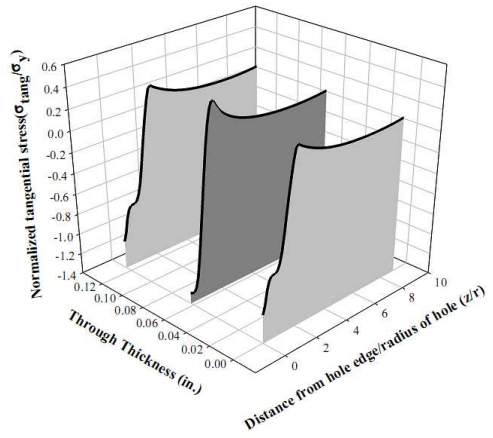
Figure 5-21 illustrates the through-thickness tangential residual stress distribution for varying levels of expansion. It is important to note that residual stress levels peak at mid-thickness and decay moving towards the surface. This is significant because levels of compressive residual stress are the reason for reduction in stress intensity factor around cold expanded hole and the main contributor to fatigue life improvement. The effects of varying residual stress through the thickness of a plate must be considered when predicting levels of fatigue life improvement.



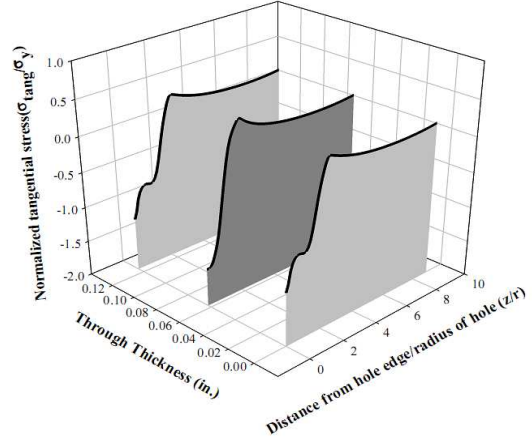
(a).



(b).



(c).



(d).

Figure 5-21: Through thickness tangential stress field for 3D UE models at various degrees of expansion (a) 3 %, (b). 4 %, (c). 5 % and (d). 6 %

Edge Distance Model Results

The effects of varying edge distance ratios for a mild steel material were shown to be similar to those exhibited for aerospace material (aluminum). As shown in Figures 5-22-5-25, the level of peak compressive stress, zone of residual compressive stress, and elastic-plastic boundary were reduced for lower levels of edge distance ratio. This trend was valid until a value of e/D became greater than or equal to 3. Once an edge distance ratio of 3 was met or exceeded, edge distance no longer affected the shape or magnitude of the tangential residual stresses. The same e/D ratio was found to exist through studies of the effects of varying edge distance ratio in aluminums, as discussed in Section 2.3.2.1.

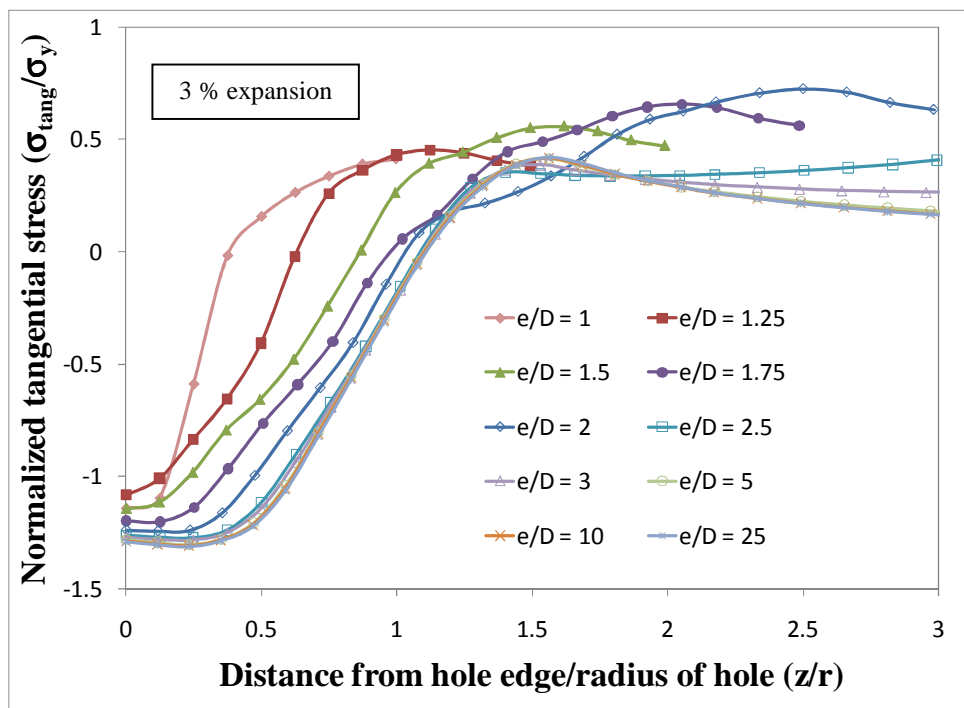


Figure 5-22: Tangential stress field for Edge Distance Model at 3 Percent Expansion

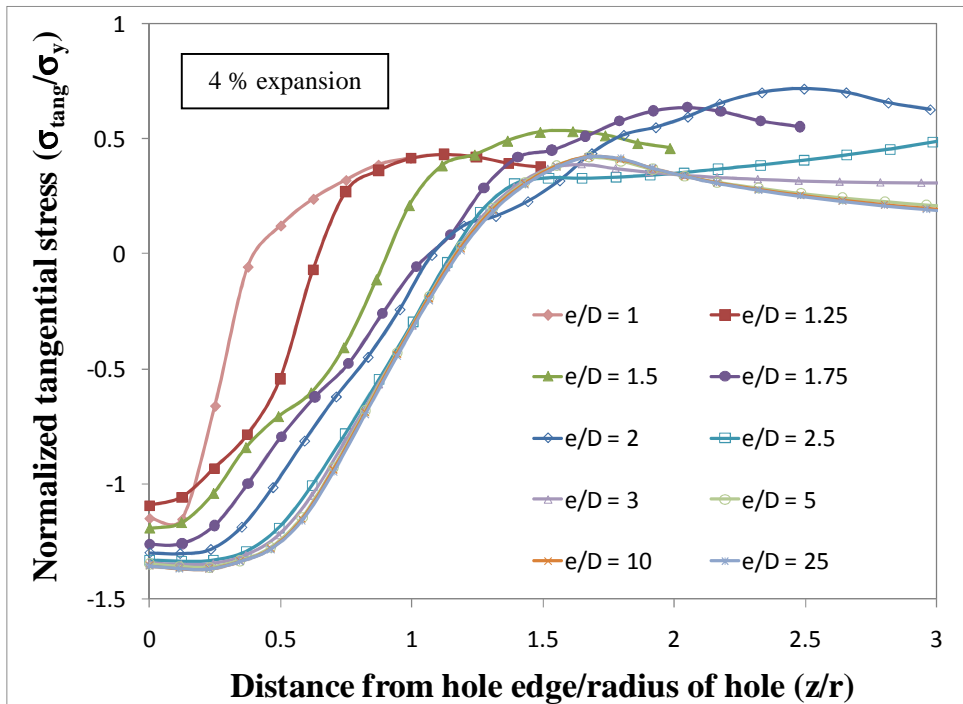


Figure 5-23: Tangential stress field for Edge Distance Model at 4 Percent Expansion

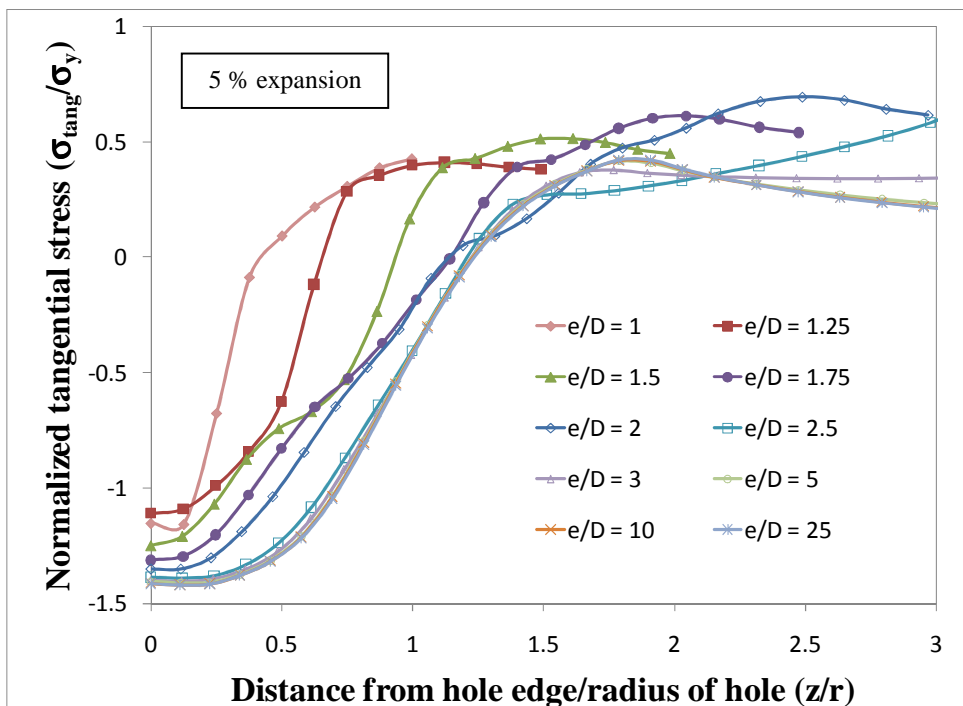


Figure 5-24: Tangential stress field for Edge Distance Model at 5 Percent Expansion

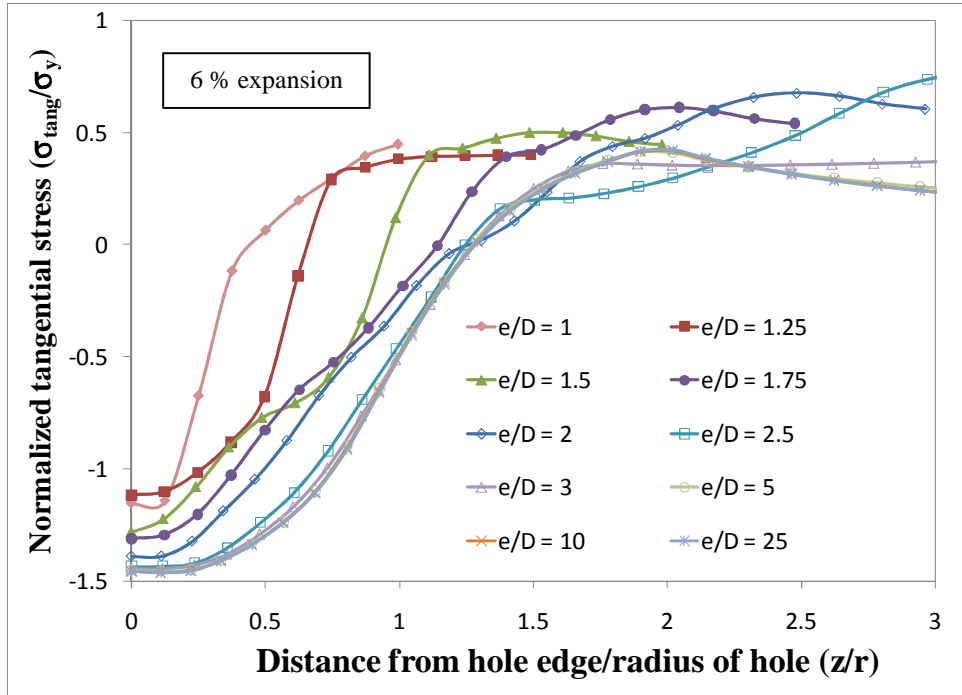


Figure 5-25: Tangential stress field for Edge Distance Model at 6 Percent Expansion

5.2.3 Hole Diameter Model Results

The results from the hole diameter models, simulating a uniform 4 % expansion, were consistent with past investigations performed on materials commonly used in the aerospace industry. As illustrated in Figure 5-26, as hole diameter increased, beneficial residual stresses were able to be achieved with minimum change in magnitude. The results give confidence to the idea that crack-stop holes of any size may be able to be effectively treated with cold expansion.

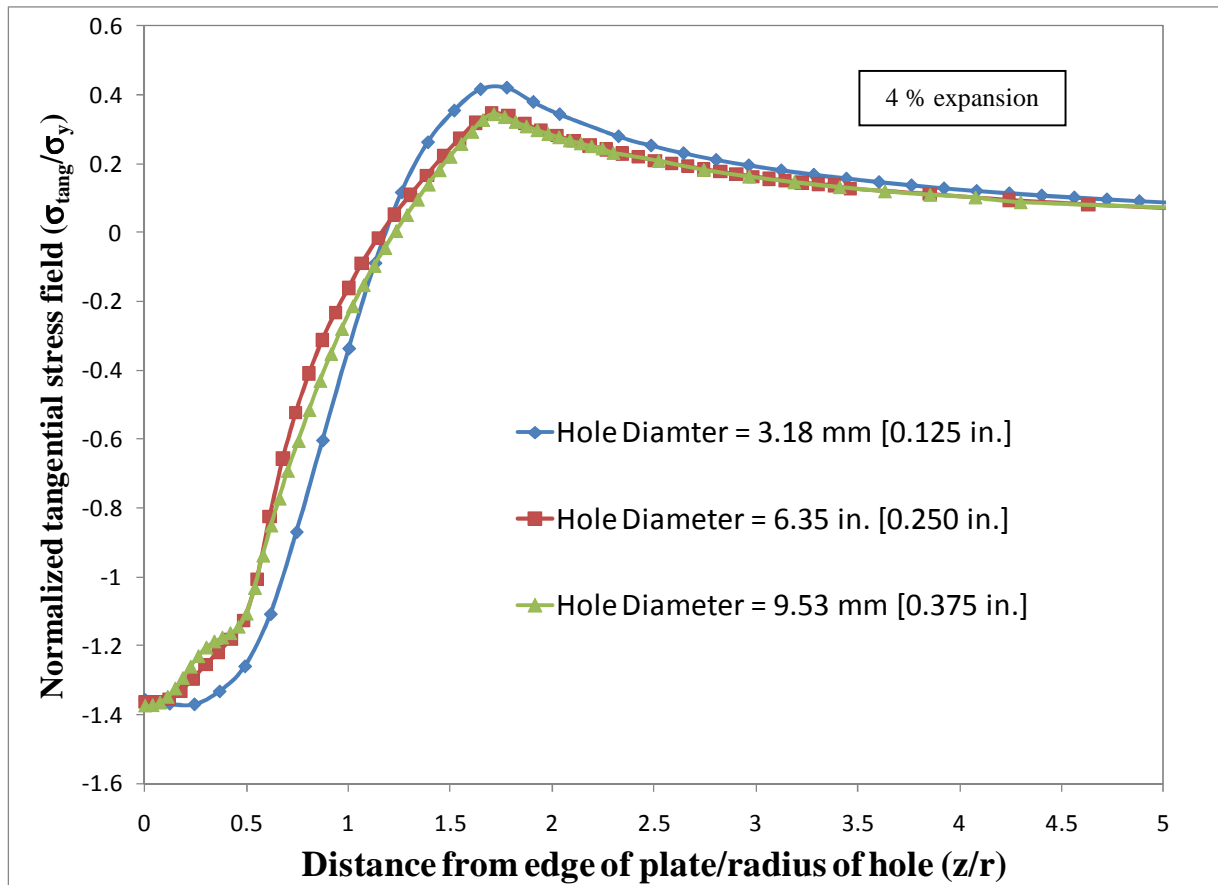


Figure 5-26: Tangential stress field for hole diameter models at 4 Percent Expansion

5.2.4 Plate Thickness Model Results

The results of the plate thickness models were consistent with findings of past FEA [8]. As in previous analytical investigations, increasing plate thickness increased the maximum level of residual compressive stress and compressive stresses were maintained for a farther distance away from the hole.

However, as illustrated in Figure 5-27, the benefits of increasing plate thickness appear to become less significant as plate thickness approached 12.7 mm [0.500 in.]. This point was illustrated by the minimal gain in residual stress levels as plate thickness was increased from 9.53 mm [0.375 in.] to 12.7 mm [0.500 in.]. This may not be as simple to confirm in a

laboratory setting, considering cold working using present techniques becomes more difficult with increased plate thickness [8].

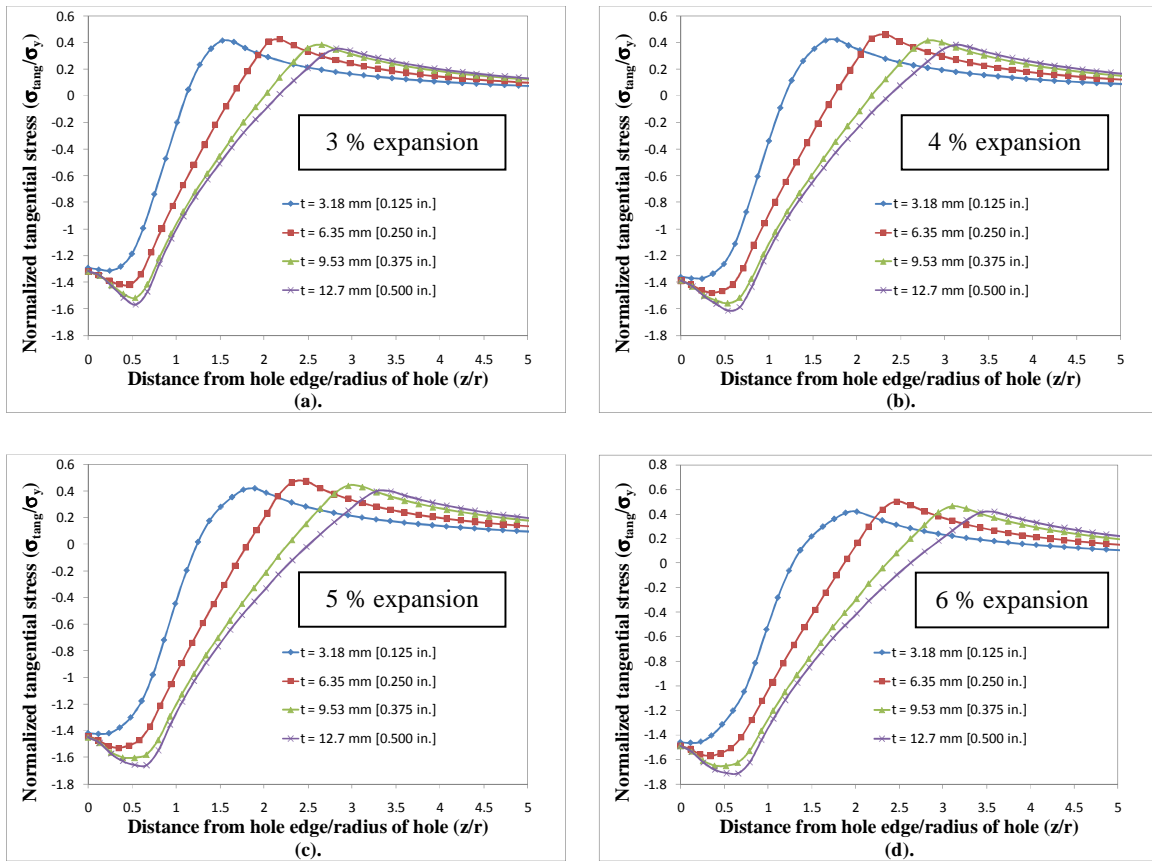


Figure 5-27: Tangential stress field for varying plate thickness models at various degrees of expansion (a) 3 %, (b). 4 %, (c). 5 % and (d). 6 %

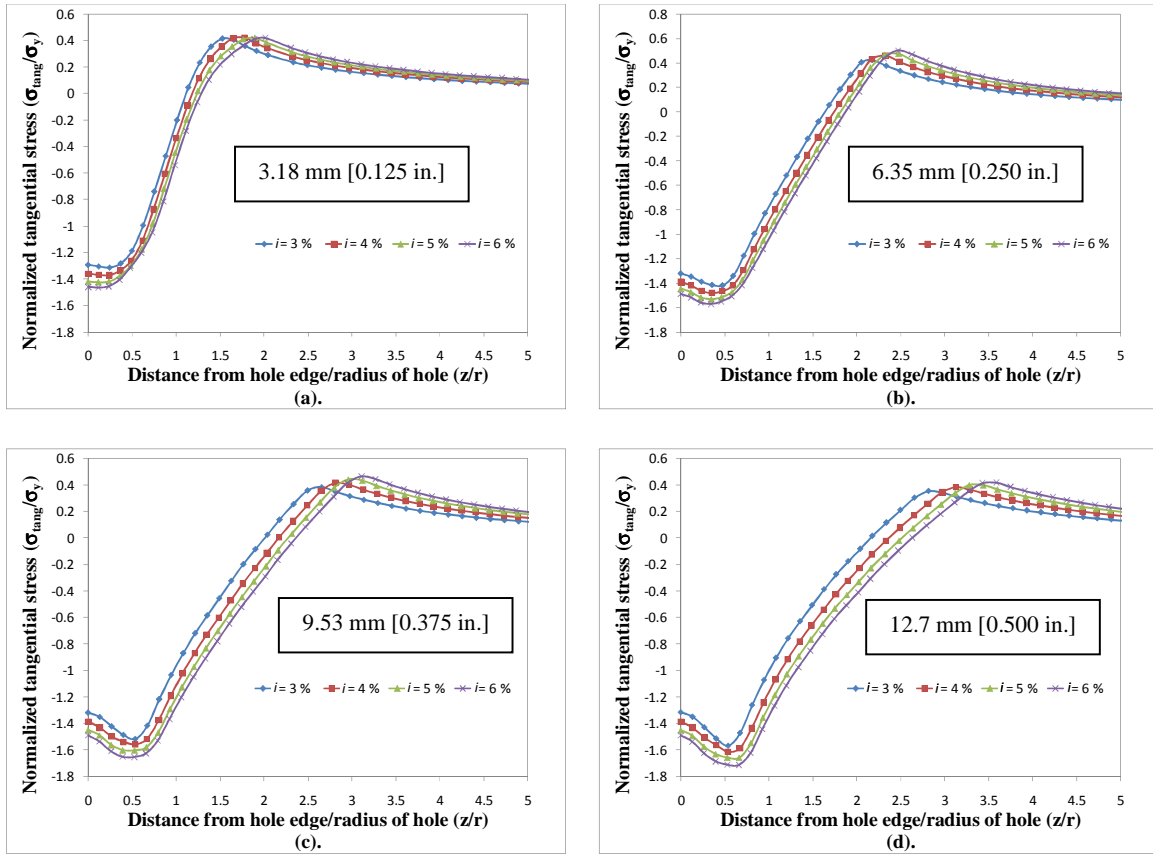


Figure 5-28: Tangential stress field for varying expansion models at various plate thicknesses (a) 3.18 mm [0.125 in.], (b) 3.65 mm [0.250 in.] (c) 9.53 mm [0.375 in.] and (d) 12.7 mm [0.500 in.]

CHAPTER 6 CONCLUSIONS AND RECCOMENDATIONS

6.1 CONCLUSIONS

The results of a combined analytical and experimental study of the fatigue behavior of notched steel specimens treated with a PICK tool are summarized. The PICK tool is used to apply a compressive pres-stress coupled with grain refinement around holes used to arrest fatigue cracks in steel bridges. Both Finite Element Analysis and experiment fatigue tests show the PICK tool technique improves the fatigue life of specimens with round notches. The development of the PICK tool is described in a separate study.

The FEA portion of this study investigated the ability of cold expansion to produce beneficial residual stresses in mild steel materials. In addition, geometric parameters shown to effect levels of residual stress in aerospace materials were investigated for cold expanded holes in mild steel plates.

The PICK tool technique has demonstrated that fatigue life improvement resulting from cold expansion can be carried over from materials commonly used in aerospace (aluminum) to materials commonly used in bridge construction (in this case, mild steel). The PICK tool produced a fatigue life improvement of approximately 4 times that of the untreated specimens. The fatigue life improvement of 4 falls directly in the range of 3-10 that has been shown can be produced through static cold expansion in aerospace materials [5-8]. It is unclear at this point whether the ultrasonic treatment is providing additional benefits beyond the basic cold expansion produced by the PICK tool. The natural progression of testing would be to treat specimens without the use of ultrasonic impact and compare those fatigue life results with the PICK treated specimens with ultrasonic impact. To follow up on the investigation of comparing treatment of the PICK tool both with and without ultrasonic impact, a laboratory investigation of the residual

stress fields surrounding the treated holes and grain size of the area surrounding the hole should be performed.

The results of the finite element study confirmed that beneficial residual compressive stresses can be produced in mild steel similar levels achievable in of materials commonly used in the aerospace industry (aluminum). Additionally, adjusting geometric parameters found to effect levels of residual stress in aircraft material had similar effects on the behavior of mild steel.

For the uniform expansion mild steel models, it was found that as the level of uniform expansion increased so too did the zone of residual compression, maximum peak residual compressive stress, and the elastic-plastic boundary. This finding was consistent with those of previous studies investigating cold working of aerospace materials.

Edge distance ratio was also shown to have a similar effect on mild steels as is seen in aircraft material. At an edge distance ratios greater than three, there is no significant change in the level of residual stress. However, if edge distance ratios are lower than three, levels of beneficial residual compressive stresses tend to decrease, and decreased fatigue life improvement can be expected.

Consistent with previous investigations, varying hole diameter showed no significant effect on the residual stress profile of cold worked crack-stop holes. This signifies that application of cold expansion may be effective for treatment of hole sizes to be seen in the field.

Due to additional levels of confinement with increasing plate thickness, levels of beneficial residual stress increased. However, the FEA results suggest that there may be a limit to the levels of residual stress that can be achieved with increasing plate thickness. In other words, there is a point in which increasing thickness no longer provides an improvement to levels of residual stress. This is significant considering the size of member thickness that will be needed

to be treated in bridge crack-stop hole situations will be thicker than many cold expansion applications in the aerospace industry. It should be recognized that with increasing plate thickness the ability to effectively treat crack-stop holes will increase in difficulty.

6.2 RECOMMENDATIONS

The effectiveness of treatment with the PICK tool remains at a developmental stage. It is clear through experimental data from this investigation that the PICK tool does have the ability to enhance fatigue life in uniaxial tensile application for thin plates. The next step in the laboratory investigation is the treatment and fatigue testing of 6.35 mm [0.250 in.] fatigue specimens. If the PICK tool is proven successful in enhancing fatigue life of the 6.35 mm [0.250 in.] specimens, it can be concluded that the PICK tool, in uniaxial tension applications, can be an effective form of treatment for plates of varying thickness. If the PICK tool shows it can enhance fatigue life of the 6.35 mm [0.250 in.] plate, the fatigue specimens must be redesigned to more closely simulate a crack-stop hole scenario.

6.3 FUTURE WORK

This type of uniaxial crack-stop hole testing has been performed on aerospace materials in studies such as the one performed by Amrouche, A. et. al. [26]. In this type of investigation, the laboratory specimen will not have a hole drilled out of an initially uncracked plate; rather, the hole will be drilled at the tip of a flaw which is initiated by a preinstalled notch at the edge of the plate. The crack-stop hole is then treated and tested in uniaxial tension until the point where crack reinitiates.

The ultimate goal of the PICK tool is the ability to treat and improve fatigue life of crack-stop holes in field applications. For this reason, a new design of the PICK tool will be necessary

for application in field conditions. The final stage of the PICK tool development will be to test the redesigned PICK tool, in a laboratory setting, on scaled bridge members subjected to a realistic crack- stop hole's out-of-plane stress environment.

The PICK tool is a technique that could extend the lives of cracked steel bridge components with minimal cost and interruption to the traveling public. The tool has shown the ability to improve fatigue life of crack-stop holes by a factor of 4. With continuing optimization of PICK tool parameters this value is expected to increase. This technique is of particular importance, considering bridges throughout the country contain connection details susceptible to the formation of fatigue cracks.

APPENDIX A

DETAILED FATIGUE TESTING PROCEDURES

MTS Load Frame Fatigue Test Procedure

The MTS fatigue test procedure began by calculating the appropriate net section area at the location of the hole. The maximum, minimum, and average load were then calculated for each specimen. Once appropriate loads had been determined, the test frequency was inputted along with the maximum number of cycles that the specimen could see before a predefined infinite fatigue life was reached. The final procedure, used for all fatigue specimens, was as follows:

1. Ramp to a load of 444.8 N [100 lbs] in 30 sec.
2. Hold 444.8 N [100 lb] load for a time period of 30 sec.
3. Ramp to average load (determined on an individual basis for each specimen) in a time period of 30 sec.
4. Hold average load for a time period of 30 sec.
5. Begin cycling between maximum and minimum values for appropriate number of cycles and test frequency.
6. Data acquisition file created so that the linear data interval was collected every 100 cycles. The maximum number of cycles stored was set on an individual basis for each specimen.

APPENDIX B

TENSION TEST DATA

B.1 MTS TEST FRAME TENSION TEST PROCEDURE

The MTS test frame was used to test the 6.35 mm [0.250 in.] tension specimens. All tension testing was performed in accordance with ASTM specification E8. Cross head displacement was individually set for both the determination of yield strength and ultimate tensile strength as outlined in ASTM 08. Up to the point of yielding, the rate of separation, set for the MTS test frame, was 0.45 mm/min. [0.018 in./min.]. This cross head displacement rate provided a loading rate between the ASTM specification E8 limits of 68.9 MPa and 689 MPa [10,000 psi and 100,000 psi].

After yielding behavior was recorded, the loading rate was changed to meet ASTM 08 specified strain rates of 0.05 mm/mm/min. to 0.5 mm/mm/min. [0.05 in./in./min. to 0.5 in./in./min.] This strain rate was maintained until specified failure.

The test procedure for all 6.35 mm [0.250 in.] tension specimens, created with the MTS user interface TestStar, was as follows:

1. Ramp to 444.8 N [100 lb] in a time period of 30 sec
2. Load hold at 444.8 N [100 lb] for a time period of 30 sec
3. Ramp to a displacement beyond yield to 5.84 mm [0.23 in.] in a time period of 783 sec.
4. Ramp to a displacement of 68.6 mm [2.7 in.] in a time period of 200 sec.
5. Failure detection defined as load falling below 50% of max load seen during step 4.

Once failure is detected station interlocks and test is shut down.

B.2 BALDWIN FRAME TENSION TEST PROCEDURE

The Baldwin test frame was used for testing tension specimens with a thickness of 3.18 mm [0.125 in.]. As with the procedure written for the MTS test frame, all portions of the Baldwin test program were written in accordance with ASTM specification E8. This included specifying appropriate load rates and strain rates up to the points of both yielding and ultimate tensile strength.

The test procedure for all 3.18 mm [0.125 in.] tension specimens, created with the Baldwin user interface, Partner, was as follows:

1. Ramp to 444.8 N [100 lb] at a load rate of 444.8 N/min. [100 lb/min.]
2. Ramp to a displacement of 1.52 mm [0.06 in.] at a displacement rate of 0.127 mm [0.005 in./min.]
3. Ramp in displacement control at a displacement rate of 5.08 mm [0.2 in./min.] until specimen can no longer take any load.

B.3 LINEAR STRESS STRAIN BEHAVIOR

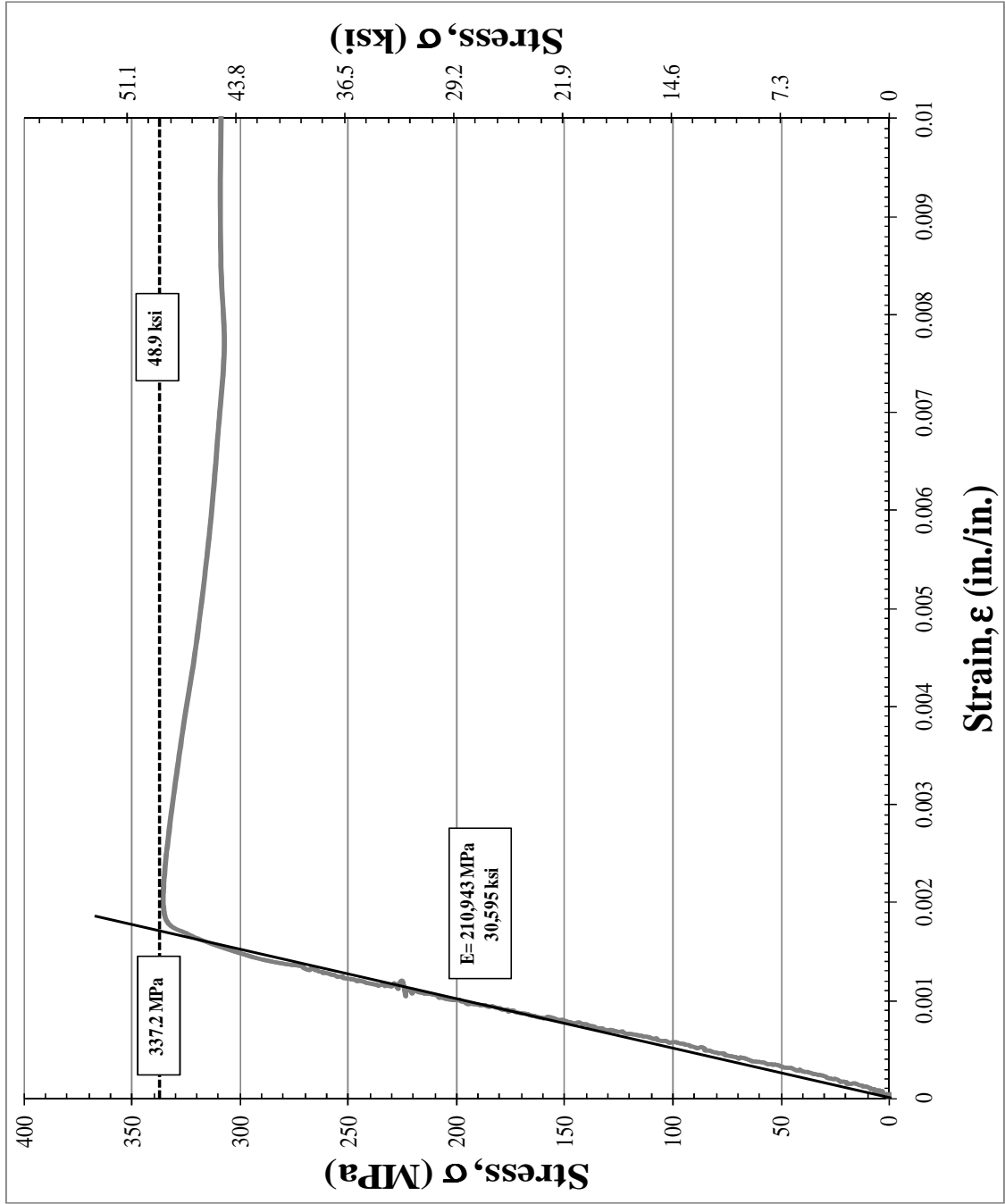


Figure B-1: Stress-Strain plot used to determine yield strength for specimen 0.125_AT1

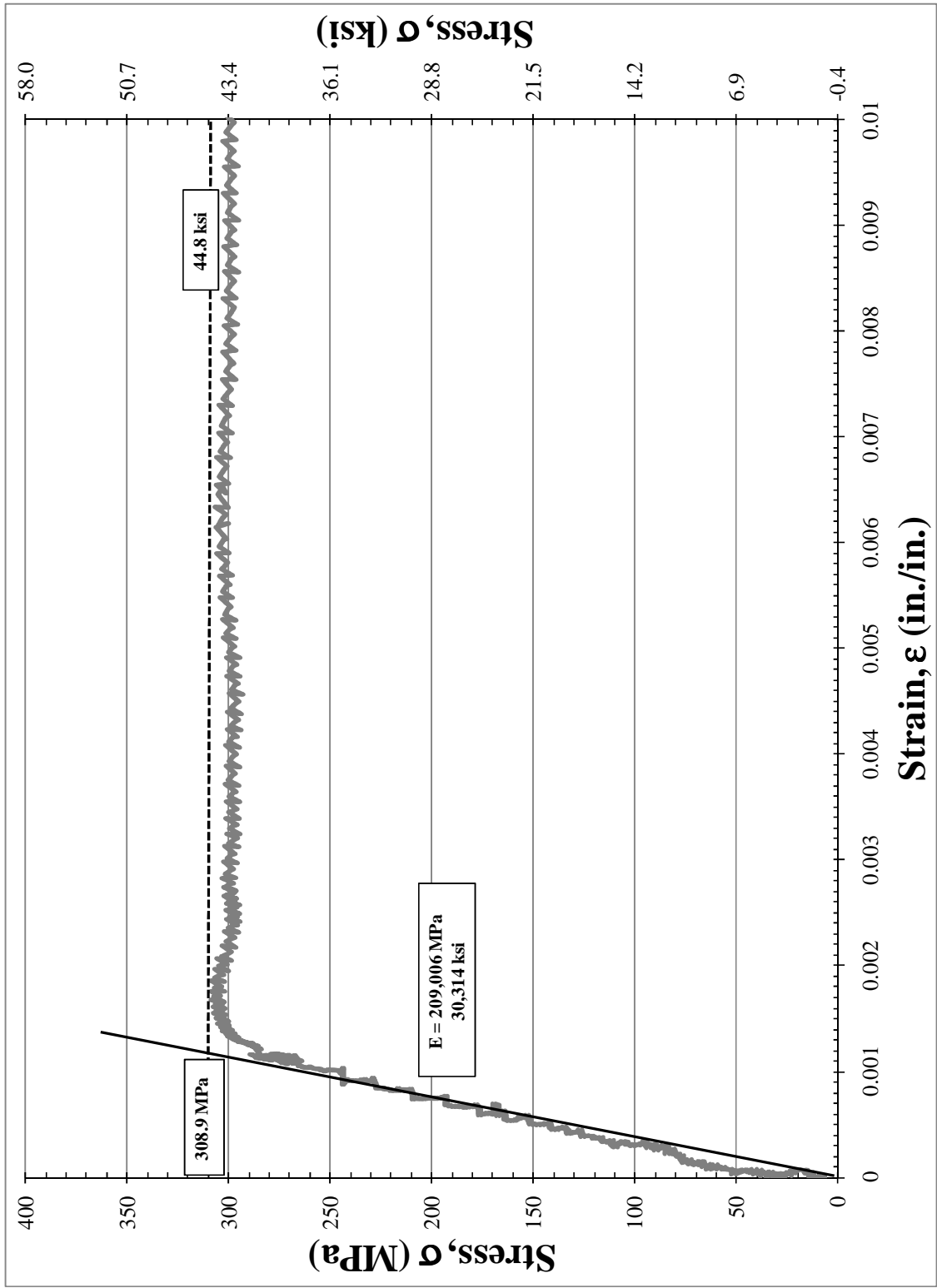


Figure B-2: Stress-Strain plot used to determine yield strength for specimen 0.125_AT3

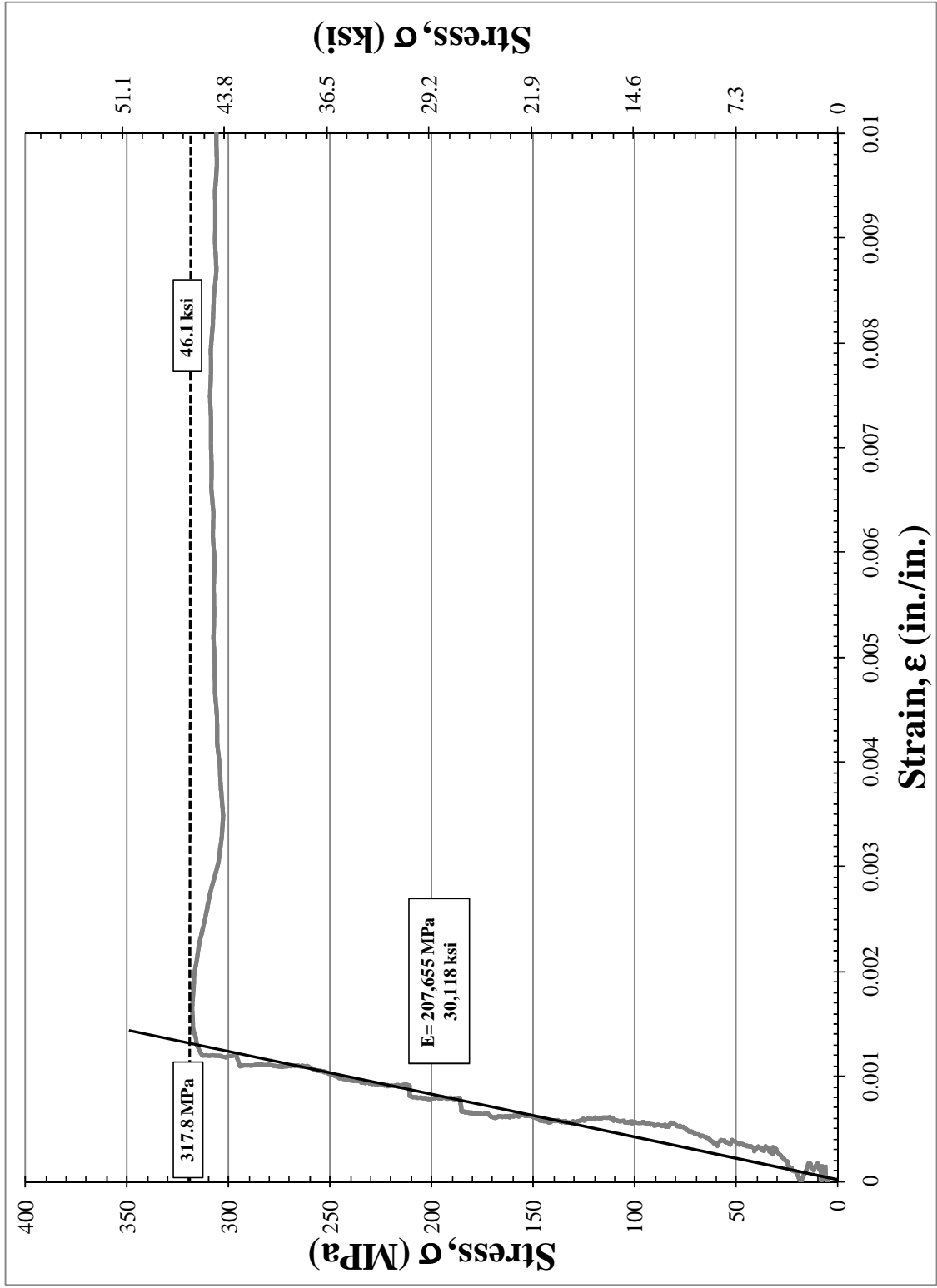


Figure B-3: Stress-Strain plot used to determine yield strength for specimen 0.125_AT4

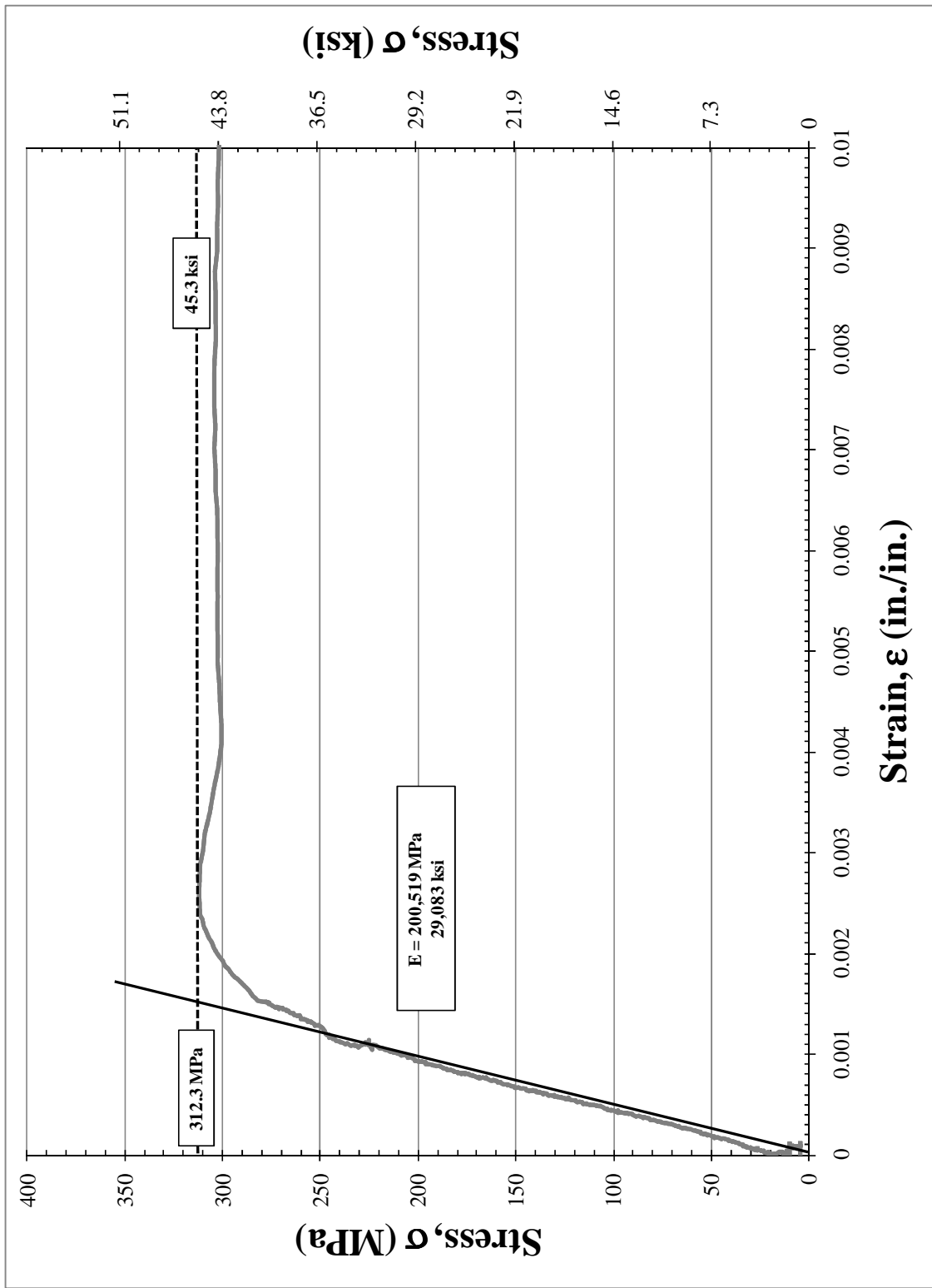


Figure B-4: Stress-Strain plot used to determine yield strength for specimen 0.125_AT5

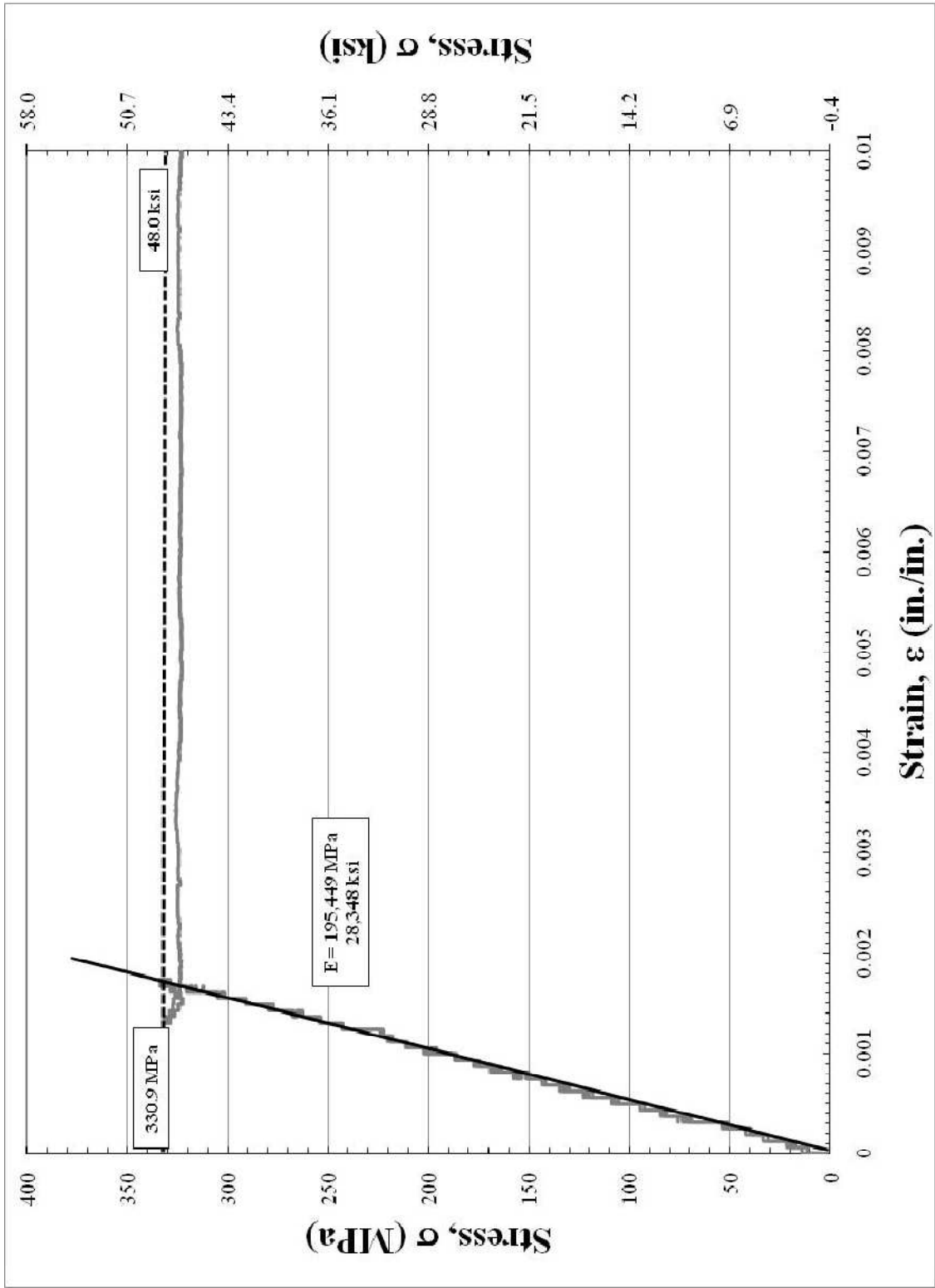


Figure B-5: Stress-Strain plot used to determine yield strength for specimen 0.25_AT1

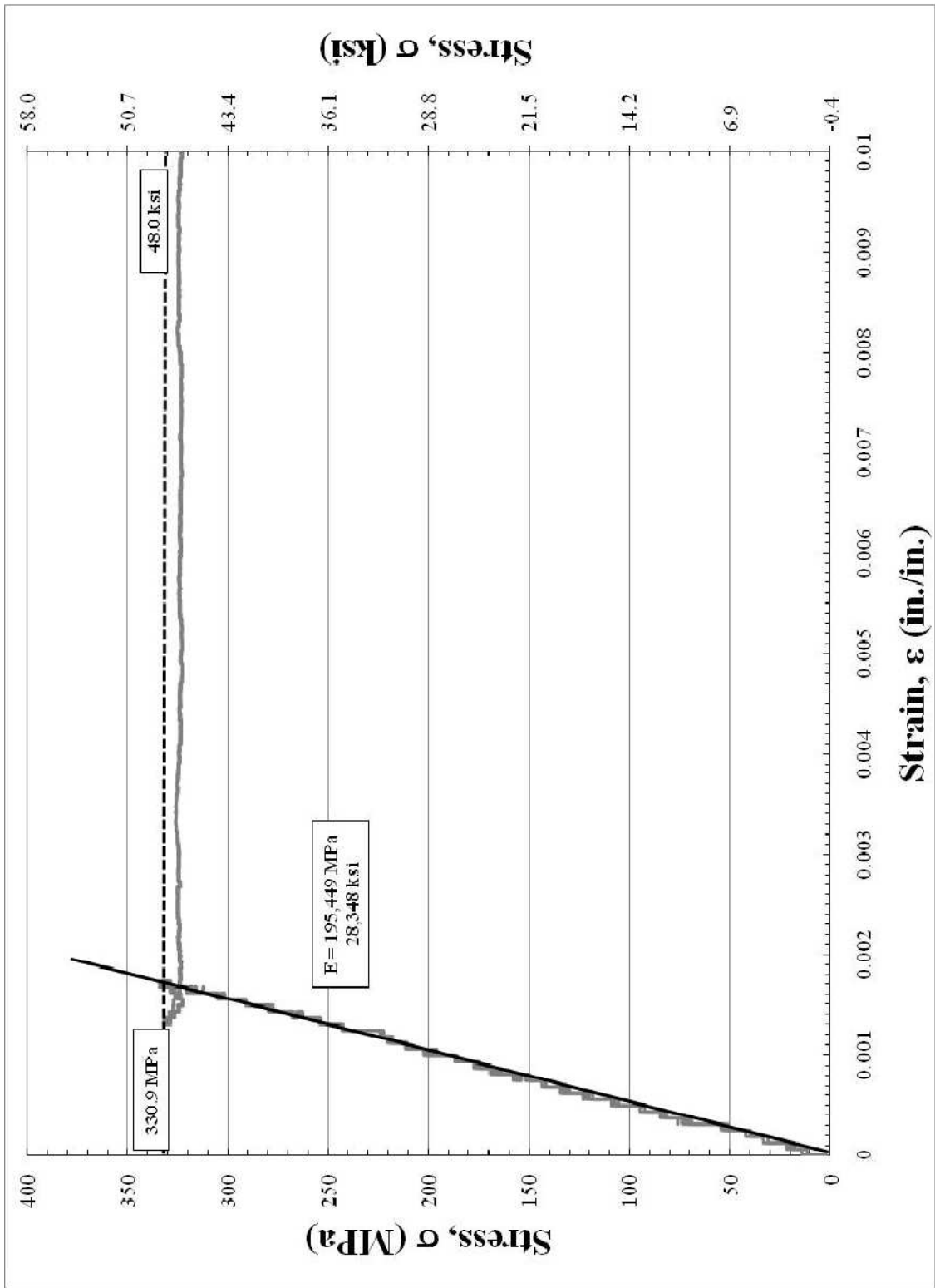


Figure B-6: Stress-Strain plot used to determine yield strength for specimen 0.25_AT2

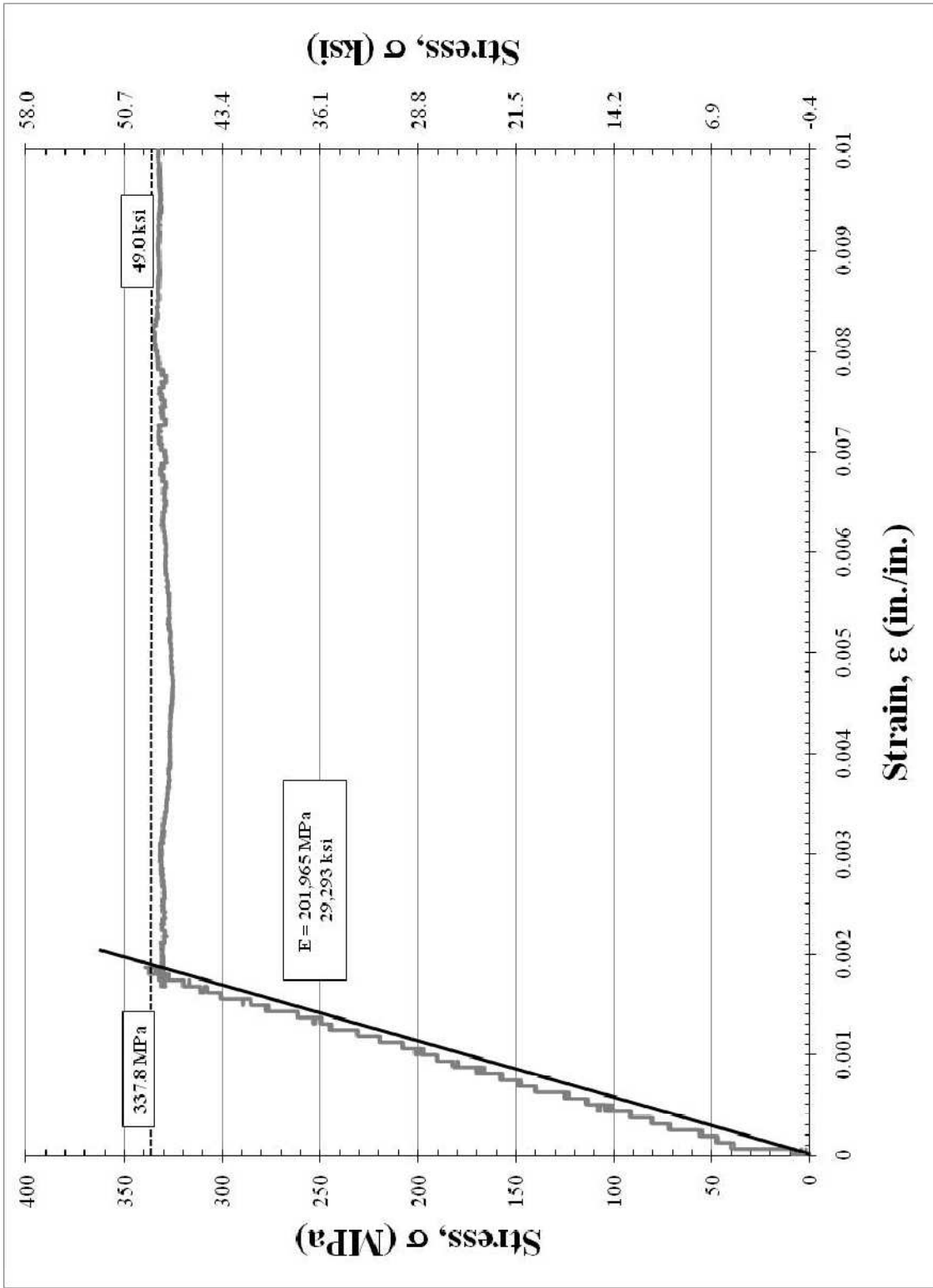


Figure B-7: Stress-Strain plot used to determine yield strength for specimen 0.25_AT3

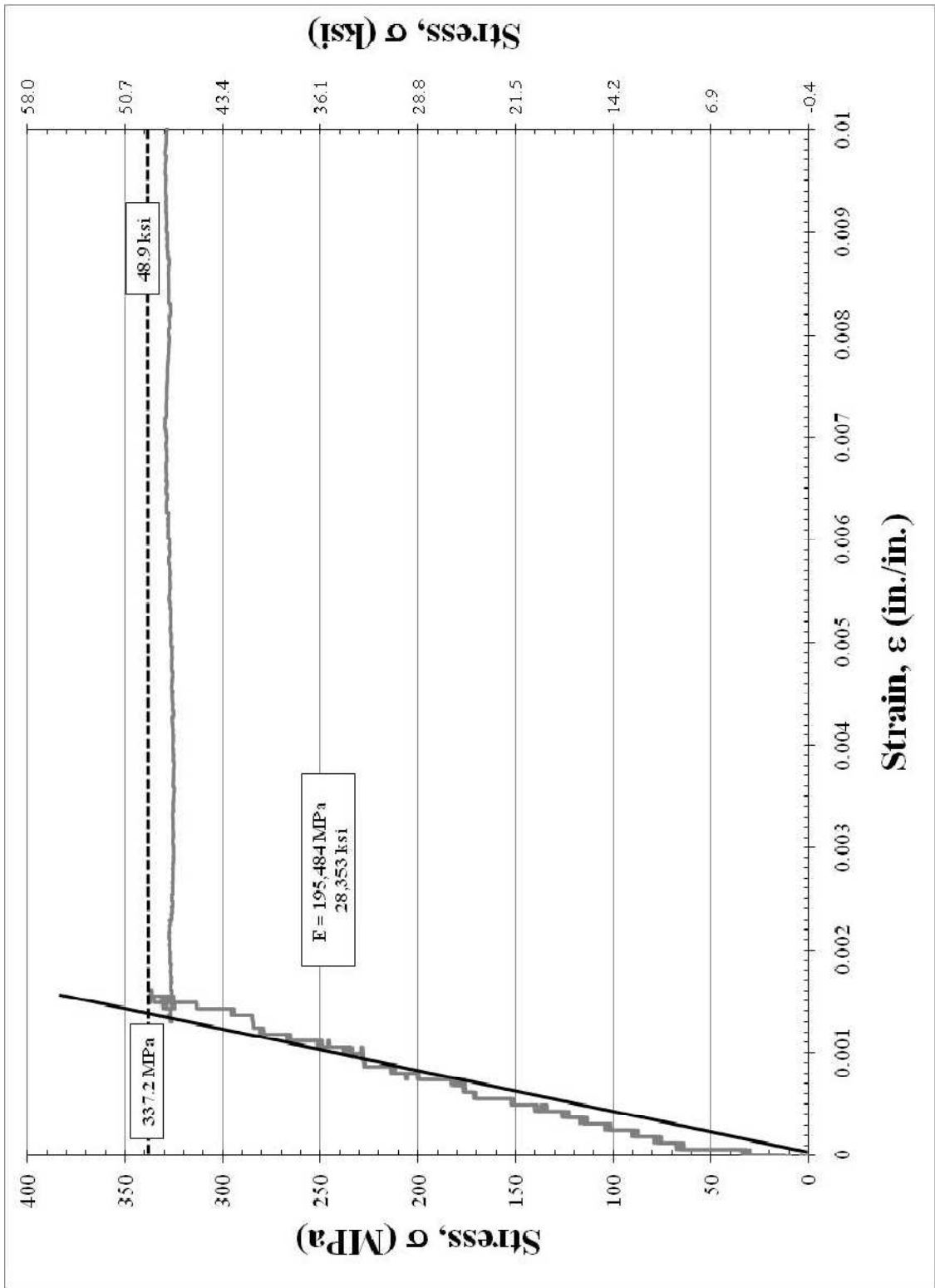


Figure B-8: Stress-Strain plot used to determine yield strength for specimen 0.25_AT4

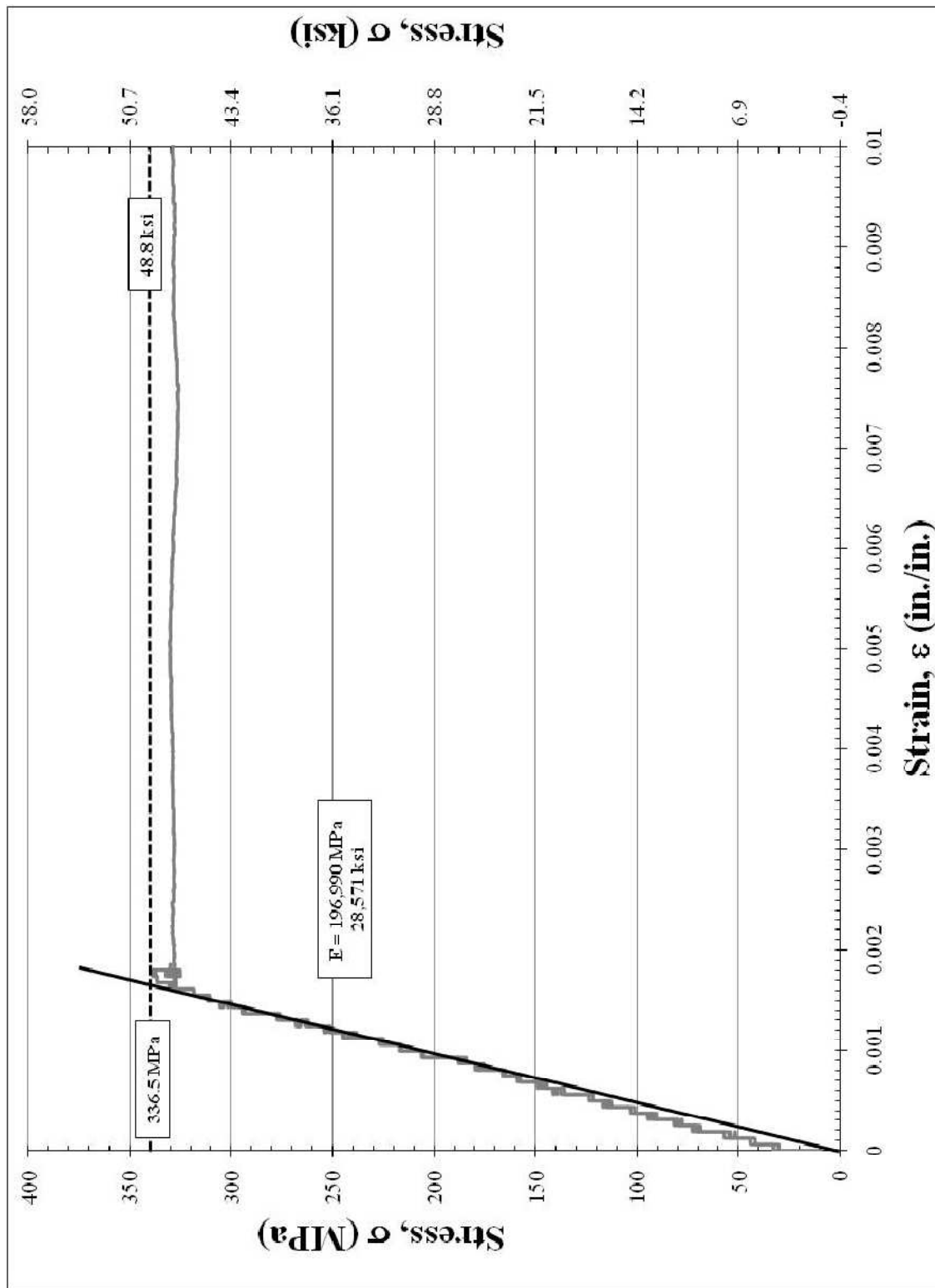


Figure B-9: Stress-Strain plot used to determine yield strength for specimen 0.25 AT5

B.4 COMPLETE STRESS STRAIN DIAGRAMS

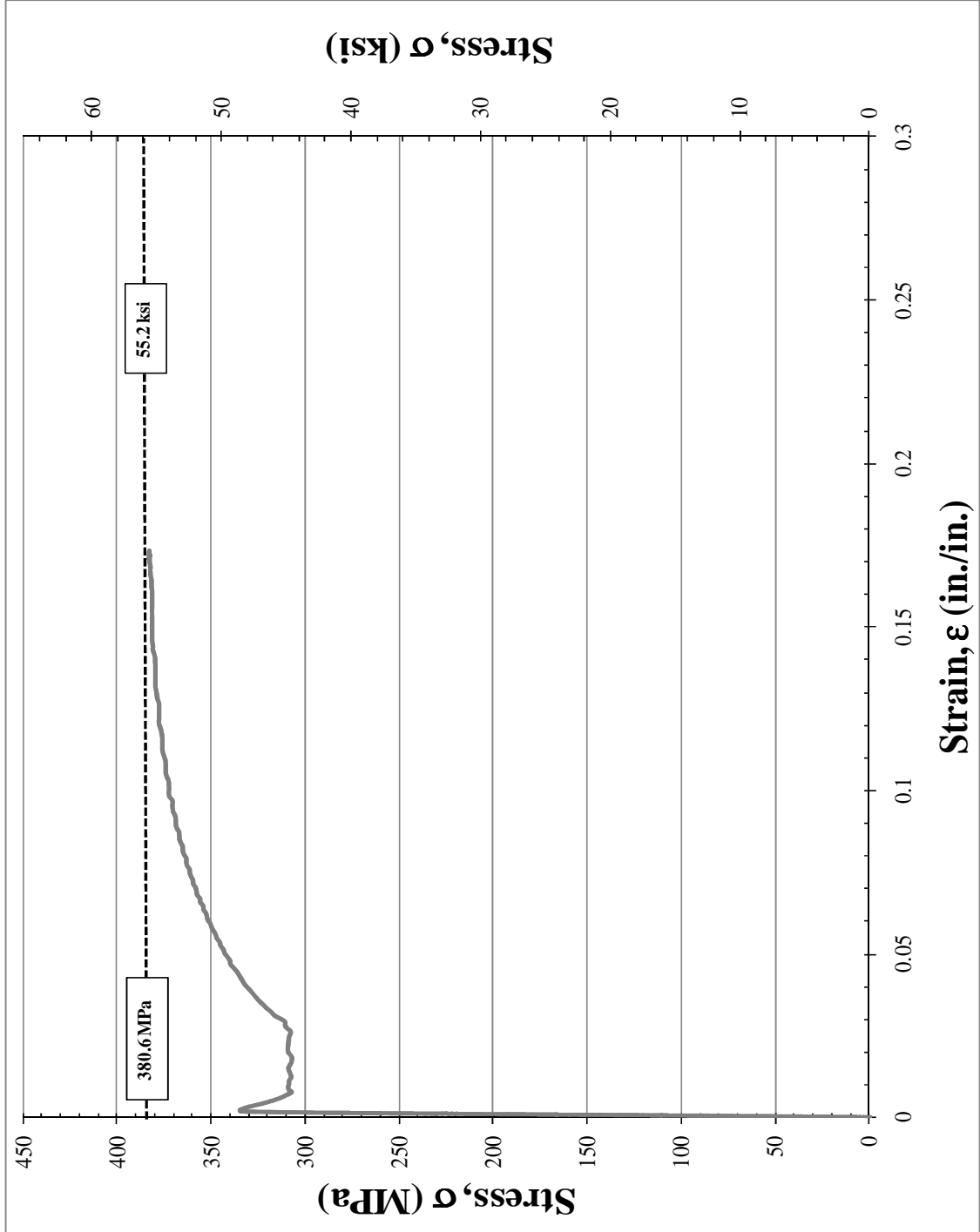


Figure B-10: Stress-Strain plot used to determine ultimate strength for specimen 0.125_AT1

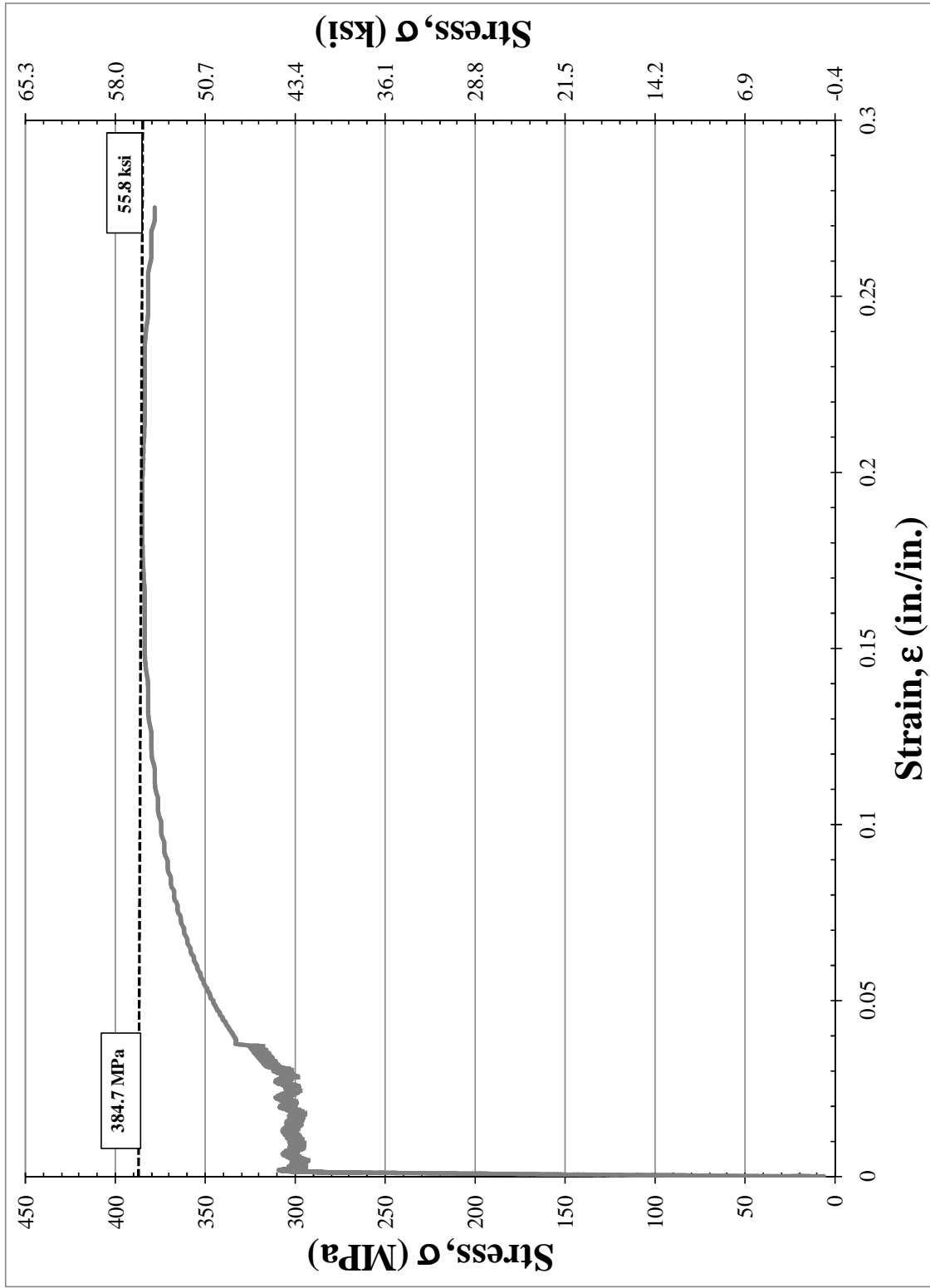


Figure B-11: Stress-Strain plot used to determine ultimate strength for specimen 0.125_AT3

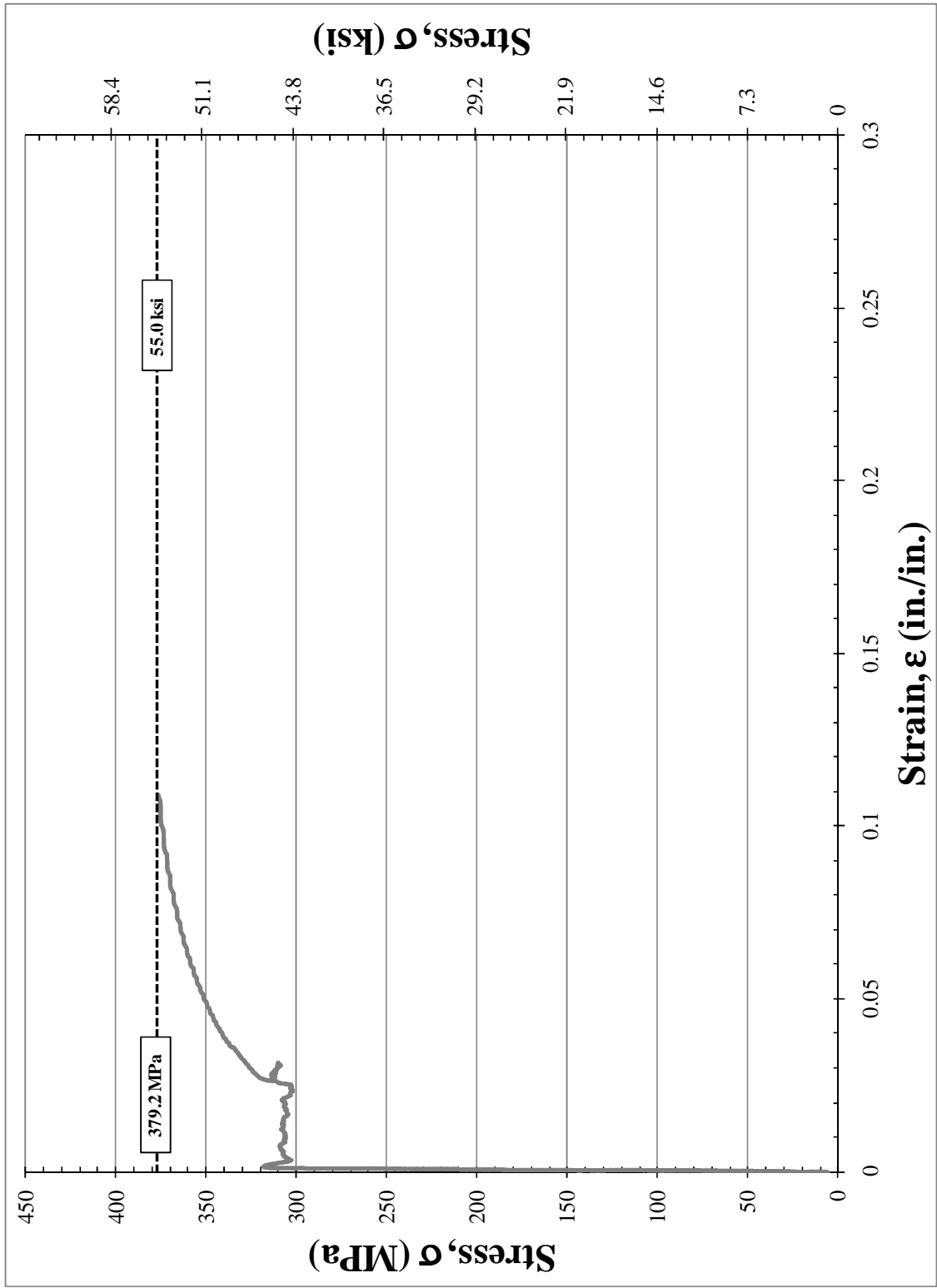


Figure B-12: Stress-Strain plot used to determine ultimate strength for specimen 0.125_AT4

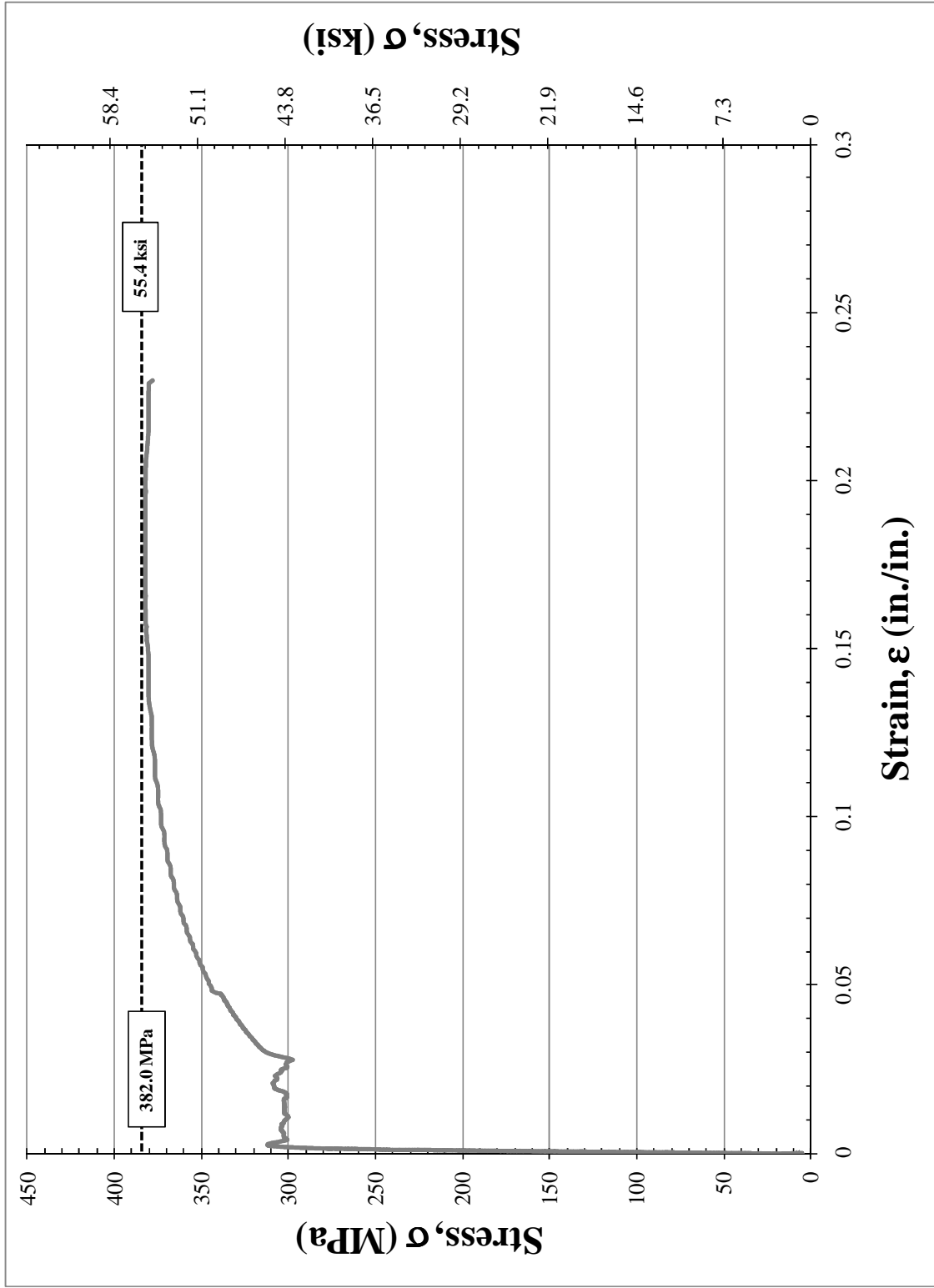


Figure B-13: Stress-Strain plot used to determine ultimate strength for specimen 0.125_AT5

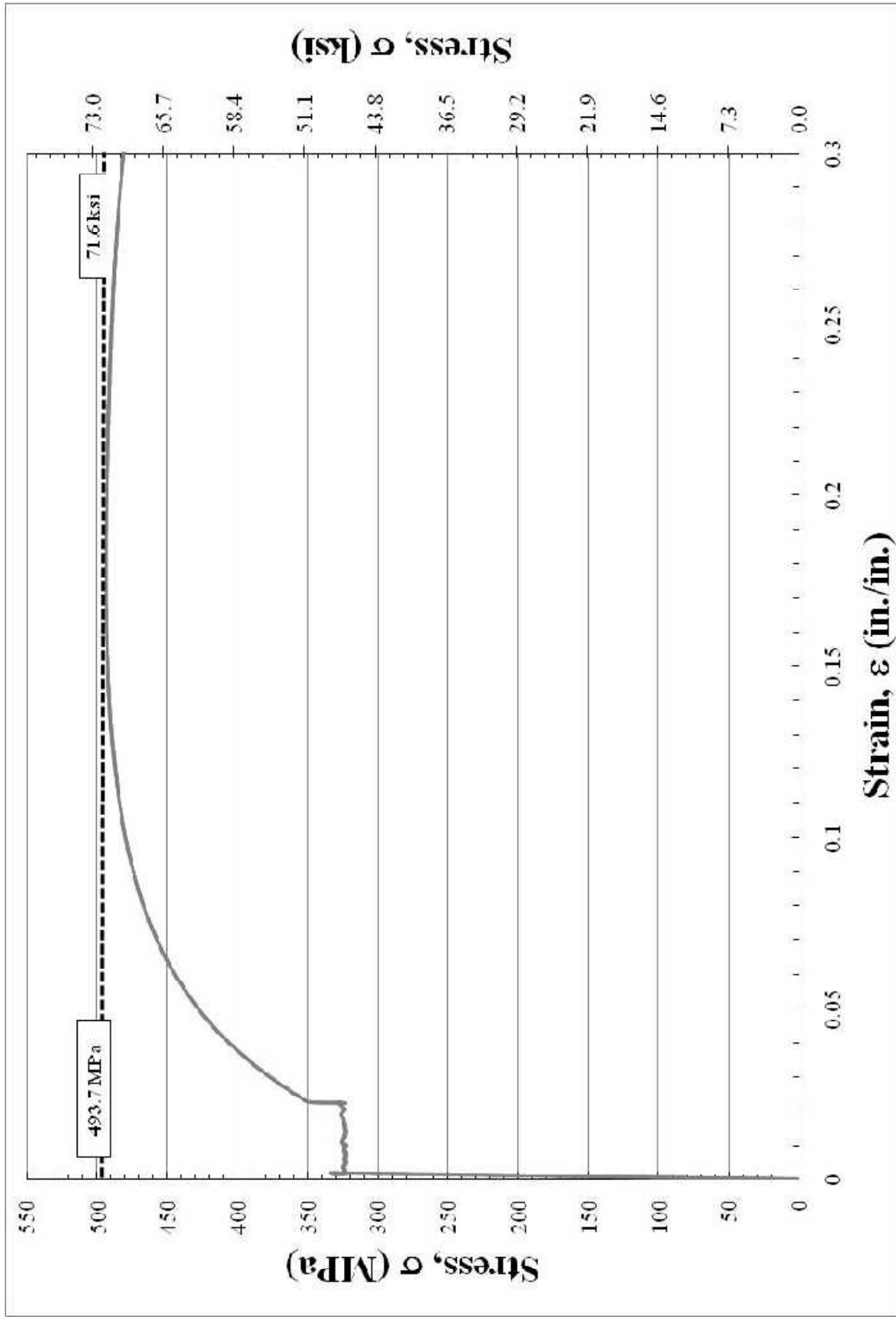


Figure B-14: Stress-Strain plot used to determine ultimate strength for specimen 0.25_AT1

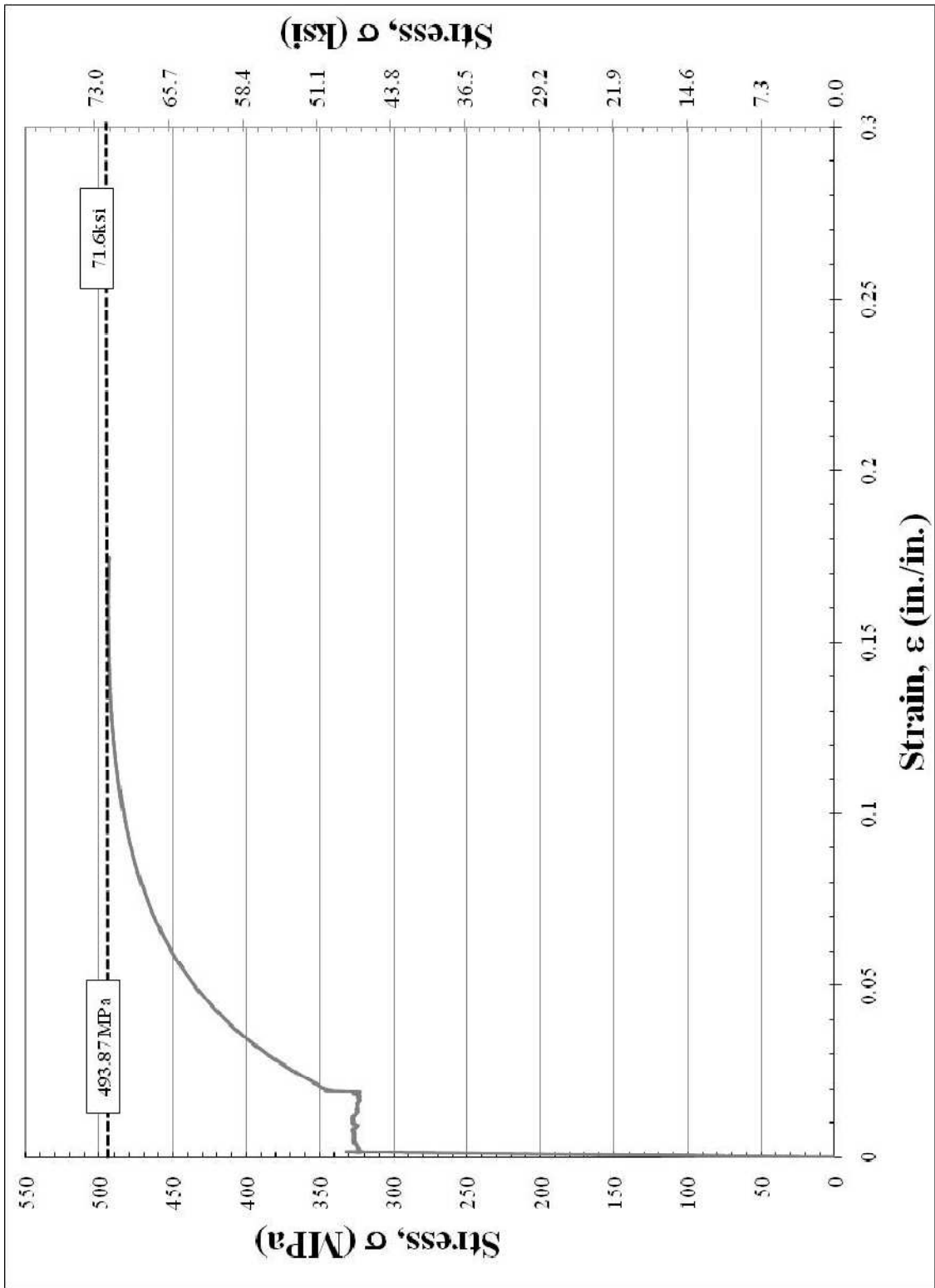


Figure B-15: Stress-Strain plot used to determine ultimate strength for specimen

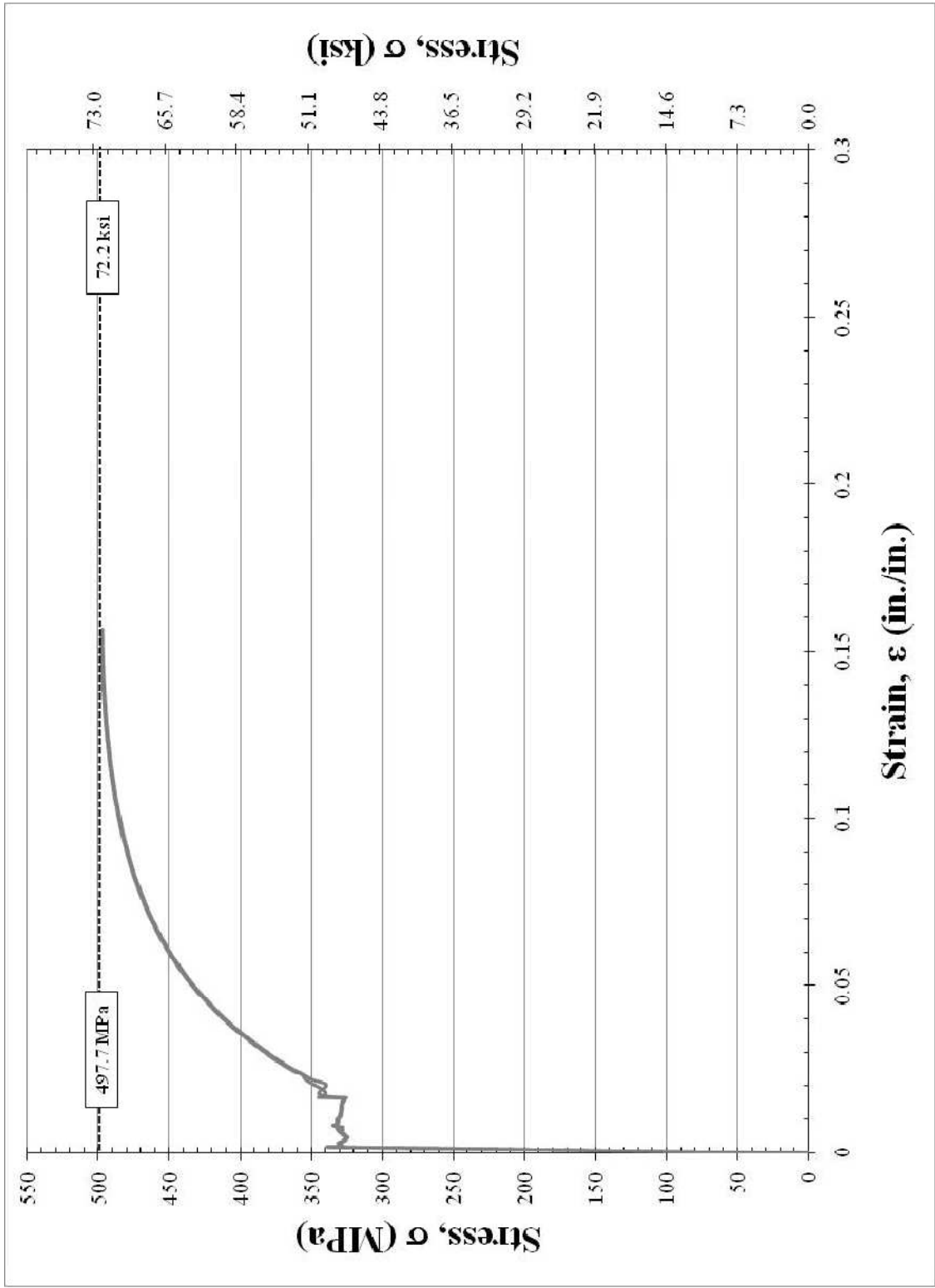


Figure B-16: Stress-Strain plot used to determine ultimate strength for specimen 0.25_AT3

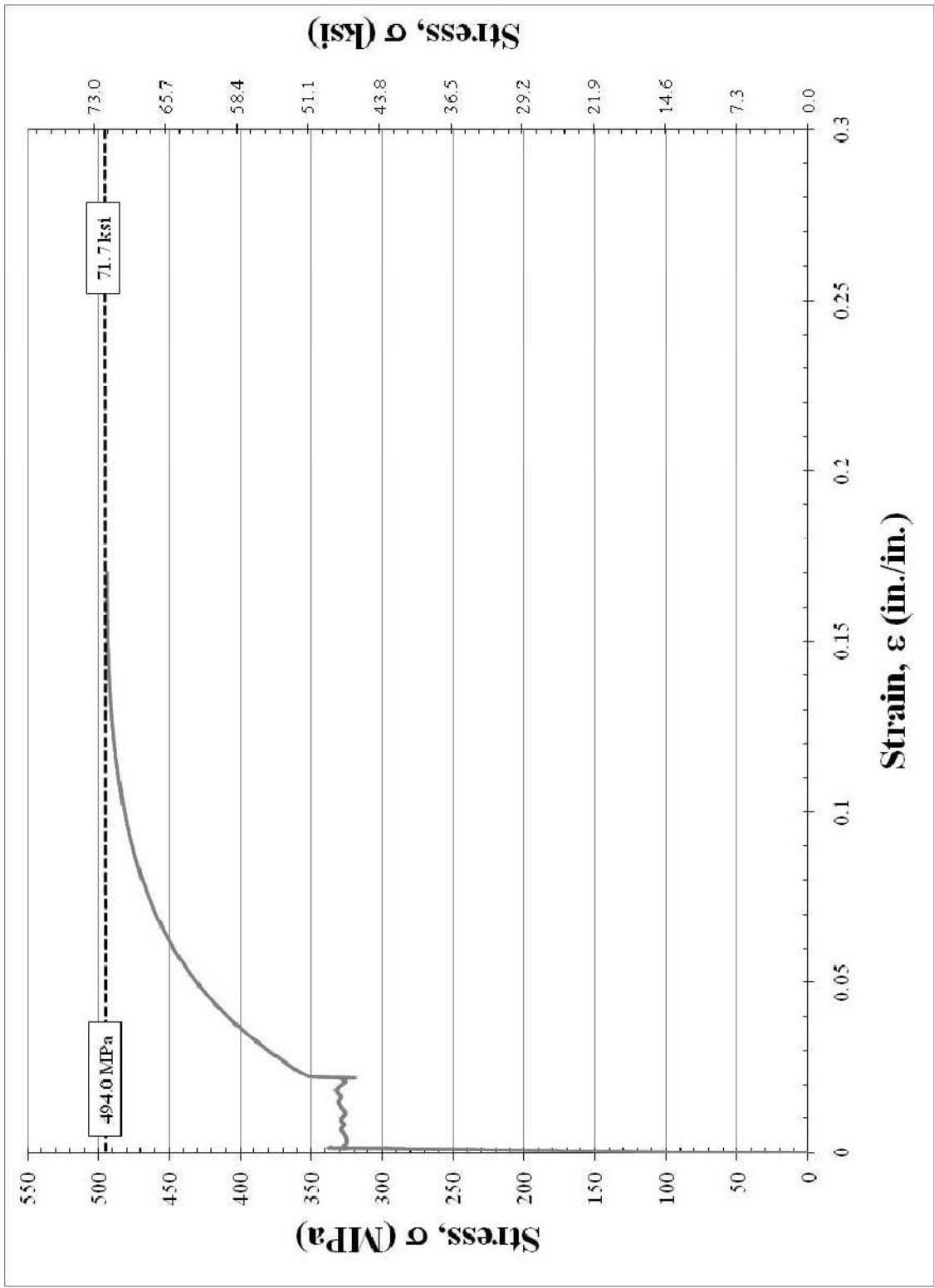


Figure B-17: Stress-Strain plot used to determine ultimate strength for specimen 0.25_AT4

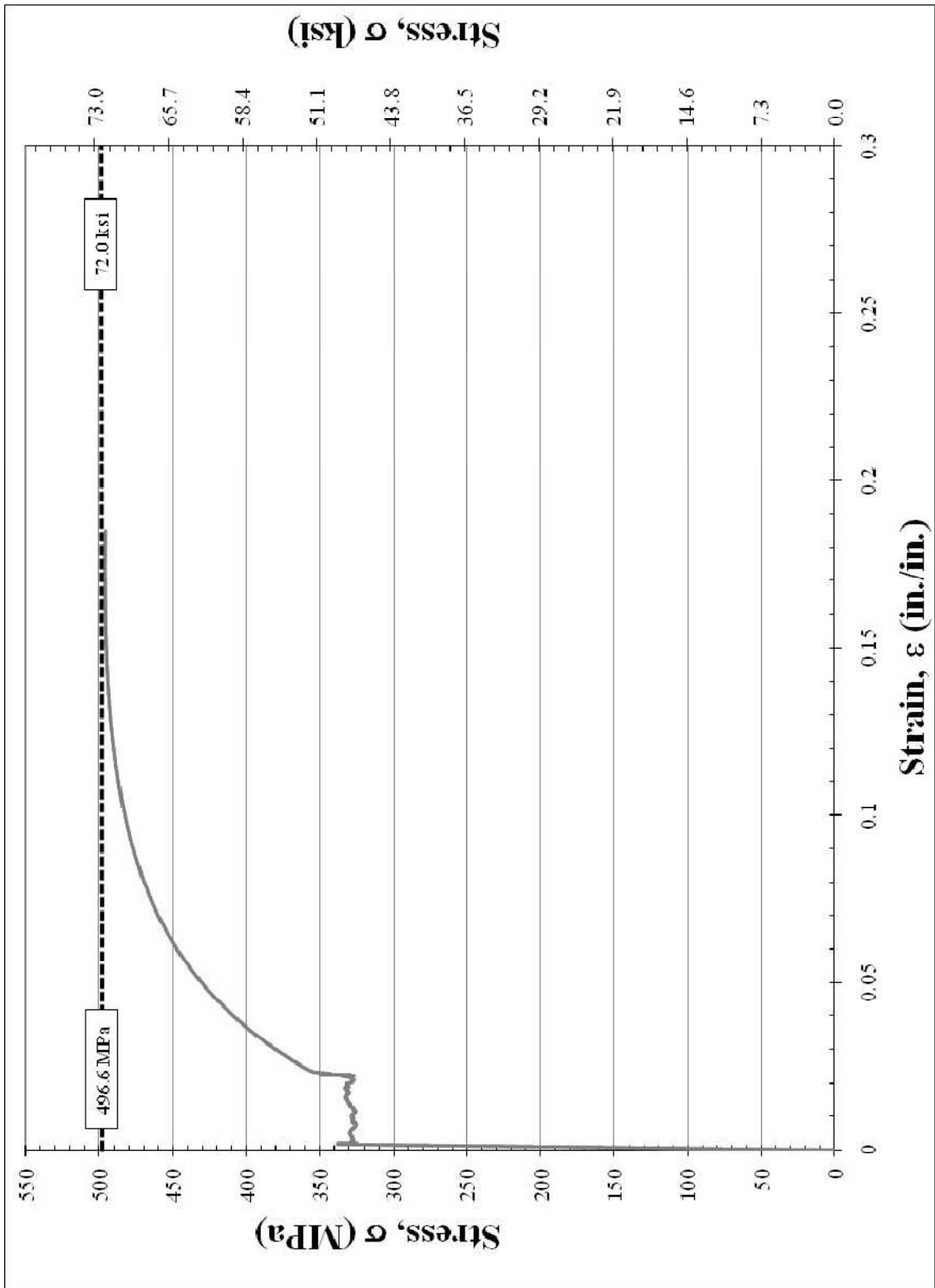


Figure B-18: Stress-Strain plot used to determine ultimate strength for specimen 0.25_AT5

B.5 MODULUS OF ELASTICITY STRESS-STRAIN PLOTS

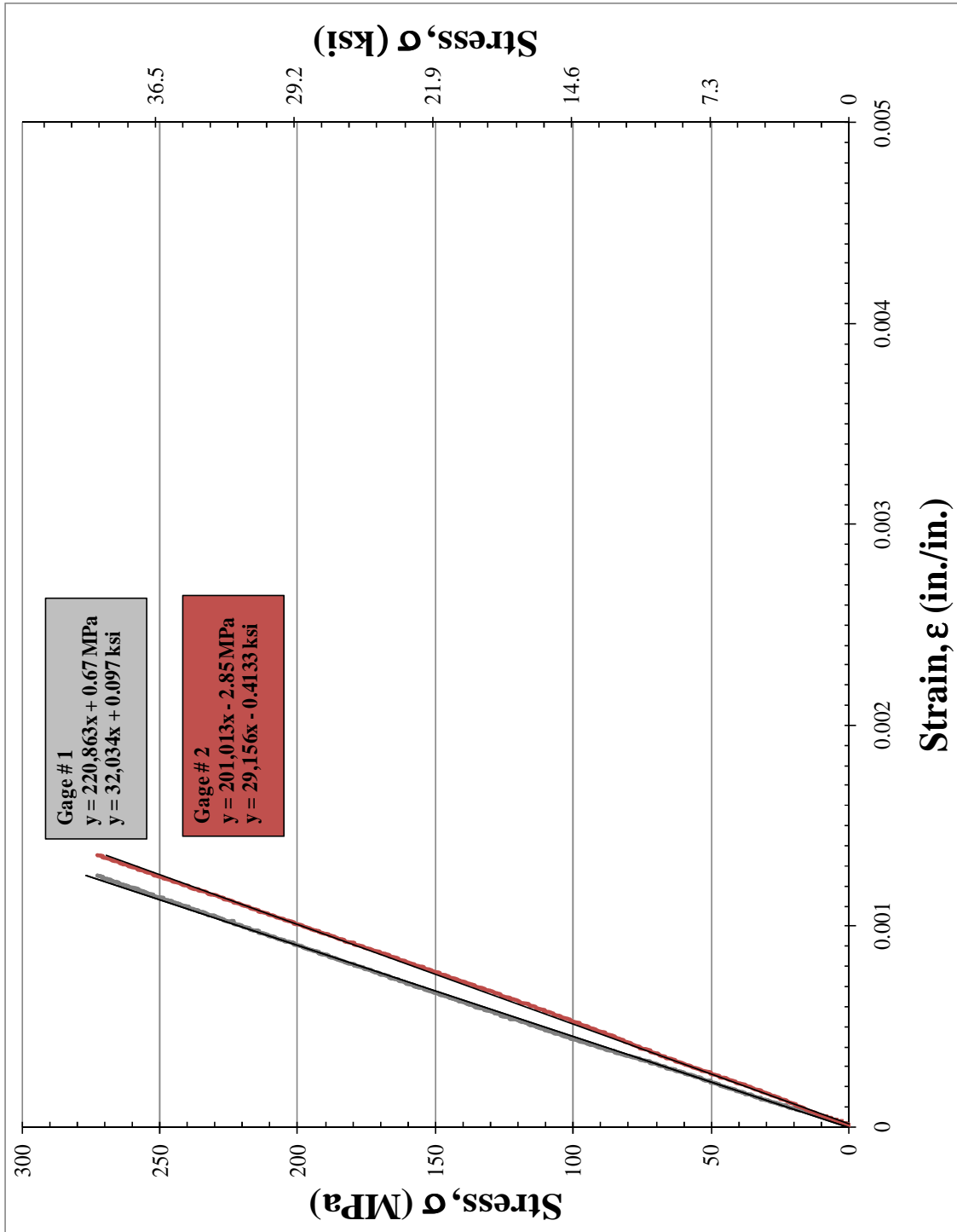


Figure B-19: Strain gage readings used to quantify modulus of elasticity for specimen 0.125_AT1

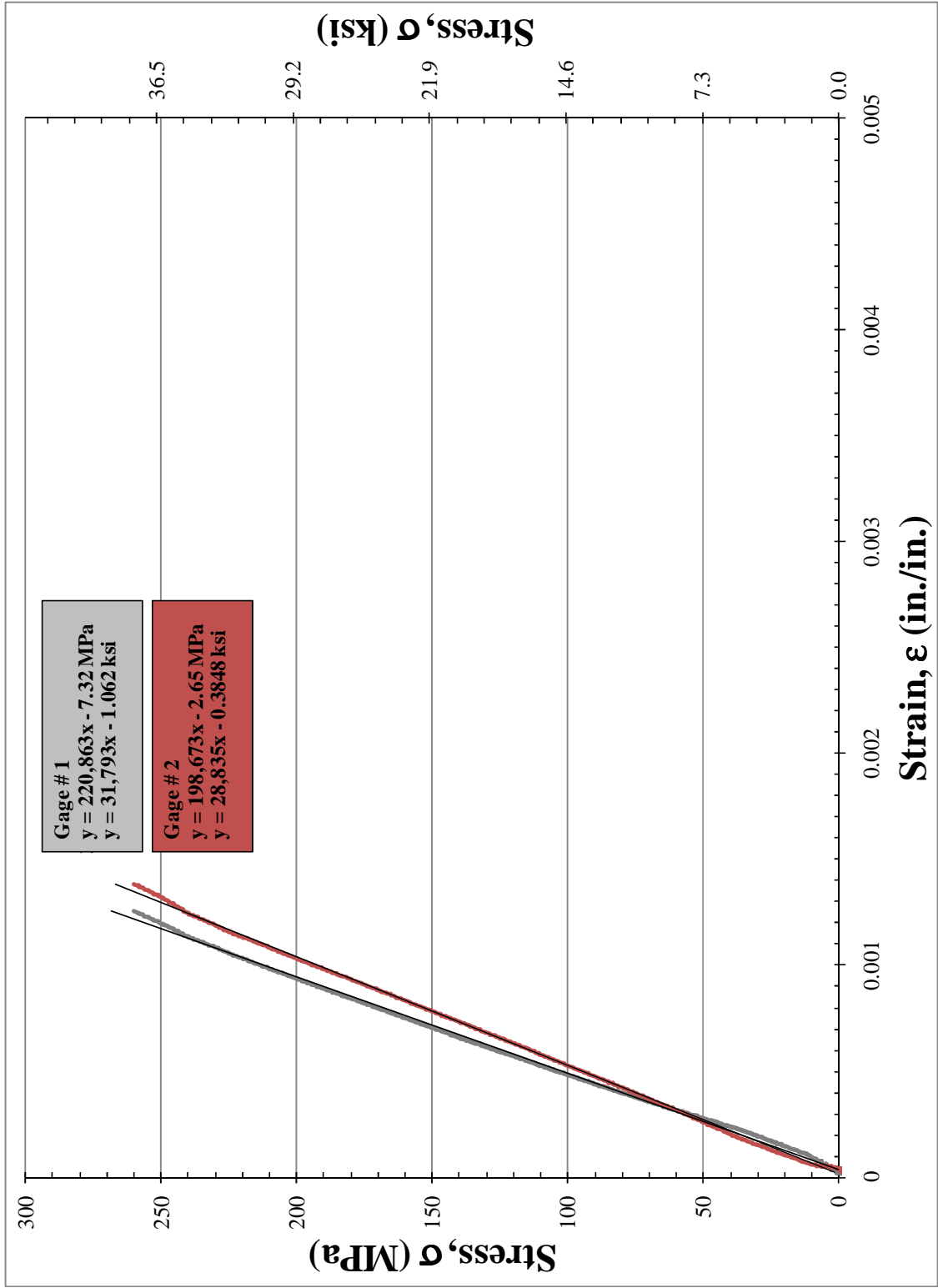


Figure B-20: Strain gage readings used to quantify modulus of elasticity for specimen 0.125_AT3

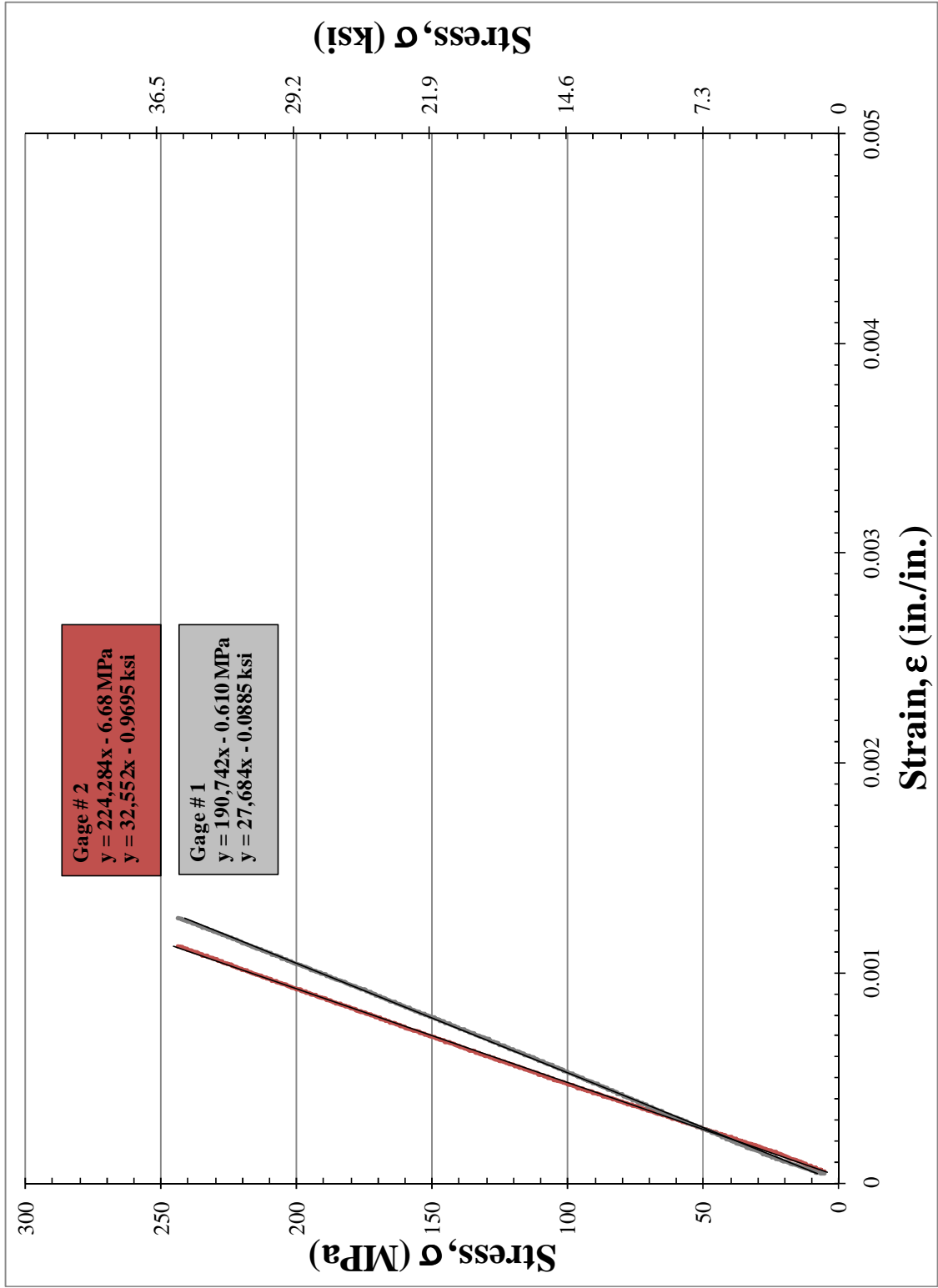


Figure B-21: Strain gage readings used to quantify modulus of elasticity for specimen 0.125_AT4

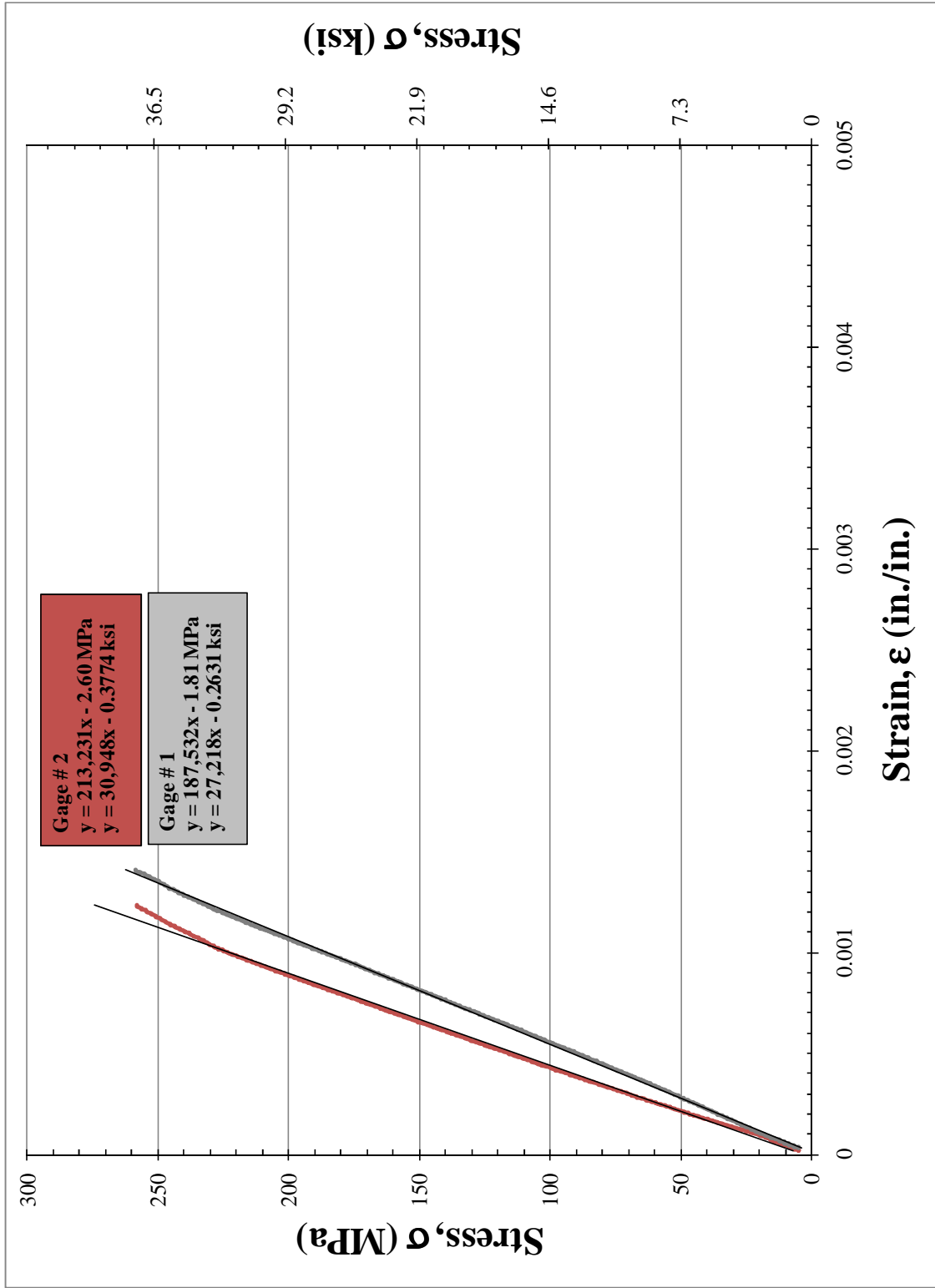


Figure B-22: Strain gage readings used to quantify modulus of elasticity for specimen 0.125_AT5

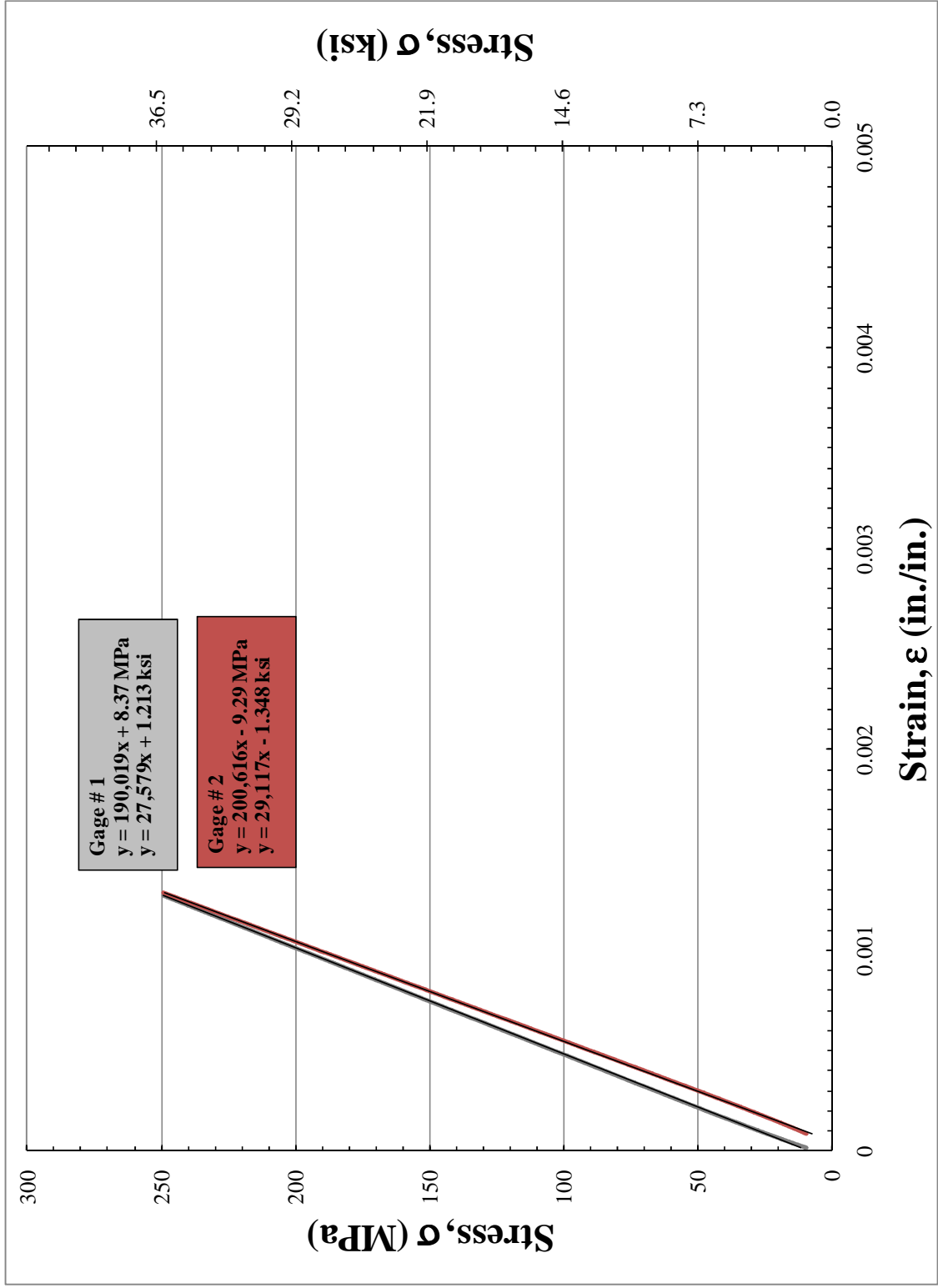


Figure B-23: Strain gage readings used to quantify modulus of elasticity for specimen 0.25_AT1

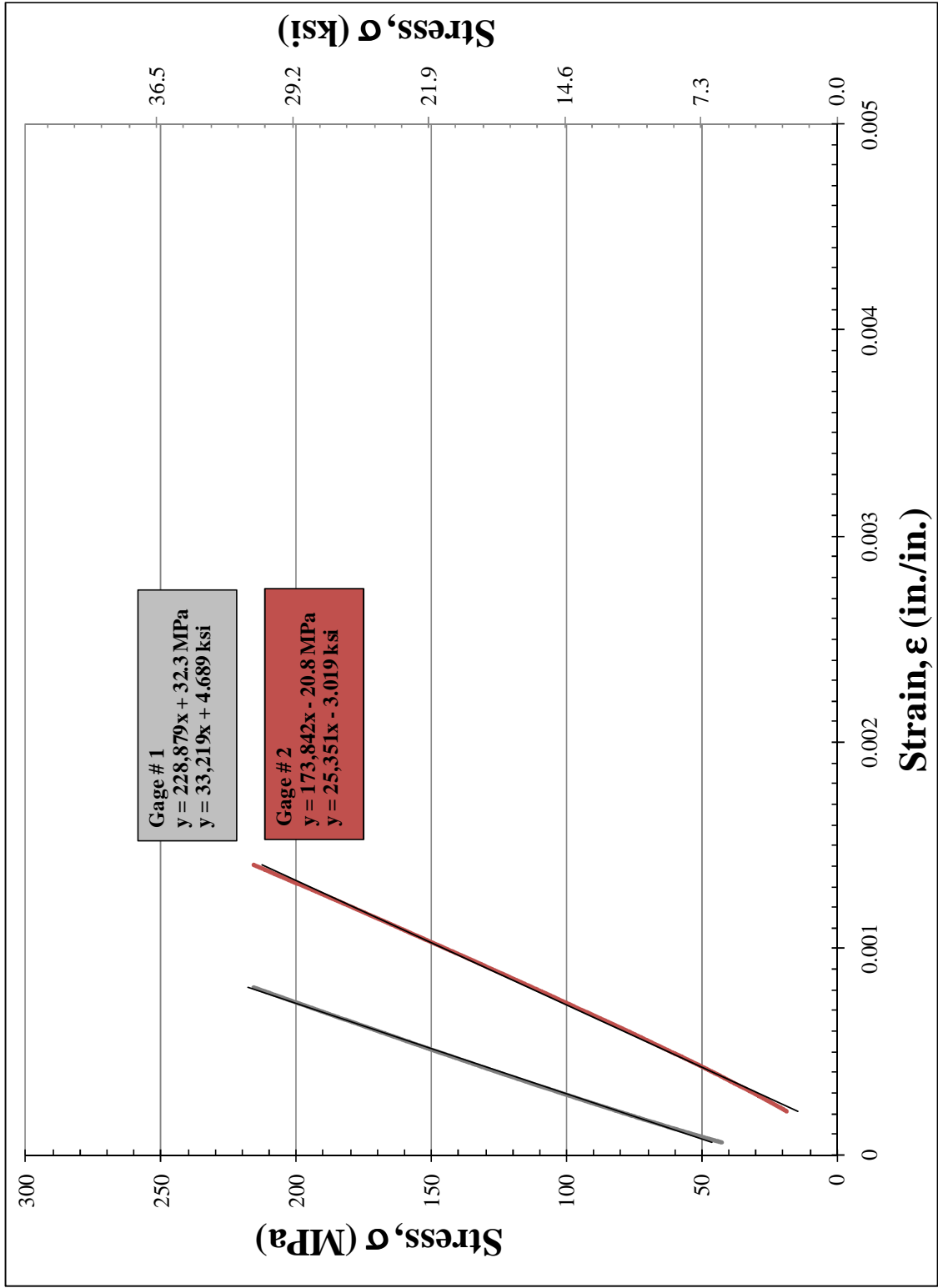


Figure B-24: Strain gage readings used to quantify modulus of elasticity for specimen 0.25_AT2

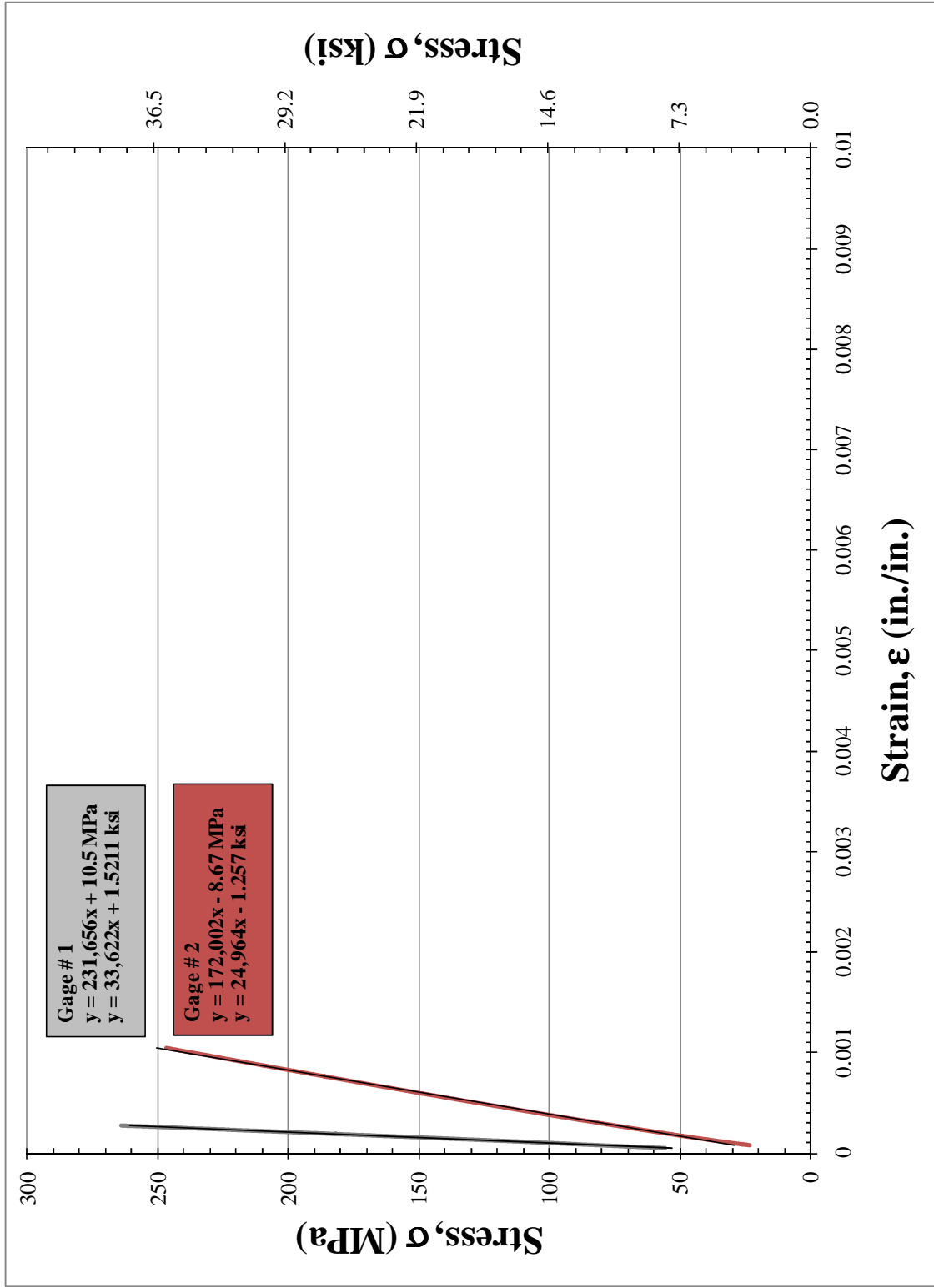


Figure B-25: Strain gage readings used to quantify modulus of elasticity for specimen 0.25_AT3

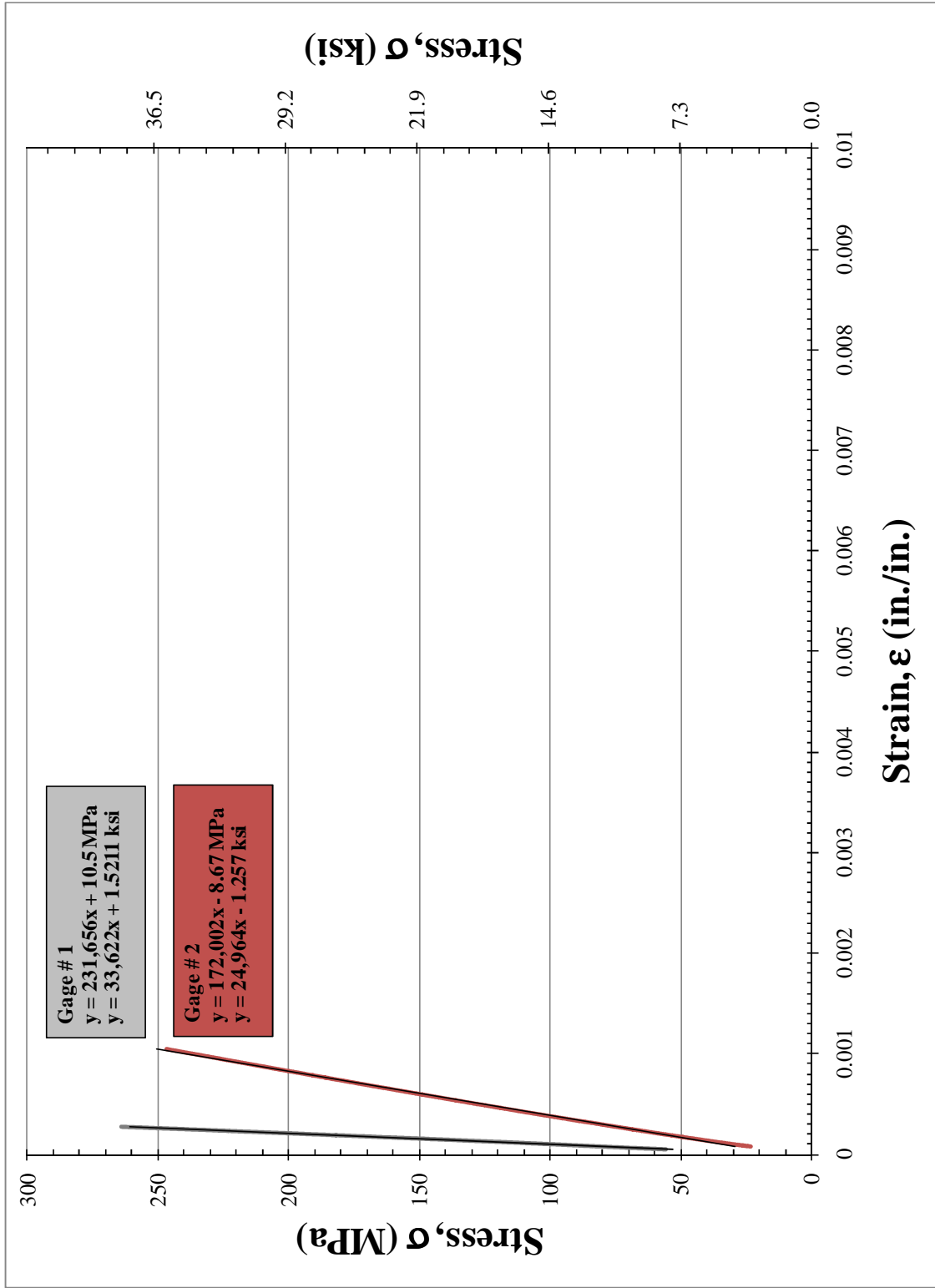


Figure B-26: Strain gage readings used to quantify modulus of elasticity for specimen 0.25_AT4

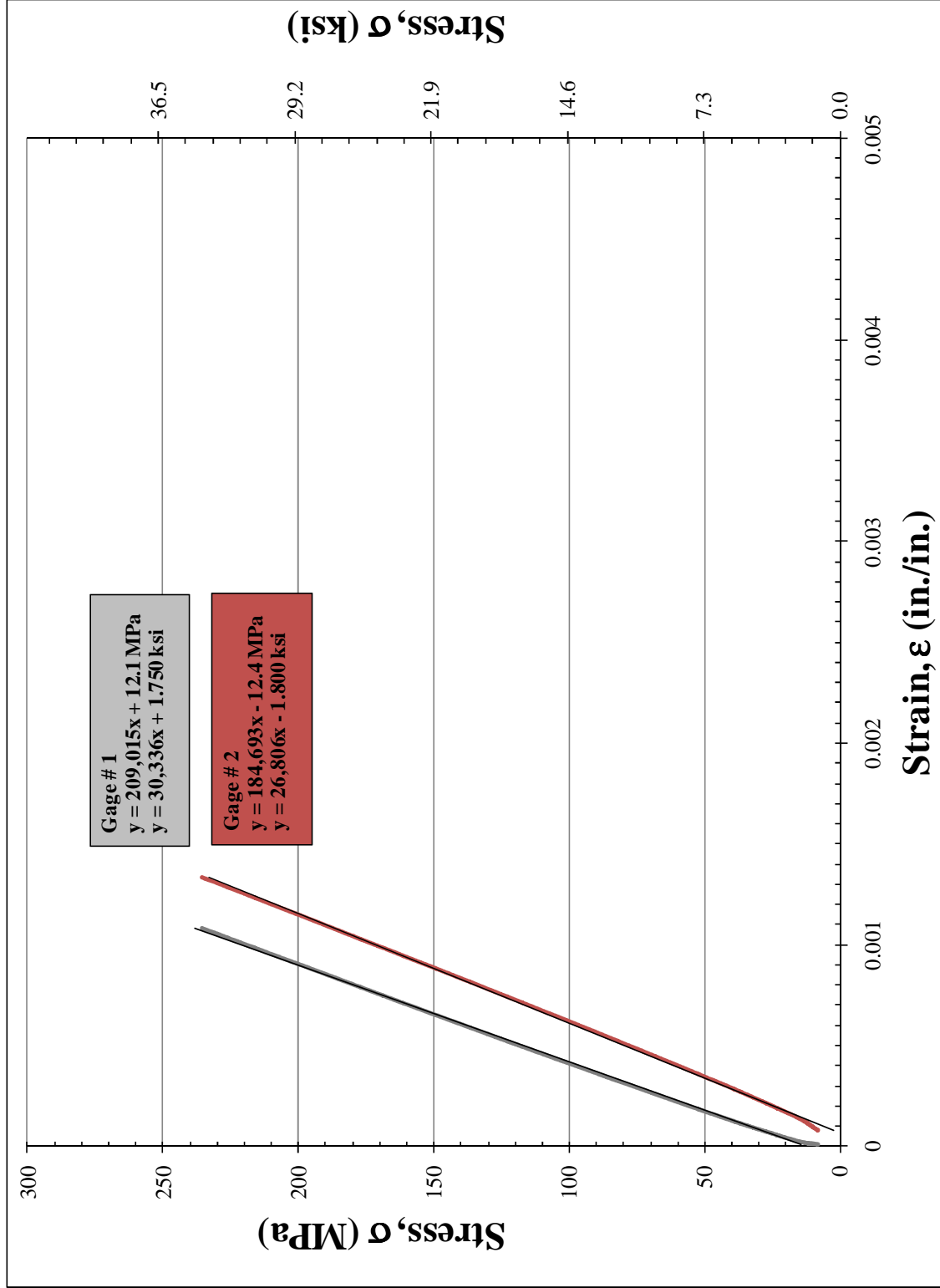


Figure B-27: Strain gage readings used to quantify modulus of elasticity for specimen 0.25_AT5

B.6 TRUE-STRESS TRUE-STRAIN CALCULATION

As a result of the large deformations associated with cold expansion, it was thought that true-stress true-strain material properties should be used for FEM simulations. True-stress and true-strain were calculated from the laboratory results for stress versus strain using the following equations.

$$\text{True Stress} = \sigma_{nom}(1 + \epsilon_{nom}) \quad \text{(B.1)}$$

$$\text{True Strain} = \ln(1 + \epsilon_{nom}) \quad \text{(B.2)}$$

These resulting values for true stress and true strain were used as the material property definitions used in all FEM modeling.

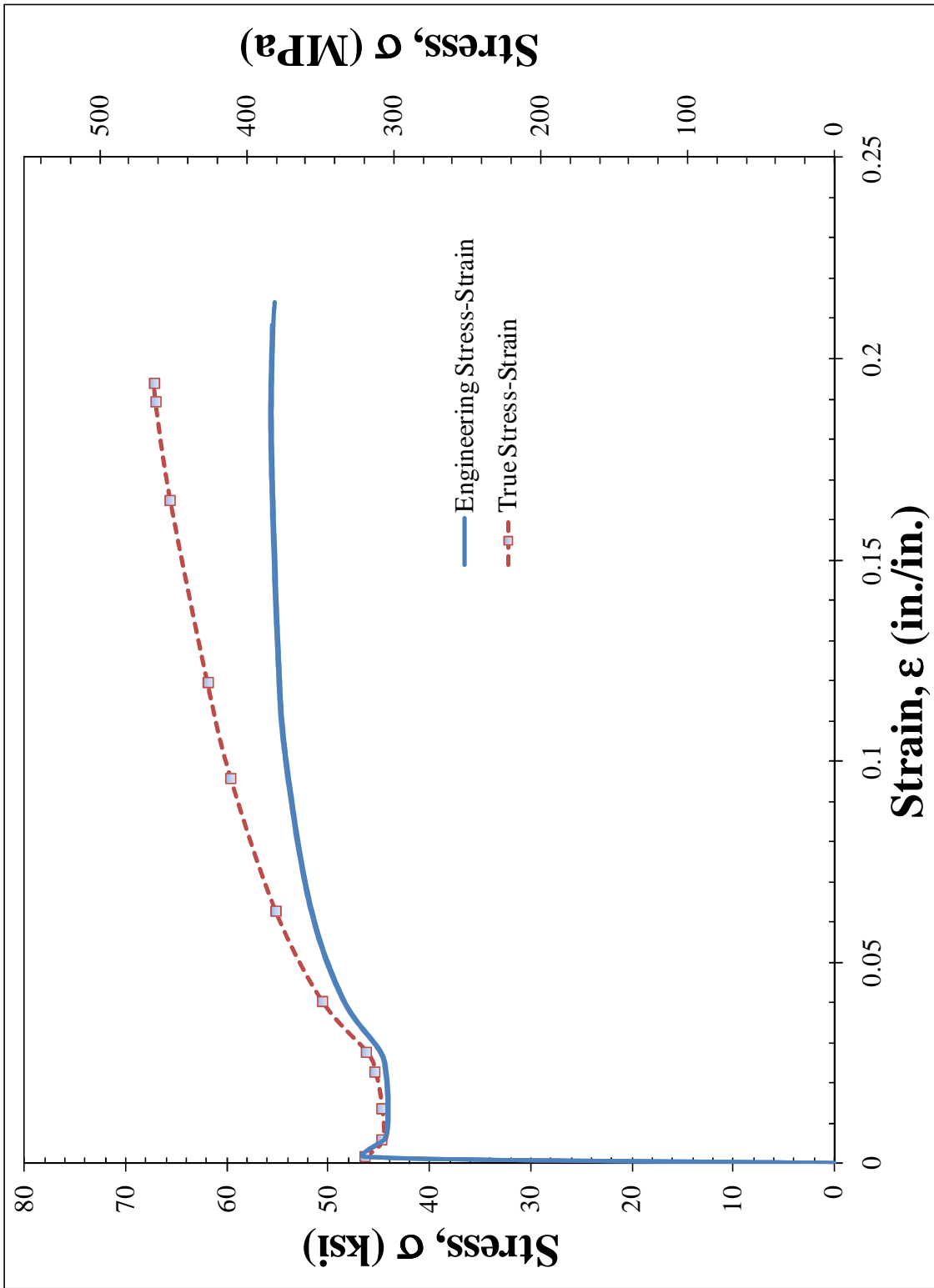


Figure B-28: True stress-strain versus nominal stress strain

APPENDIX C

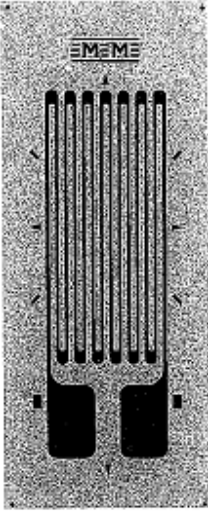
STRAIN GAGE DATA SHEET

250BG

Vishay Micro-Measurements



General Purpose Strain Gages - Linear Pattern

GAGE PATTERN DATA							
			GAGE DESIGNATION See Note 1	RESISTANCE (OHMS) See Note 2	OPTIONS AVAILABLE W, E, L, LE, P E, L*, LE* W* W*		
			EA-XX-250BG-120 ED-DY-250BG-350 WA-XX-250BG-120 WK-XX-250BG-350 EA-XX-250BG-100 EP-XX-250BG-120 SA-XX-250BG-120 SK-XX-250BG-350 SD-DY-250BG-350 WD-DY-250BG-350	120 ± 0.15% 350 ± 0.3% 120 ± 0.3% 350 ± 0.3% 100 ± 0.15% 120 ± 0.15% 120 ± 0.3% 350 ± 0.3% 350 ± 0.6% 350 ± 0.6%			
DESCRIPTION Widely used general-purpose gage. Compact geometry. See also 250UN pattern.							
GAGE DIMENSIONS							
Legend: ES = Each Section CP = Complete Pattern S = Section (S1 = Sec 1) M = Matrix							
<table border="1" style="display: inline-table; border-collapse: collapse;"> <tr> <td style="padding: 2px;">inch</td> </tr> <tr> <td style="padding: 2px;">millimeter</td> </tr> </table>						inch	millimeter
inch							
millimeter							
Gage Length	Overall Length	Grid Width	Overall Width	Matrix Length	Matrix Width		
0.250	0.375	0.125	0.125	0.52	0.22		
6.35	9.53	3.18	3.18	13.2	5.6		

GAGE SERIES DATA			
See Gage Series data sheet for complete specifications.			
Series	Description	Strain Range	Temperature Range
EA	Constantan foil in combination with a tough, flexible, polyimide backing.	±3%	-100° to +350°F [-75° to +175°C]
ED	Isoelastic foil in combination with tough, flexible polyimide film.	±2%	-320° to +400°F [-195° to +205°C]
WA	Fully encapsulated constantan gages with high endurance leadwires.	±2%	-100° to +400°F [-75° to +205°C]
WK	Fully encapsulated K-alloy gages with high-endurance leadwires.	±1.5%	-452° to +550°F [-269° to +230°C]
EP	Annealed constantan foil with tough, high-elongation polyimide backing.	±20%	-100° to +400°F [-75° to +205°C]
SA	Fully encapsulated constantan gages with solder dots.	±2%	-100° to +400°F [-75° to +205°C]
SK	Fully encapsulated K-alloy gages with solder dots.	±1.5%	-452° to +450°F [-269° to +230°C]
SD	Equivalent to WD Series, but with solder dots instead of leadwires.	±1.5%	-320° to +400°F [-195° to +205°C]
WD	Fully encapsulated isoelastic gages with high-endurance leadwires.	±1.5%	-320° to +500°F [-195° to +260°C]

Note 1: Insert desired S-T-C number in spaces marked XX.

Note 2: Tolerance is increased when Option W, E, SE, LE, or P is specified.

*Options available but not normally recommended. See Optional Features data sheet for details.

APPENDIX D

CRACKED FATIGUE SPECIMENS

As mentioned in Sections 3.4 and 4.1.1, failure of the axial fatigue test program was defined as the visual confirmation of cracks formed at a hole's edges. The following section provides photographs and flaw sizes at failure for each successfully cracked specimen.

D.1 SPECIMEN CONTROL_9

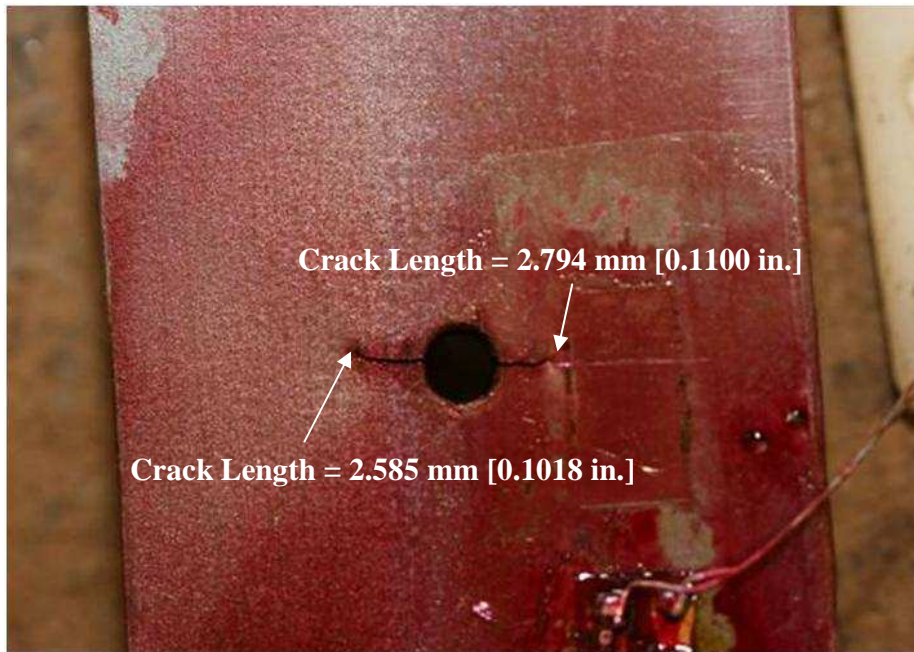


Figure D-1: Cracked specimen *Control_9* side 1, failed at 234,824 cycles

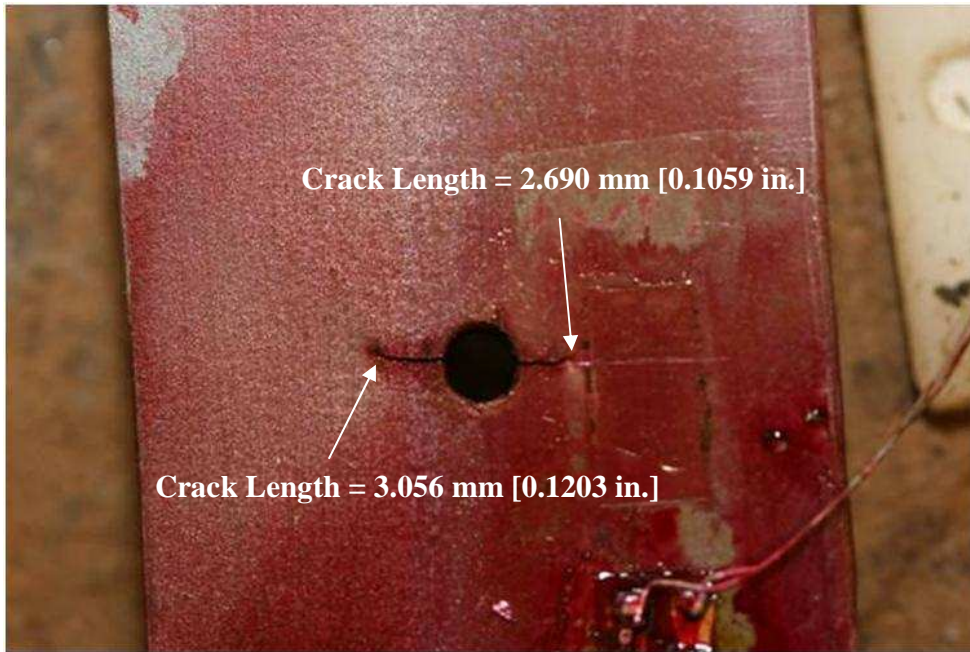


Figure D-2: Cracked specimen *Control_9* side 1, failed at 234,824 cycles

D.2 SPECIMEN CONTROL_10

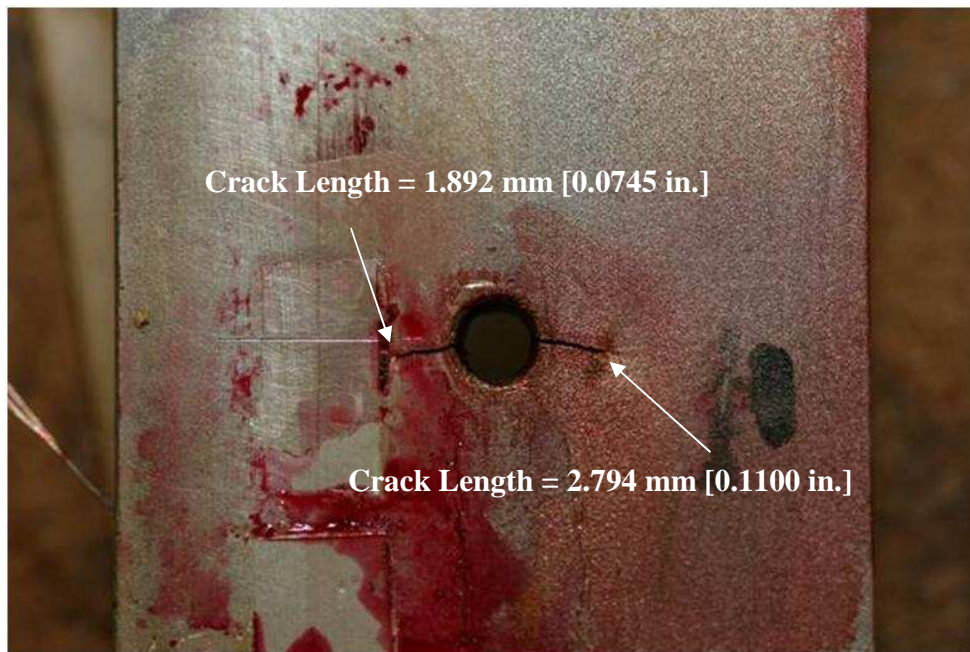


Figure D-3: Cracked specimen *Control_10* side 1, failed at 177,106 cycles

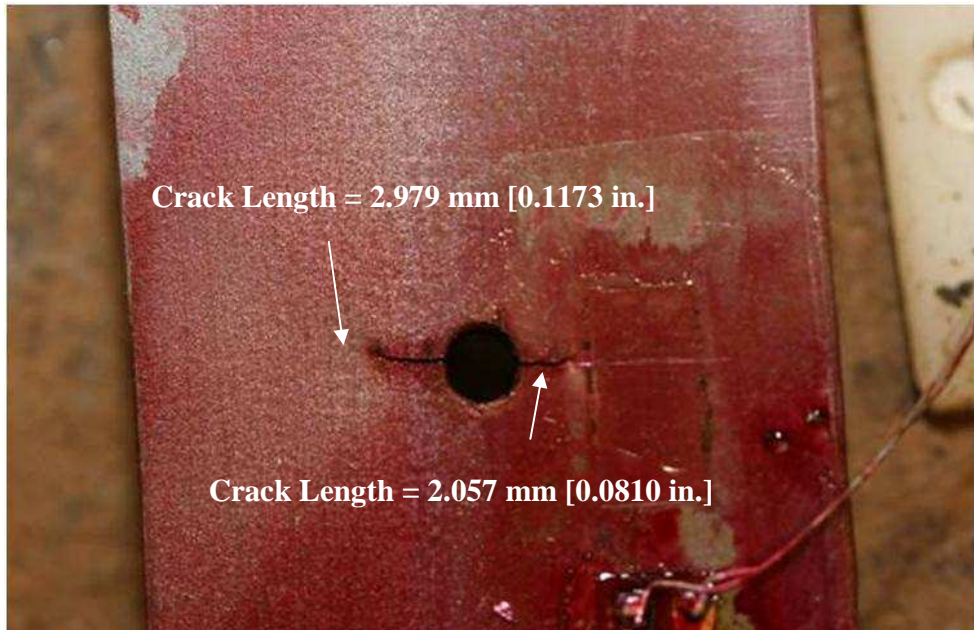


Figure D-4: Cracked specimen *Control_10* side 2, failed at 177,106 cycles

D.3 SPECIMEN CONTROL_11

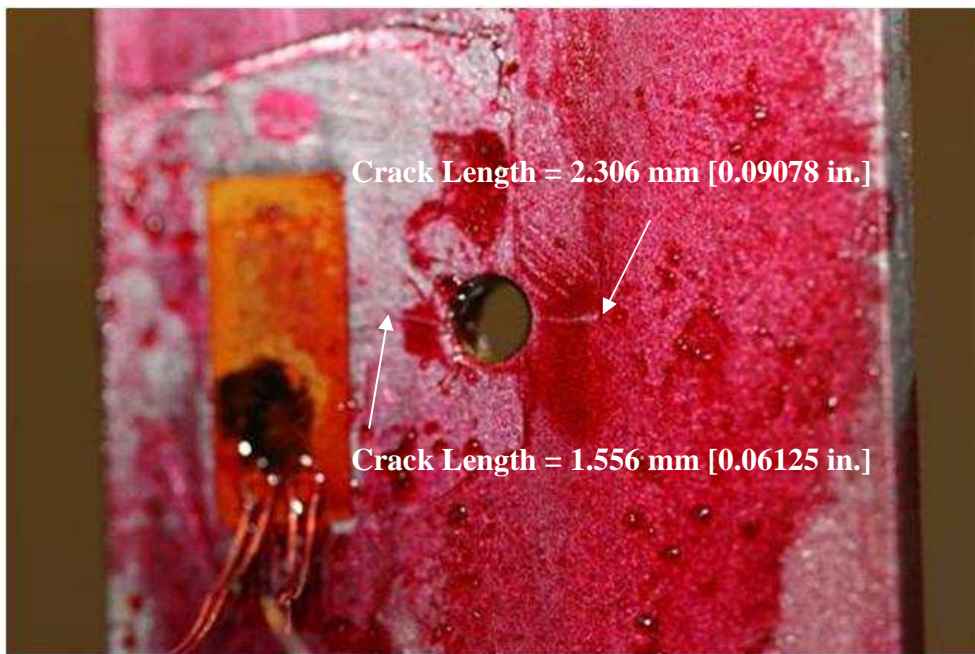


Figure D-5: Cracked specimen *Control_11* side 1, failed at 169,222 cycles

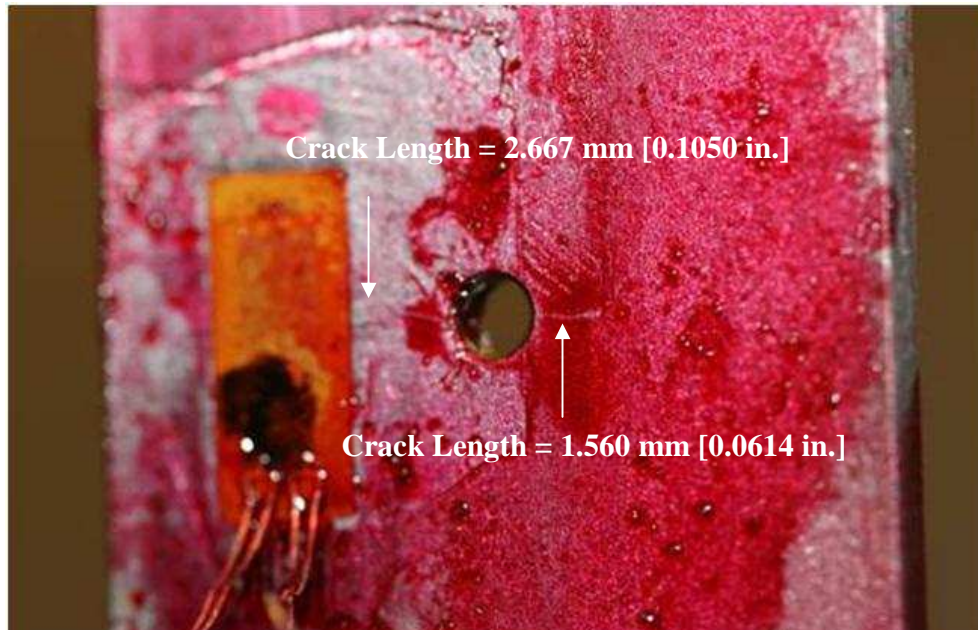


Figure D-6: Cracked specimen *Control_11* side 2, failed at 169,222 cycles

D.1 SPECIMEN CONTROL_12



Figure D-7: Cracked specimen *Control_12* side 1, failed at 195,220 cycles

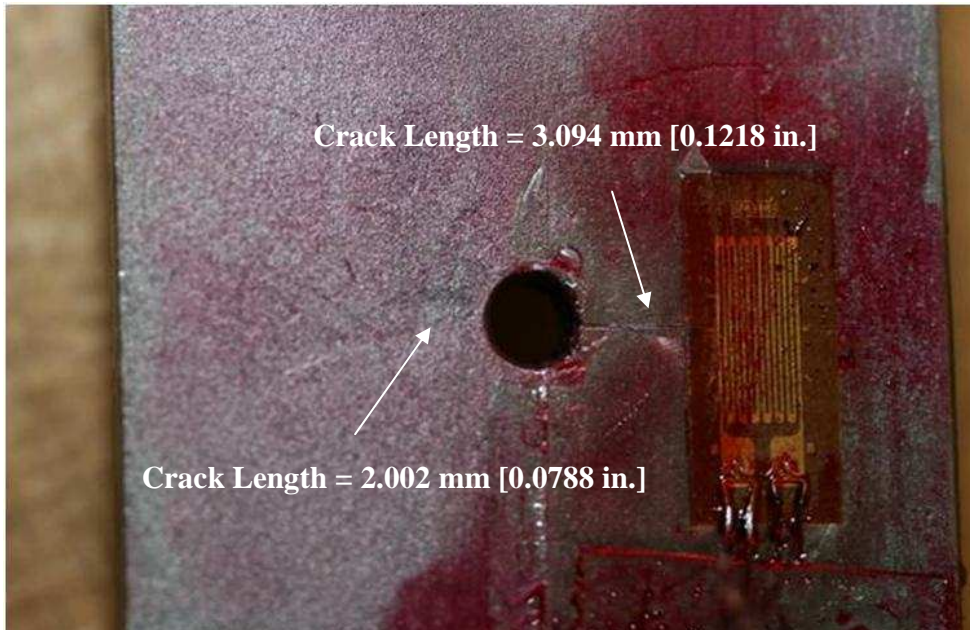


Figure D-8: Cracked specimen *Control_12* side 2, failed at 195,220 cycles

D.2 SPECIMEN CONTROL_13

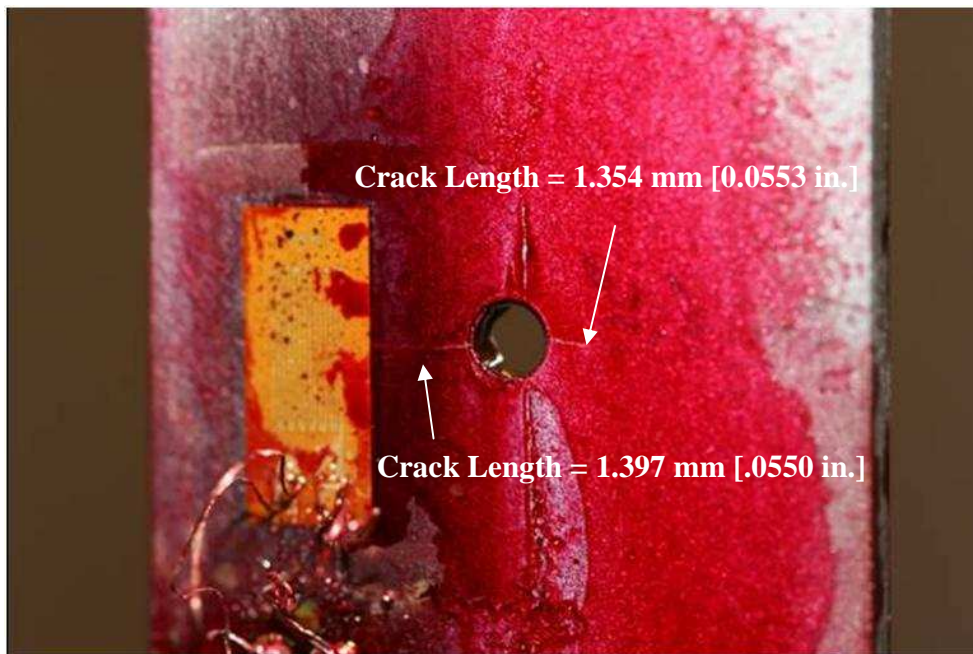


Figure D-9: Cracked specimen *Control_13* side 1, failed at 194,449 cycles

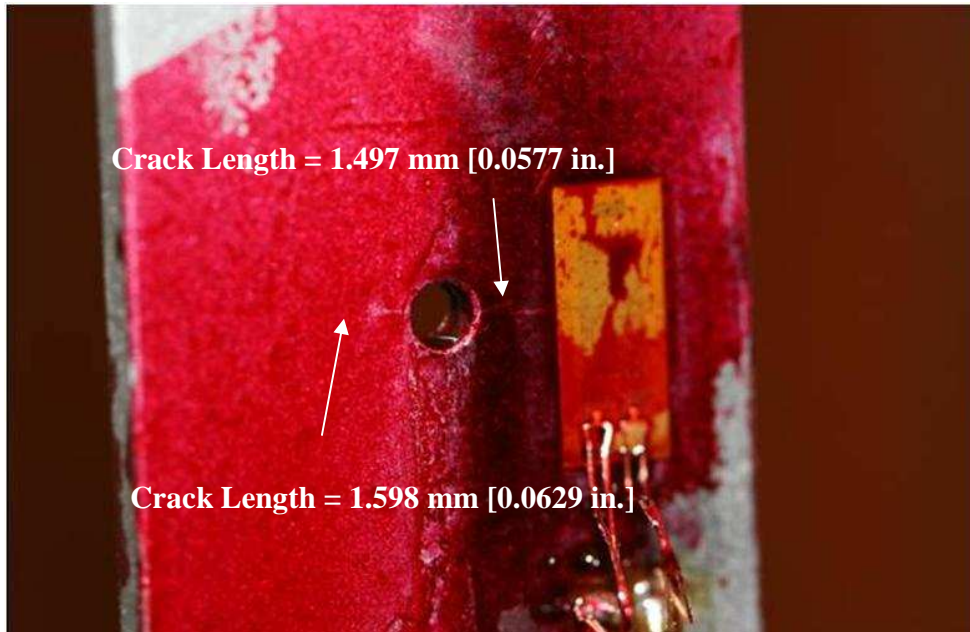


Figure D-10: Cracked specimen *Control_13* side 2, failed at 194,449 cycles

D.3 SPECIMEN CONTROL_14

Specimen not photographed.

D.4 SPECIMEN CONTROL_15

Specimen did not fail.

D.5 SPECIMEN CONTROL_16

Specimen did not fail.

D.6 SPECIMEN PICK 3

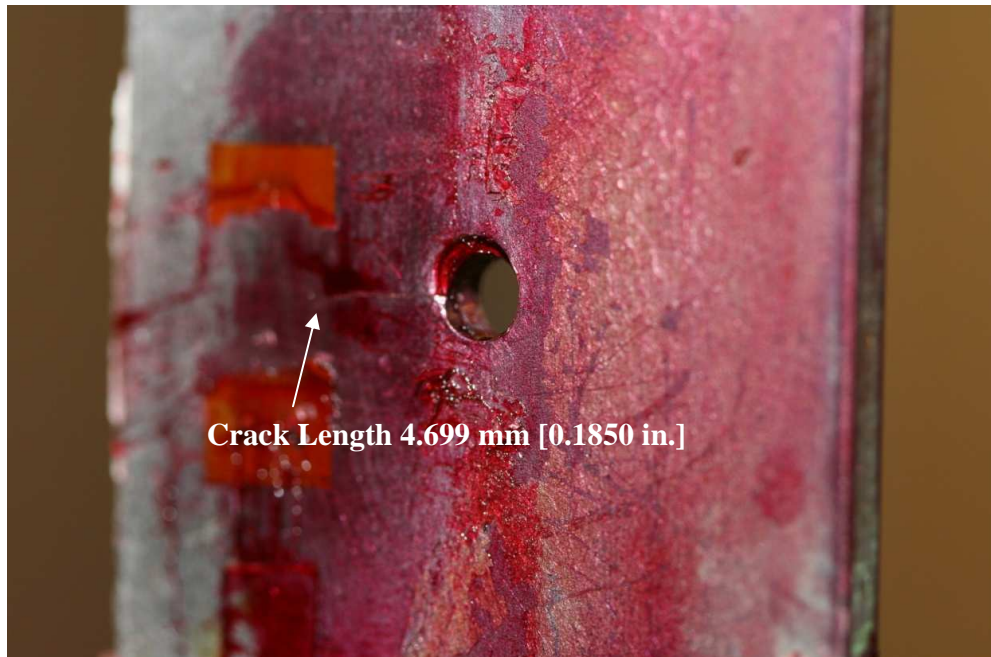


Figure D-11: Cracked specimen *PICK 3* side 1, failed at 818,635 cycles



Figure D-12: Cracked specimen *PICK 3* side 2, failed at 818,635 cycles

D.7 SPECIMEN PICK 4

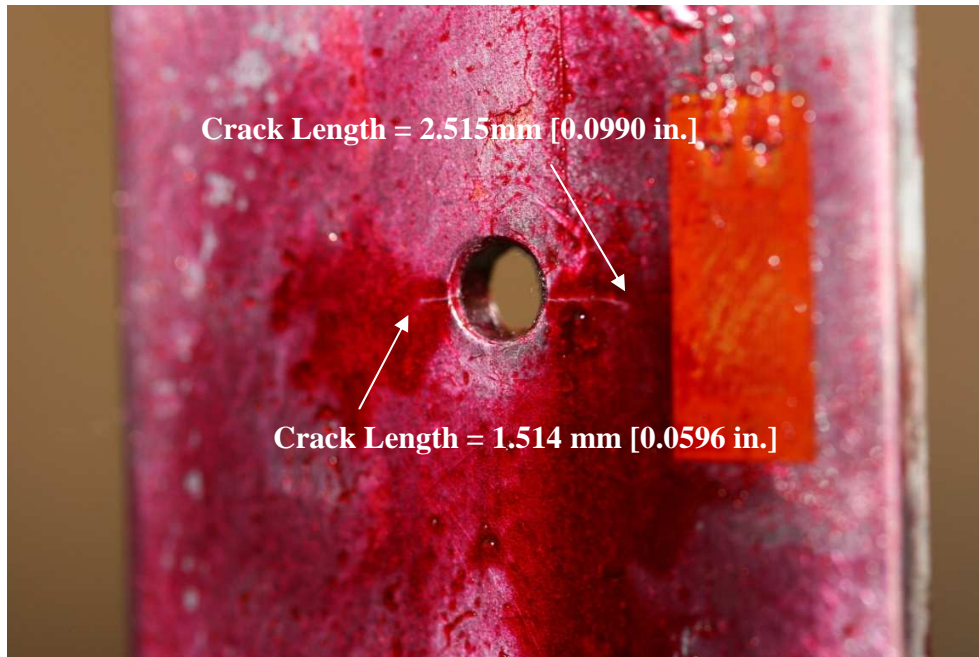


Figure D-13: Cracked specimen *PICK 4* side 1, failed at 743,725 cycles



Figure D-14: Cracked specimen *PICK 4* side 2, failed at 743,725 cycles

D.8 SPECIMEN PICK 6

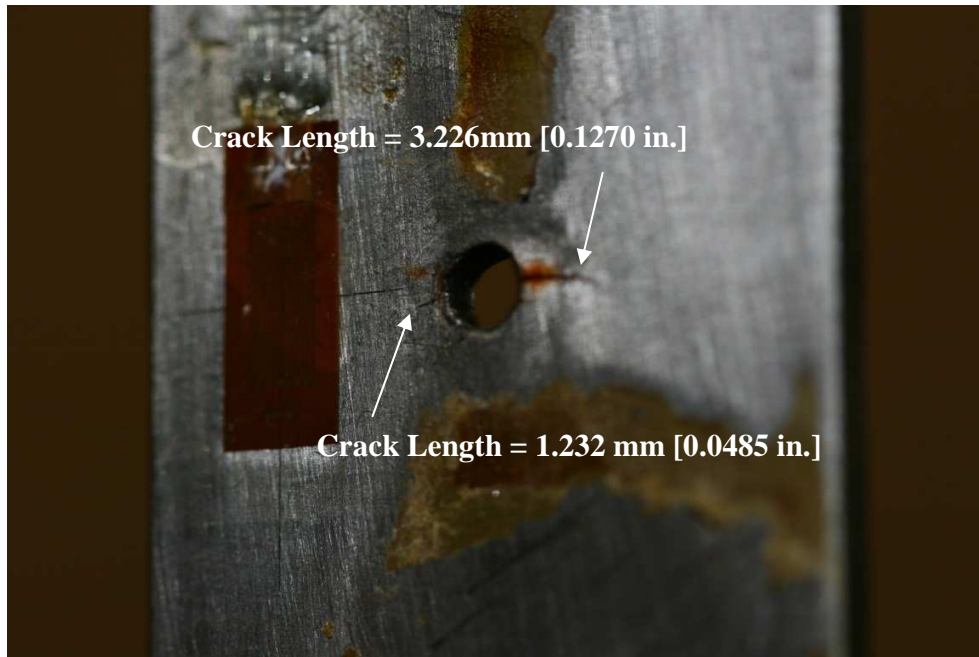


Figure D-15: Cracked specimen *PICK 6* side 1, failed at 426,302 cycles



Figure D-16: Cracked specimen *PICK 6* side 2, failed at 426,302 cycles

REFERENCES

1. Lindberg, A.Y. and Schultz, A.E. (2007). Incorporation of Fatigue Detail Classification of Steel Bridges into the Minnesota Department of Transportation Database: Final Report. St. Paul, Minnesota Department of Transportation Research Services Section.
2. Vulić, N., Jecić, S., and Grubišić, V. (1997). "Validation of crack arrest technique by numerical modeling." *International Journal of Fatigue*, 19(4), 283-291.
3. Domazet, Z. (1996). "Comparison of fatigue crack retardation methods." *Engineering Failure Analysis*, 3(2), 137-147.
4. Amrouche, A., Ghfiri, R., Imad, A., & Mesmacque, G. (2000). "Fatigue life estimation after crack repair in 6005 A-T6 aluminum alloy using the cold expansion hole technique." *Fatigue Fract. Engr. Mater. Struct.*, 23, 991-916.
5. de Matos, P. F. P., McEvily, A. J., Moreira, P. M. G. P., and de Castro, P. M. S. T. (2007). "Analysis of the effect of cold-working of rivet holes on the fatigue life of an aluminum alloy." *International Journal of Fatigue*, 29(3), 575-586.
6. Edwards, L. & Ozdemir, A.T. (2004). "An assessment of the complete through thickness residual stress distribution after the split sleeve cold expansion of fastener holes." *Canadian Metallurgical Quarterly*. 43(2), 239-247.
7. Pavier, M. J., Poussard, C. G. C., and Smith, D. J. (1999). "Effect of residual stress around cold worked holes on fracture under superimposed mechanical load." *Engineering Fracture Mechanics*, 63(6), 751-773.
8. Herman, R. & Ozdemir, A.T. (1999). "Effect of expansion techniques and plate thickness on near-hole residual stresses and fatigue life of cold expanded holes." *Journal of Material Science*. 34, 1243-1252.
9. Landy, M. A., Armen, H. Jr., and Eidinoff, H. L. (1986). "Enhanced Stop-Drill Repair Procedure for Cracked Structures." *Fatigue in Mechanically Fastened Composite and Metallic Joints*, ASTM STP 927, edited by J. M. Potter, American Society for Testing and Materials, Philadelphia, PA, 190-220.
10. Poolsuk, Saravut. (1977). "Measurement of the elastic-plastic boundary around coldworked fastener holes," thesis, presented to Michigan State University at East Lansing, MI, in partial fulfillment of the requirements for the degree of Doctor of Applied Mechanics.
11. Statnikov, E.S. (2004). "Physics and mechanisms of ultrasonic impact treatment." IIV Document XIII-2004-04, International Institute of Welding, Paris, France.

12. Barsom, J.M & Rolfe, S.T. (2006). *Fracture and Fatigue Control in Structures: Application of Fracture Mechanics Third Edition*. ASTM, West Conshohocken, PA
13. Creager, M. (1966). "The elastic stress field near the tip of a blunt crack," Measter Science thesis, Lehigh University, Bethlehem, PA.
14. Kim Roddis, W.M. & Zhao, Y. (2003). "Finite-element analysis of steel bridge distortion-induced fatigue." *Journal of Bridge Engineering*, 8(5), 259-266.
15. Zhao, Y. & Kim Roddis, W.M. (2007). "Fatigue behavior and retrofit investigation of distortion-induced web gap cracking." *Journal of Bridge Engineering*, 12(6), 737-745.
16. Leon, A. (1998). "Benefits of split mandrel coldworking." *International Journal of Fatigue*, 20(1), 1-8.
17. Zhang, Y., Fitzpatrick, M. E., and Edwards, L. (2005). "Analysis of the Residual Stress around a Cold-expanded Fastener Hole in a Finite Plate." *Strain*, 41(2), 59-70.
18. Forgues, S. A., Bernard, M., and Bui-Quoc, T. (1993). "3-d axisymmetric numerical analysis and experimental study of the fastener hole coldworking process." *Computer Methods and Experimental Measurements for Surface Treatments Effects*, edited by C. A. Brebbia and M. H. Aliabadi, Engineering Sciences, (2), Computational Mechanics Publications, Southampton, UK, 61-70.
19. Ball, D. & Lowry, D.R. (1998). "Experimental investigation on the effects of cold expansion of fastener holes." *Fatigue Fract. Engr. Mater. Struct.*, 21(1), 17-34.
20. Poussard, C., Pavier, M. J., and Smith, D. J. (1995). "Analytical and finite element predictions of residual stresses in cold worked fastener holes." *Journal of Strain Analysis for Engineering Design*, 30(4), 291-304.
21. Poussard, C. G. C., Pavier, M. J., and Smith, D. J. (1994). "Prediction of residual stresses in cold worked fastener holes using the finite element method." *Proceedings of the 2nd Biennial European Joint Conference on Engineering Systems Design and Analysis*, 8(A) ASME, New York, N.Y., 47-53.
22. de Matos, P.F.P., Camanho, P.P. and de Castro, P.M.S.T. (2005). "Numerical simulation of cold working rivet holes." *Finite Elements in Analysis and Design*, 41, 989-1007.
23. Shao, X.J., Liu, Y., and Yue, Z.F. (2007). "FEM simulation and experimental test of residual stress of cold expansion hole of rectangular plate." *Key Engineering Materials*, 348-349, 745-748.
24. Stefanescu, D., Santisteban, J.R., Edwards, L. and Fitzpatrick, M.E. (2004). "Residual stress measurement and fatigue crack growth prediction after cold expansion of cracked fastener holes". *Journal of Aerospace Engineering*, 17(3), 91-97.

25. Ayatollahi, M.R. and Nik, M.A. (2009). "Edge distance effects on residual stress distribution around a cod expanded hole in Al 2024 alloy". *Computational Materials Science*, 45, 1134-1141.
26. Amrouche, A., Mesmacque, G., Garcia, S. and Talha, A. (2003). "Cold expansion effect on the initiation and the propagation of the fatigue crack". *International Journal of Fatigue*, 25, 949-954.
27. Ozelton, M. W., and Coyle, T. G. (1986). "Fatigue Life Improvement by Cold Working Fastener Holes in 7050 Aluminum." *Fatigue in Mechanically Fastened Composite and Metallic Joints, ASTM STP 927*, edited by J. M. Potter, American Society for Testing and Materials, Philadelphia, PA, 53-71.
28. Hanlon, T., Kwon, Y.N. and Suresh, S. (2003). "Grain size effects on the fatigue strength response of nanocrystalline metals". *Scripta Materialia*, 49, 675-680.
29. Vilhauer, B., Bennett, C., Matamoros, A., Rolfe, S. (2008). "Fatigue Behavior of Welded Connections Enhanced with UIT and Bolting." Final Report. *The Kansas Department of Transportation K-TRAN Project No. KU-07-1*.
30. An, X., Rodopoulos, C.A., Statnikov, E.S., Vitazev, E.S. and Korolkov, O.V. (2006). "Study of the surface nanocrystallization induced by the esonix ultrasonic impact treatment on the near-surface of 2024-T3561 aluminum alloy." *Journal of Materials Engineering and Performance*, 15(3), 355-364.
31. Dai, K. and Shaw, L. (2007). "Comparison between shot peening and surface nanocrystallization and hardening processes". *Materials Science and Engineering*, 463, 46-53.
32. Fisher, J.W. (1977). *Bridge Fatigue Guide: Design and Details*. American Institute of Steel Construction (AISC), New York, NY.
33. ASTM. (2007). "Standard Practice for Conducting Force Controlled Constant Amplitude Axial Fatigue Tests of Metallic Materials." *E466-07*, ASTM International, West Conshohocken, PA.
34. AASHTO. (2007). *LRFD Bridge Design Specifications*. 4th Edition, American Association of State Highway and Transportation Officials, Washington, D.C.
35. Vishay Micro-Measurements. (2005b). "Strain gage installation with M-Bond 200 adhesive." *Instruction Bulletin B-127-12*, Vishay Micro-Measurements, Raleigh, NC.
36. Vishay Micro-Measurements. (2007a). "Strain gage selection: criteria, procedures, recommendation." *Tech Note TN-505-4*, Vishay Micro-Measurements, Raleigh, NC.

37. Vishay Micro-Measurements. (2007d). "Strain gage soldering techniques." *Application Note TT-609*, Vishay Micro-Measurements, Raleigh, NC.
38. Vishay Micro-Measurements. (2007b). "Strain gages and accessories." *Micro-Measurements Product Catalog*, Vishay Micro-measurements, Raleigh, NC.
39. National Instruments. (2007) "NI 9219 operating instructions." *National Instruments Corp 374473B-01*. Austin, TX.
40. ASTM. (2001). "Standard Test Methods for Tension Testing of Metallic Materials." *E466-07*, American Society for Testing and Materials (ASTM) International, West Conshohocken, PA.